Experimental Investigation of a Passively Deforming Airfoil Under Dynamic Flow Conditions

Vom Fachbereich Maschinenbau

an der Technischen Universität Darmstadt

zur

Erlangung des Grades eines Doktor-Ingenieurs (Dr.-Ing.)

genehmigte

Dissertation

vorgelegt von

Ulrike Cordes, M.Sc.

aus Frankfurt am Main

Berichterstatter:	Prof. Dr.-Ing. C. Tropea
Mitberichterstatter:	Prof. Dr.-Ing. C.O. Paschereit
Tag der Einreichung:	28.06.2016
Tag der mündlichen Prüfung:	30.08.2016

Darmstadt 2016

D 17

Abstract

A rigid and a passively deforming airfoil, designed to alleviate fatigue causing load fluctuations that appear during normal operation of wind turbines, are investigated under unsteady conditions in two-dimensional wind tunnel experiments. In a first series of experiments, a vertical gust encounter is generated by means of an active grid. This approximates the wind turbine blade's passage through the atmospheric boundary layer and corresponds to the theoretical formulation of the Sears problem. In a second experiment the airfoil is oscillated in a steady free stream, which approximates the bending and twisting motion of a wind turbine blade and corresponds to the theoretical formulation of the Theodorsen problem.

The frequency dependent dynamic lift response of the rigid airfoil under attached flow conditions is compared to the Theodorsen and Sears function. If the airfoil is oscillated around its zero lift angle, experimental results and theoretical prediction agree. Contrary to theoretic assumptions, a substantial dependence on the mean angle of attack is observed: If the airfoil is oscillated around higher mean angles of attack, the dependence on the reduced frequency is is inverted.

The deforming airfoil shows good performance in terms of gust load alleviation over a wide range of operating conditions: At small mean angles of attack, up to 60 % of the fluctuating loads are alleviated. Under high mean angles of attack, leading edge vortices are efficiently suppressed, yielding up to 30 % less load fluctuations.

IV

Zusammenfassung

In dieser Arbeit wird die aerodynamische Lastantwort eines starren Flügels und eines Flügels mit selbstanpassender Wölbung experimentell unter instationären Bedingungen untersucht. Das Konzept der selbstanpassenden Wölbung wurde entwickelt, um Lastschwankungen an Windenergieanlagen zu dämpfen. Die Anströmbedingungen am rotierenden Windenergieanlagenblatt werden in zwei Windkanal Experimenten am zweidimensionalen Flügel abgebildet: Mittels eines aktiven Gitters wird eine sinusförmige Vertikalböe erzeugt, was das Durchstreichen des bodennahen Geschwindigkeitsprofils nachempfindet und gleichzeitig dem Sears-Problem entspricht. In einem zweiten Experiment oszilliert der Flügel in stationärer Anströmung, was Biege-Torsionsschwingungen am Windenergieanlagenblatt nachempfindet und dem Theodorsen-Problem entspricht.

Die frequenzabhängige dynamische Lastantwort des starren Flügels in angelegter Strömung wird mit der Sears- und der Theodorsen-Funktion verglichen. Eine Oszillation um den Nullauftriebswinkel zeigt gute Übereinstimmungen zwischen experimentellen Daten und theoretischen Werten. Entgegen theoretischer Annahmen hat der mittlere Anstellwinkel einen großen Einfluss auf das Übertragungsverhalten: Bei einer Oszillation um höhere mittlere Anstellwinkel werden deutliche Unterschiede in der Frequenzabhängigkeit der dynamischen Lastantwort beobachtet.

Das Flügelprofil mit selbstanpassender Wölbung dämpft fluktuierende Lasten effektiv über einen weiten Betriebsbereich: Bei kleinen mittleren Anstellwinkeln werden bis zu 60 % der Lastschwankungen gedämpft, unter höheren mittleren Anstellwinkeln wird die Bildung von Vorderkantenwirbeln unterdrückt, was zu einer Dämpfung von bis zu 30 % der Lastschwankungen führt.

VI

Danksagung

Contents

1. Introduction

1.1. Motivation

Wind turbines operate under highly unsteady conditions and are submitted to fluctuating inflow due to yaw misalignment, wind shear, tower shadow, gusts or atmospheric turbulence. This leads to fluctuating aerodynamic loads which are transmitted from the blades to the drive train and tower, where they cause fatigue and limit the life time and upscaling of turbines. Several concepts to alleviate these fluctuating loads are currently under investigation, amongst them a passive approach developed by Hufnagel and Lambie [38] at TU Darmstadt. The concept comprises an airfoil with a mechanically coupled leading-edge and trailing flap. The combined motion of leading-edge and trailing flap corresponds to a change of camber, therefor the concept is named 'adaptive camber concept'. Proof of concept was given by Lambie [57] under steady inflow conditions: The adaptive camber concept effectively manipulates the airfoil's load response. A lift curve with a high mean and reduced slope can be generated, which is promising in terms of gust load reduction on wind turbines. The experimental results have been numerically confirmed by Spiegelberg [88]. Spiegelberg investigated further the vibration dynamics of the adaptive camber airfoil and its response to unsteady inflow by coupling a structural model of the adaptive camber airfoil to unsteady thin airfoil theory and an unsteady panel code. Although attained under simplified conditions using linear theory, the results promised good gust load alleviation performance of the adaptive camber airfoil under unsteady conditions. The lift response of an airfoil in unsteady flow differs significantly from results obtained under quasi-steady conditions: At small angles of attack, every change in inflow leads to the shedding of a vortex in the wake of the airfoil. The wake vortices couple back on the flow field and pressure distribution on the airfoil, integrally altering the lift. At high angles of attack, viscous nonlinear effects become predominant and encourage delayed flow separation, accompanied by high transient

forces. These effects are still not completely understood. Accordingly, an analytic or numeric prediction of unsteady airfoil response has to be treated with caution, even on rigid airfoils. In the case of the adaptive camber airfoil, the increased fluid structure interaction intrinsic to the concept introduces an additional complexity into the predictions.

1.2. Objectives and Outline of the Thesis

To assess the adaptive camber airfoil in terms of gust load alleviation under unsteady conditions, a systematic experimental study has to be performed. This is the scope of this thesis, which is structured in six chapters:

Chapter 2 motivates the need for gust load alleviation in modern multi-mega-watt wind turbines and gives a brief overview of the current research. A special focus is placed on active trailing flap devices, as they are based on the same working principle as the passively working adaptive camber concept. Then the adaptive camber concept is introduced. The concept comprises a mechanically coupled leading-edge and trailing flap, where flow conditions on the leading-edge provoke a trailing flap deflection. The quasi steady aeroelastic response of the adaptive camber airfoil and parameters to influence this aeroelastic response are presented.

Chapter 3 provides the theoretical background of unsteady aerodynamics. First, important parameters to describe the unsteady inflow are defined and placed in the context of wind turbines. The physics of unsteady airfoil response differ substantially between attached and detached flow regime. In attached flow, at small mean angles of attack, the airfoil's load response is dominated by pressure forces and can be described by linear theory. The basic assumptions of linear theory as well as important results are summarized. At higher mean angles of attack, viscous forces that are not included in linear assumptions become predominant. A phenomenon typically referred to as dynamic stall occurs. Basic physical processes during dynamic stall and their implications for the adaptive camber airfoil are presented.

The pursued **experimental approach** of Chapter 4 and Chapter 5 is schematically visualized in Figure 1.1.
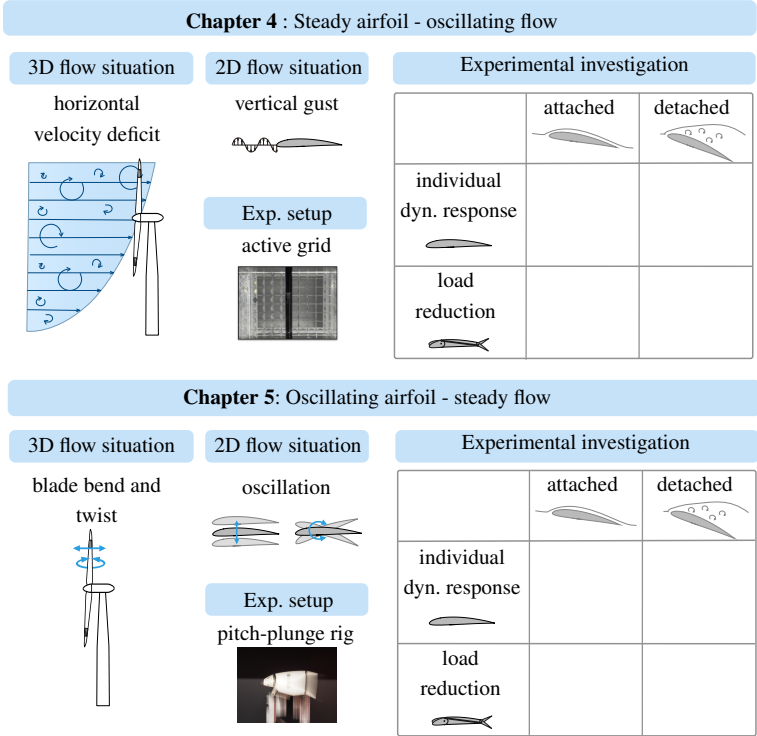
Figure 1.1.: Schematic visualization of the pursued experimental approach.

From the three-dimensional flow situation in the rotating reference frame of a wind turbine, the corresponding flow scenarios on a two-dimensional blade section are transferred into wind tunnel experiments. A two-dimensional airfoil model equipped with an adaptive camber mechanism and a rigid reference airfoil are submitted to these unsteady conditions. The experimental data are evaluated in terms of individual dynamic airfoil response and compared to prediction models from literature. The adaptive camber airfoil's gust load alleviation performance is assessed by comparing the dynamic load response of the adaptive camber and the rigid reference airfoil under the same unsteady conditions.

Chapter 4 presents the experimental investigation of the vertical gust encounter. The vertical gust encounter is an important flow condition in terms of gust load alleviation: In the rotating reference frame of a wind turbine, the vertical gust corresponds to the passage of the blade through a horizontal velocity deficit, caused by -for example-the earth atmospheric boundary-layer or the tower shadow. Experiments were performed at the university of Oldenburg active grid wind tunnel. The active grid offers the possibility to vary the reduced frequency, while keeping all other flow parameters constant. An extensive investigation of the influence of the mean angle of attack, the gust amplitude and the reduced system stiffness on the frequency dependent individual dynamic load response and the frequency dependent gust load alleviation performance of the adaptive camber airfoil was carried out. The individual dynamic load response of the rigid airfoil is used to validate the linear transfer function of an airfoil encountering a sinusoidal vertical gust, the so-called Sears function. This widely used transfer function still lacks a systematic experimental verification in terms of reduced frequency dependence.

Chapter 5 presents the experimental investigation of a pitching and plunging airfoil, obtained at the Eiffel wind tunnel at TU Darmstadt. This experimental setup approximates the twisting and bending oscillations of a wind turbine blade, which occur for example due to cyclic loading or after a heavy gust impact. In attached flow, the experimental results serve as a second basis to validate linear transfer functions of the airfoil's dynamic load response. Pitching and plunging motions induce additional inertial forces on the adaptive camber airfoil, which is designed to be actuated by aerodynamic forces alone. The influence of inertial forces on the gust load alleviation capabilities is studied. At high mean angles of attack, a phenomenon typically referred to as 'dynamic stall' occurs. Dynamic stall is accompanied by coherent leading-edge vortices that induce high localized forces on the airfoil. The interaction between coherent leading-edge vortices and the adaptive camber airfoil's rotatable leading-edge is studied by means of particle image velocimetry.

Chapter 6 summarizes the results regarding individual airfoil response and gust load alleviation capabilities. An outlook for further research is given.

2. State-of-the-Art

2.1. Gust Load Alleviation

The Need for Gust Load Alleviation

The power P produced by a wind turbine of diameter D and subjected to an inflow velocity U_∞ can be estimated according to Hau [34] by

$$P = C_P \frac{\rho}{2} U_\infty^3 \pi \left(\frac{D}{2} \right)^2 \tag{2.1}$$

where ρ is the mass density of the air and C_P is the turbines total power coefficient, determined by the turbine design. In 1926, using linear momentum theory, Betz [10] found that not more than 16/27 of the energy present in an air stream can be extracted by an ideal turbine. Independent of the turbine design the power coefficient is therefore limited to $C_{P,max} \leq 0.59$. According to Hau [34], modern turbines achieve a power coefficient of $C_{P,max} > 0.5$. Increasing power production is thus most easily achieved by increasing the turbine diameter D. Power production scales with the square of the rotor diameter D^2, but the cost of energy (COE) does not. COE is estimated by

$$\text{COE} = \frac{\text{lifetime energy capture}}{\text{capital} + \text{operation} + \text{maintenance cost}} \tag{2.2}$$

Van Dam et al. [95] confirm that the most effective way to decrease COE on wind turbines is by increasing the rotor diameter. These facts and the demand for affordable green energy production have led to an increase of turbine rotor diameter in recent years, as illustrated in Figure 2.1. With increasing rotor diameter, the turbine experiences higher load fluctuations and increased bending moments due to the passage through the wind profile of the atmospheric boundary-layer (ABL). Increased bending oscillations are critical, as a contact of the blades with the tower or other
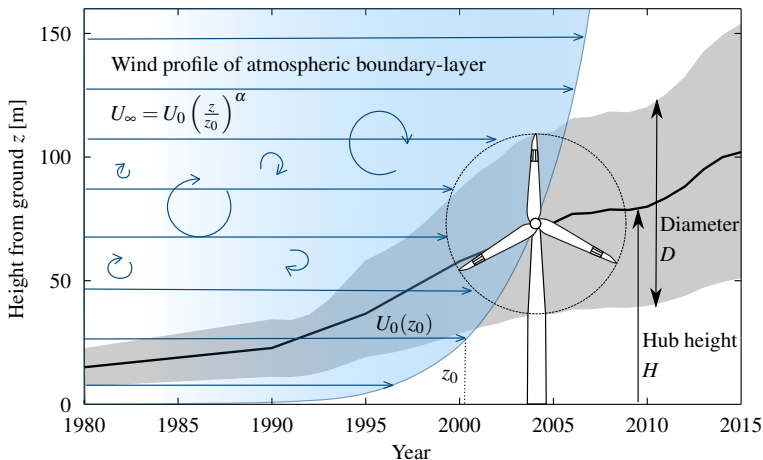
Figure 2.1.: Average size of world wide installed wind turbines. Data taken from IWES [106]. The growing demand for affordable green energy leads to an increase of rotor diameter. With increasing rotor diameter, the wind turbine blade experiences higher velocity fluctuations due to the passage of the wind profile of the atmospheric boundary-layer. The wind profile of the atmospheric boundary-layer is commonly approximated by a power law, where $U_0(z_0)$ is the known wind speed at a certain height z_0 and α is an empirically derived coefficient that depends on the stability of the atmosphere.

components has to be avoided. Deflection analysis and tower clearance verification are the first steps in wind turbine blade design according to the Det Norske Veritas (DNV) standard [99]. Bending oscillations can be reduced by either stiffer blades or alleviation of the fluctuating aerodynamic loads. A stiffer blade design can be accomplished by the use of more glass fiber or stiffer materials such as carbon fibers. The disadvantages are increased weight or an economical disadvantage. Alleviation of fluctuating loads can be achieved by innovative rotor design, which is not only beneficial in terms of blade bending and tower clearance. It also helps reduce fluctuating loads and increase lifetime of all turbine components, as cyclic aerodynamic loads are transmitted from the blades to the drive train and tower. The importance of cyclic loading on material failures was first reported by Wöhler [107] in 1870, who found that components fail well below their ultimate load if subjected to cyclic

loading of smaller amplitudes. This degradation is known as fatigue and the number of load cycles that a component can withstand before it breaks is the fatigue life. Fatigue life is determined by properties of the cyclic loading itself (amplitude, mean, oscillation frequency, waveform and time history) and the properties of the structure (geometry and material). Wind turbines are complex mechanical systems that operate in a wide spectrum of fluctuating loads. Sutherland [93] summarizes methods of fatigue analysis specially adapted for wind turbine applications. Veers et al. [98] state that an alleviation of 10-20 % of aerodynamic load fluctuations would result in substantial savings of all major turbine components and improve the cost of energy significantly. This has given rise to extensive research in smart rotor technology, aiming to alleviate fluctuating loads, reduce fatigue, increase turbine lifetime and rotor diameter and thereby reduce the cost of energy.

Classification of Gust Load Alleviation Devices

A comprehensive overview on smart rotor systems is given by Barlas and van Kuik [8] and van Dam et al. [95]. The authors categorize the approaches of smart rotor control into active and passive systems, which is schematically visualized in Figure 2.2:

- **Active systems** manipulate loads by actively controlling wind turbine components or the surrounding flow

through -for example- a change in pitch, generator torque, flaps, tabs or other devices. The need for appropriate sensor input, effective control strategies and advanced actuators all represent current research topics associated with active load control on wind turbines.

- **Passive systems** manipulate the boundary-layer passively or allow a deformation under aerodynamic loading due to their structural design.

Compared to active systems, passive systems are more robust and less complex, as no sensors, actuators or control schemes are needed. If they encompass deformations, a thorough structural design is required. Furthermore, smart rotor control systems can be categorized into:

- approaches that manipulate the **entire wind turbine** blade and

- **sectional approaches** that influence only part of the wind turbine blade.
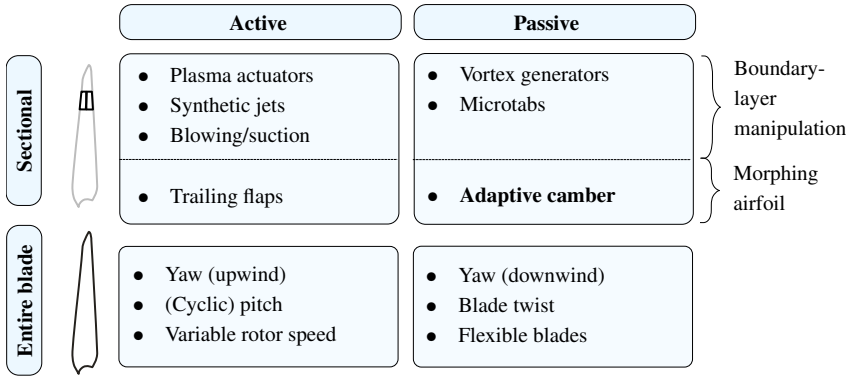
Figure 2.2.: Schematic visualization of the categorization of smart rotor control systems (incomprehensive), adapted from Barlas and van Kuik [8] and van Dam et al. [95]. The adaptive camber airfoil analyzed in this study can be classified as one of the few passive sectional approaches.

The fluctuating velocity perturbations on which smart rotor systems have to react can be attributed to different causes. Figure 2.3 gives a spectral view of these fluctuating perturbations. Leishman [63] categorizes the fluctuating inflow on a wind turbine into deterministic perturbations, which occur periodically and arise from wind shear, yaw misalignment or tower shadow, and stochastic perturbations due to turbulence, wake dynamics, blade/wake interaction or gusts. Deterministic fluctuations occur with rotational frequency (1P) of the rotor or multiples of it. Stochastic fluctuations are distributed over a broad range of frequencies. According to Burton [14], the response time of systems acting on the entire blade, as -for example- state-of-the-art pitching mechanisms, is generally in the order of minutes; faster changes are not feasible. Bergami and Gaunaa [9] show in a numerical analysis on the NREL 5 MW that only 11 % of a turbine's life time fatigue is caused by deterministic loads around the 1P frequency ($\approx$ 0.2 - 1 Hz on modern multi megawatt turbines). 89 % of the damage equivalent load of a turbine are attributed to stochastic processes. These loadings can neither be alleviated by systems acting on the whole blade nor
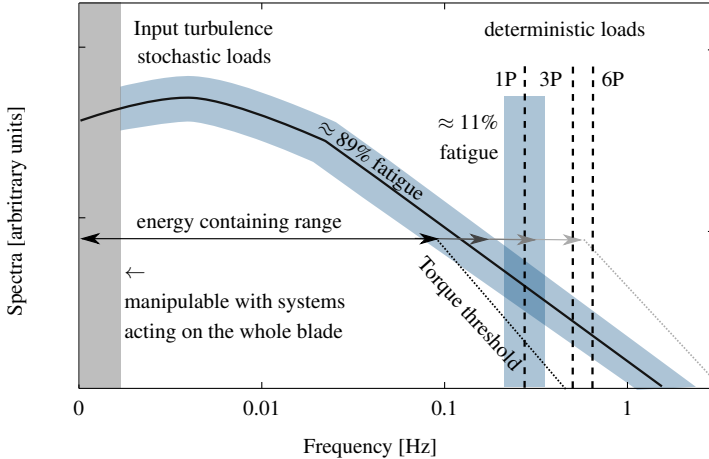
Figure 2.3.: Schematic representation of the frequency content of the velocity fluctuations encountered by a wind turbine. The stochastic turbulent inflow contains a wide band of frequencies while deterministic loads occur at multiples of the rotational frequency P. The entire frequency range contributes to fatigue, while energy is only harvested in the energy containing range, limited by the torque threshold, as pointed out by Connell [19]. The limits of the energy containing range are difficult to estimate as very few temporally highly resolved data sets of the inflow velocity on a wind turbine exist.

by systems aiming to reduce deterministic loading such as cyclic pitch.

Trailing Flaps

According to Marrant and van Holten [67], trailing flaps are the most promising devices for the alleviation of high frequency load fluctuation on wind turbines. A trailing flap deflection of only a few degrees causes a substantial change of blade lift. Trailing flaps can be distributed radially on the wind turbine blade. They are accordingly less costly in terms of actuation power, exhibit faster response and can react locally. Using trailing flaps to alter lift characteristics is common practice on aircraft. Barbarino et al. [7] give an extensive review of past and current aircraft related research topics. In aircraft applications, flap deflections are set by the pilot if inflow conditions or mission segments deviate from ideal cruise conditions. In wind turbine applications, this task has to be automated and executed by a controller. It

9

was experimentally shown by Bak et al. [6] that an almost complete attenuation of the load fluctuations on a two-dimensional airfoil section is possible, if the angle of attack perturbations are known beforehand and the controller can set the flap deflection accordingly. Andersen et al. [3] point out that the time lag between the angle of attack perturbation and the controller reaction is the most critical point in wind turbine applications. In a numerical study of the *Upwind* 5 MW reference turbine, they observed a decrease in fatigue load alleviation efficiency in the order of 20-30 % for time lag of 150 ms and pointed out that larger time lags can have harmful effects on the wind turbine. The adequate sensing of oncoming perturbations and the realization of small response time of the flap actuation are critical issues in gust load alleviation by active trailing flaps. Their realizability is best investigated in experimental studies.

Literature Review of Experimental Investigations

In experimental studies, trailing flaps showed to effectively alleviate deterministic and stochastic loadings: Lee et al. [61] experimentally investigated a two-dimensional airfoil with an active trailing flap at high Reynolds numbers ($Re = 540.000 - 660.000$). The two-dimensional airfoil had a span of 2 m, a chord of 1.2 m and was equipped with a hinged trailing flap with maximum flap deflection of $\pm 10\,°$. The flap was actuated with up to 1200 N according to a feedback control protocol, which got its input from load cells measuring the flapwise bending loads. When exposed to turbulent inflow, load fluctuations were reduced by 20-30 %. Better results in terms of gust load alleviation were found by Van Wingerden et al. [96,97] in a lower Reynolds number experimental setup: A two-dimensional airfoil of 0.12 m chord and 0.9 m span and a two bladed test turbine of $D \approx 2$ m diameter with the dynamically scaled properties of the *Upwind* 5 MW reference turbine were exposed to stochastic perturbations as well as periodic disturbances due to yaw misalignment. Mechanical stresses, measured at the blade root, were fed into a real time environment that controls high performance actuators. In this set up, up to 90 % of the periodic perturbations and up to 55 % of distinct frequencies in the broad turbulence spectrum were alleviated.

From an aerodynamic point of view, trailing flaps are the right choice to alleviate high frequency load fluctuations. Adequate control of trailing flaps is the critical point: An ideal gust load alleviation device reacts on a changes in flow conditions before they are converted into aerodynamic loads and mechanical stresses. Active systems currently under investigation use mechanical stresses that act as an input signal. Gaunaa and Andersen [27] proposed to use the pressure difference on the leading flap as a sensor input, as aerodynamic conditions at the leading-edge are a good estimator for the total lift and hence the mechanical stresses. The adaptive camber airfoil exploits the same idea: the pressure distribution on the leading-edge is used as a sensor for the oncoming flow. Simultaneously, the leading-edge serves as an actuator, making the whole system passive. No further control schemes or actuation power are foreseen.

2.2. Adaptive Camber Concept

Theoretical Considerations

From thin airfoil theory (see for example Katz [46]) it follows that the stationary lift coefficient C_L of a rigid thin airfoil is:

$$C_L = 2\pi\alpha - C_{L0}(\eta) \tag{2.3}$$

where $2\pi\alpha$ is the lift coefficient for a flat plate under angle of attack α and $C_{L0}(\eta)$ is an additive constant accounting for camber η. The lift curve slope $\partial C_L/\partial\alpha$ is then 2π, since on a rigid airfoil the effect of camber is independent of α. If the camber of an airfoil changes with α, the lift curve slope deviates from 2π:

$$\frac{\partial C_L}{\partial\alpha} = 2\pi - \frac{\partial}{\partial\alpha}C_{L0}(\eta(\alpha)) \tag{2.4}$$

This can be beneficial in terms of gust load alleviation, as a gust expresses itself mainly through a change of angle of attack $\Delta\alpha$ in the rotating reference system of a wind turbine. The fluctuating load on a two-dimensional wind turbine blade section can be approximated by

$$\Delta C_L = \frac{\partial C_L}{\partial\alpha}\Delta\alpha \tag{2.5}$$
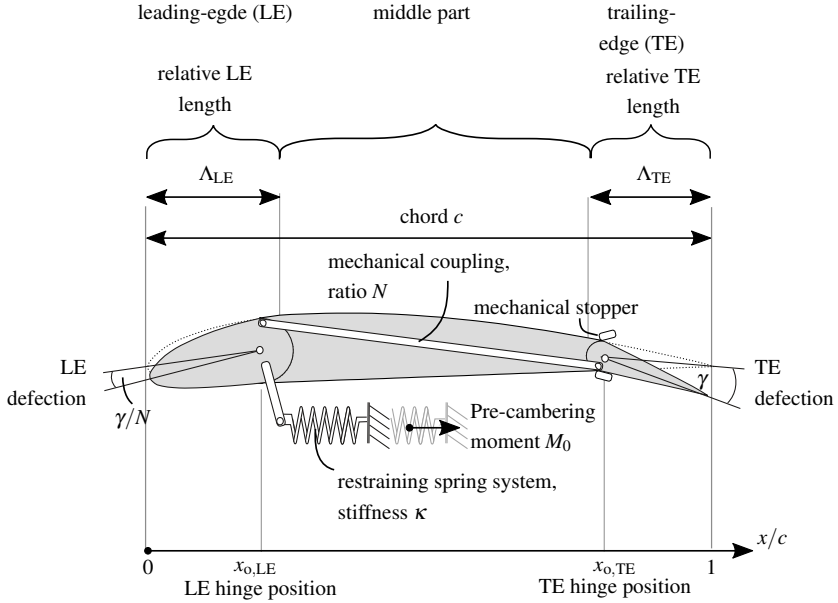
Figure 2.4.: Schematic view of the adaptive camber airfoil: Leading-edge and trailing flap are detached and hinged. The rotation of the leading-edge γ/N is transferred to the trailing flap via a mechanical coupling mechanism of coupling ratio N. The motion is opposed by a restraining spring system of stiffness κ, allowing to apply a pre-cambering moment M_0.

Modifying the airfoil camber such that the lift curve slope $\frac{\partial C_L}{\partial \alpha} < 2\pi$ results in a reduction of fluctuating loads ΔC_L, compared to a rigid airfoil with constant camber. One way to achieve such modification of camber in a purely passive way is the adaptive camber concept.

Working Principle

The concept was developed by Hufnagel and Lambie at TU Darmstadt and patented in 2011 [38]. A schematic view of an airfoil equipped with adaptive camber concept is given in Figure 2.4: It consists of an airfoil with detached and hinged leading-edge (LE) and a trailing-edge (TE) flap. Leading-edge and trailing flaps are mechanically coupled via a coupling mechanism of ratio N. A clockwise rotation of the leading-edge of γ/N results in a counterclockwise rotation of the trailing flap of γ
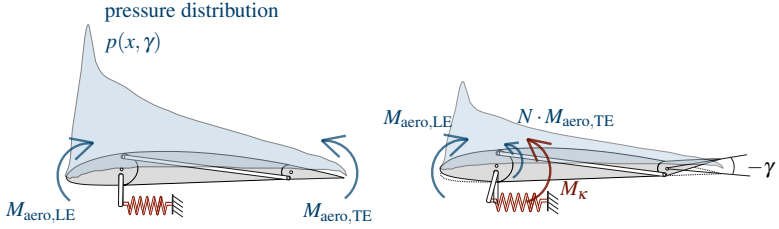
Figure 2.5.: Functionality of the adaptive camber airfoil: High aerodynamic loads at high angles of attack induce a high aerodynamic moment on the leading-edge. Both leading and trailing flap rotate upwards, until an equilibrium between restraining spring system and aerodynamic forces is obtained.

and vice versa. The combined motion of both flaps results in a change of camber. The maximal flap deflections are limited by mechanical stoppers. A spring system of stiffness κ restrains the motion by applying the spring moment M_κ that counteracts the leading-edge deflection. The mechanism can be pre-stressed by applying an additional pre-cambering moment M_0. M_0 is defined as the moment that needs to be applied to bring the airfoil to its reference shape ($\gamma = 0°$). A positive M_0 increases the camber (flaps down), if no flow is present. The mode of operation of the adaptive camber airfoil is schematically shown in Figure 2.5: When placed in an air stream, a pressure distribution $p(x, \eta)$ is generated around the airfoil, integrally responsible for the aerodynamic loads. The pressure distribution is such that the main part of the load is generated at the leading-edge, whereas the level of the load is mainly determined by the trailing flap deflection. The adaptive camber airfoil concept exploits these facts and uses the airfoil's leading-edge to actuate the trailing flap: At high angles of attack, the pressure distribution generates an upward bending aerodynamic moment $M_{\mathrm{aero,LE}}$ around the leading-edge. Around the trailing flap, an aerodynamic moment $M_{\mathrm{aero,TE}}$ is generated, which is an order of magnitude smaller than $M_{\mathrm{aero,LE}}$. The leading-edge is rotated upwards around its hinge by $-\gamma/N$. The motion is transfered via the mechanical coupling system to the trailing flap. The trailing flap rotates upward by $-\gamma$ and the level of the pressure distribution around the airfoil decreases. The combined flap motion corresponds to a de-cambering of the airfoil. The de-cambering persists, until an equilibrium

$$M_{\mathrm{aero,LE}}(\alpha, q, \eta, \Lambda_{\mathrm{LE}}, x_{\mathrm{o,LE}}) - N \cdot M_{\mathrm{aero,TE}}(\alpha, q, \eta, \Lambda_{\mathrm{TE}}, x_{\mathrm{o,TE}}) = M_\kappa(\kappa, M_0, \eta) \quad (2.6)$$

between the aerodynamic moments M_aero and the restraining spring moment M_κ is reached. For one fixed configuration of the adaptive camber airfoil (i.e. leading and trailing flap length, hinge positions and coupling ratio), the dependencies of equation 2.6 reduce to

$$M_\text{aero,LE}(\alpha, q, \eta) - n \cdot M_\text{aero,TE}(\alpha, q, \eta) = M_\kappa(\kappa, M_0, \eta) \tag{2.7}$$

The driving aerodynamic forces M_aero are proportional to the aerodynamic pressure $q = \frac{\rho}{2} U_\infty^2$ and the angle of attack α. The restraining spring moment is composed of the pre-cambering moment M_0 and a moment proportional to the LE deflection γ/N and the physical spring stiffness κ. Omitting the influence of $M_\text{aero,TE}$ yields:

$$\frac{\rho}{2} U_\infty^2 \alpha \cdot M_\text{aero,LE}(\eta) \approx M_0 - \kappa \cdot \frac{\gamma}{N} \tag{2.8}$$

The proportionality between the $M_\text{aero,LE}$ and the angle of attack α leads to an uniform de-cambering of the airfoil with increasing α. Figure 2.6 shows the numerically calculated aeroelastic response of the adaptive camber airfoil and graphically illustrates how a constant de-cambering results in a decreased lift curve slope $\partial C_L / \partial \alpha$ compared to a rigid airfoil. The starting point of de-cambering is defined by the pre-cambering moment M_0, the rate of de-cambering is determined by the system stiffness κ. The effect on the lift curve under quasi steady flow conditions was experimentally investigated by Lambie [57]. He states:

- The lift curve slope $\partial C_L / \partial \alpha$ decreases with decreasing system stiffness κ.

- Adding a pre-cambering moment M_0 shifts the lift curve vertically.

In this way, the lift curve of the adaptive camber airfoil can be customized according to a target function. For gust load alleviation on wind turbine blades, the lift curve target function has a small slope whilst maintaining a high mean. The driving aerodynamic moments M_aero scale with the dynamic pressure $q = \frac{\rho}{2} U_\infty^2$. At higher inflow velocity, the adaptive camber airfoil de-cambers earlier and at a higher rate. This perceived reduction of the pre-cambering moment M_0 and the physical system stiffness κ is accounted for by defining the reduced pre-cambering moment M_0^+ and the reduced system stiffness κ^+:

$$M_0^+ = \frac{M_0^+}{c^2 \frac{\rho}{2} U_\infty^2}, \qquad \kappa^+ = \frac{\kappa}{c^2 \frac{\rho}{2} U_\infty^2} \tag{2.9}$$
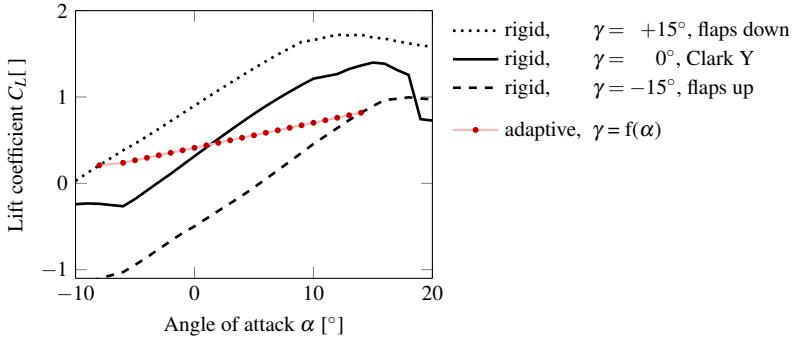
Figure 2.6.: Lift coefficient C_L plotted over the angle of attack α, obtained with a steady panel code (*XFLR5*). The rigid airfoil with constant camber has a lift curve slope of $\partial C_L/\partial \alpha \approx 2\pi$. Fixing leading and trailing flap at the indicated deflection angles leads to an increase of camber and shifts the lift curve vertically, but does not affect $\partial C_L/\partial \alpha$. The lift coefficient of the adaptive camber airfoil is obtained by gradually decreasing the flap deflection from $\gamma_{(\alpha=-8°)} = 15°$ to $\gamma_{(\alpha=+12°)} = -15°$. This results in a decreased lift curve slope $\partial C_L/\partial \alpha$.

For a constant M_0^+ and a constant κ^+, the airfoil de-cambers in the same manner.

The influence of the adaptive camber airfoil configuration, i.e. the relative leading and trailing flap length Λ_{LE} and Λ_{TE}, the leading and trailing flap hinge positions $x_{\mathrm{o,LE}}$ and $x_{\mathrm{o,TE}}$, the coupling ratio N, as well as the airfoil camber η on the aeroelastic response of the adaptive camber airfoil was studied analytically by Spiegelberg [88]. He found that:

- For a given airfoil configuration (i.e. leading-edge and trailing flap length, hinge positions and coupling ratio), a lift curve slope $\partial C_L/\partial \alpha = 0$ can be attained by choosing an appropriate reduced system stiffness (see Spiegelberg [88], p. 69, Figure 5.6).

Lambie [57] found a coupling ratio of $N = 3$ (meaning that a $1°$ clockwise rotation of the leading-edge results in a $3°$ rotation in counterclockwise direction of the trailing flap), a leading-edge length of 20% chord and a trailing length of 30% chord to be an experimentally viable and effective configuration. In this study, all experimentally investigated airfoil models are equipped with an adaptive camber mechanism of this

configuration, the corresponding parameters are summarized in Table 2.1.

Table 2.1.: Common parameters of the investigated adaptive camber airfoil models.

Parameter		Unit	Quantity
Leading-edge length	Λ_{LE}	$[x/c]$	0.2
Trailing flap length	Λ_{TE}	$[x/c]$	0.3
Leading-edge hinge position	$x_{\mathrm{o,LE}}$	$[x/c]$	0.2
Trailing flap hinge position	$x_{\mathrm{o,TE}}$	$[x/c]$	0.7
Coupling ratio	N	$[°/°]$	3
Airfoil profile	Clark Y		

3. Theoretical Background: Unsteady Aerodynamics

Unsteady flow conditions can be described by their frequency, amplitude and waveform. All investigations performed during this thesis deal with sinusoidal waveforms and differ only in terms of frequency and amplitude. Section 3.1 presents the corresponding **parameters of unsteady aerodynamics** and places them in the context of wind turbine applications. If an airfoil is subjected to unsteady conditions, its dynamic response differs from quasi-steady approximations. In the linear region of **attached flow regime**, the unsteady airfoil response follows a sinusoidal perturbation with the same waveform and frequency, but with a different amplitude and a phase shift. This behavior is most conveniently described with transfer functions. In section 3.2 the common approaches to derive theoretical transfer functions are reviewed. In **detached flow regime** the airfoil response follows the perturbation with a different waveform, including high transient forces. The physical mechanisms of lift generation that are responsible for this change in behavior are reviewed in section 3.3.

3.1. Parameters of Unsteady Aerodynamics

Harmonic unsteady flow conditions are described by the frequency of their occurrence and their amplitude. For comparability, these parameters are expressed in dimensionless form: the **reduced frequency** k describes the unsteadiness in time and the **Strouhal number** Sr the perturbation amplitude.

Reduced Frequency k

The reduced frequency k is used to quantify the unsteadiness of a flow situation. It is defined as

$$k = \frac{\pi f c}{U_\infty} \tag{3.1}$$

Physically, k signifies the ratio of convective time or length-scale to the period or length-scale of the perturbation.

$$k = \pi \frac{T_{\text{flight}}}{T_{\text{perturbation}}} = \pi \frac{L_{\text{flight}}}{L_{\text{perturbation}}} \tag{3.2}$$

Figure 3.1 illustrates the relationship for an airfoil encountering a traveling sinusoidal vertical gust.
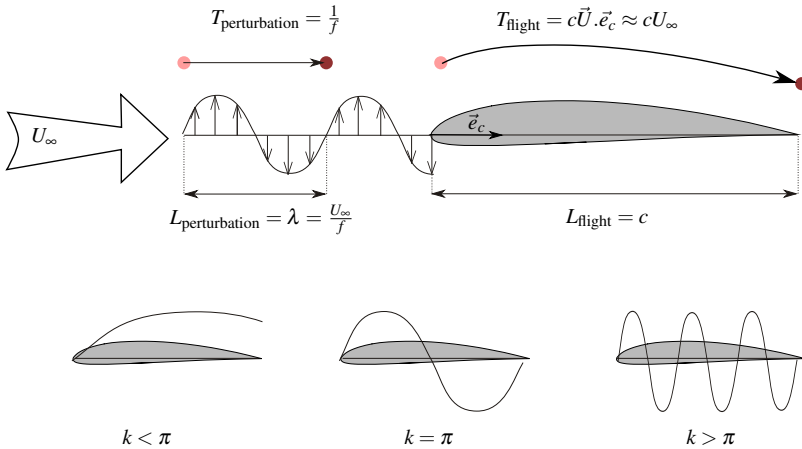
Figure 3.1.: Physical significance of the reduced frequency k for an airfoil: For small k, the wave-length of the perturbation is long compared to the chord length. The airfoil 'sees' only a small part of the perturbation. For high k, the wavelength of the perturbation is short compared to the chord length.

An approximation of the reduced frequencies encountered by a wind turbine blade due to the passage of the atmospheric boundary-layer is given in Figure 3.2. In the rotating reference frame, the time of flight T_{flight} depends mainly on the radial position of the airfoil section r, the chord length at that radial position $c(r)$ and the
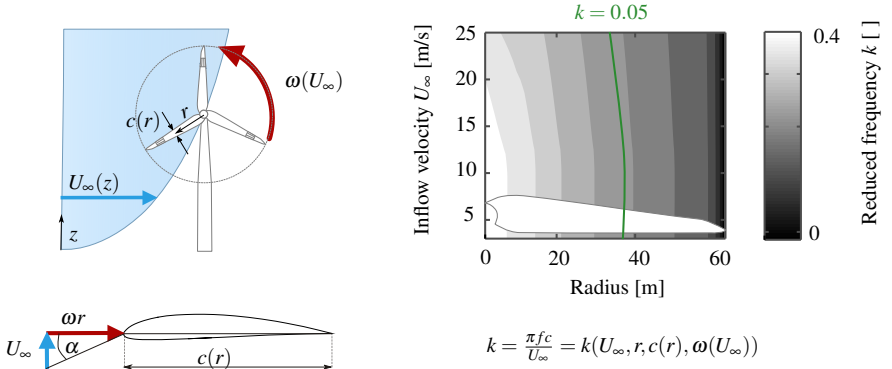
Figure 3.2.: Left: The passage of the atmospheric boundary-layer leads to angle of attack fluctuations on the blade section. Right: Reduced frequency of the 1P perturbation, seen by an airfoil section on a certain radial position at a certain inflow velocity U_∞, approximated with data of the NREL 5 MW turbine provided by Jonkman et al. [45].

rotational velocity ω. The rotational velocity ω is defined by the turbine characteristics and increases with increasing wind velocity until the rated wind speed is reached. The period of the perturbation $T_{\text{perturbation}}$ depends primarily on the nature of the perturbation. Deterministic perturbations occur with multiples of the rotor frequency P. Perturbations due to yaw misalignment or perturbations due to the passage of the atmospheric boundary-layer occur with 1P frequency. Stochastic perturbations due to atmospheric turbulence or gusts are distributed over a wide spectra of frequencies. There is disagreement about the exact k-limit that distinguishes unsteady aerodynamics from steady aerodynamics. Leishman [64] (p. 427) considers disturbed flow of $k \geq 0.05$ as unsteady, Pereira et al. [74] (p. 208) sets the limit to $k = 0.02$ and Carr et al. [16] found significant dynamic effects for reduced frequencies as small as $k = 0.004$.

Figure 3.2 illustrates that wind turbine blades encounter a large variety of reduced frequencies and the flow on a wind turbine blade section must be considered as unsteady.

Strouhal Number *Sr*

The perturbation amplitude is quantified by the Strouhal Number *Sr*. In the context of flapping flight, the Strouhal number of a plunging airfoil is usually defined as the ratio of oscillating speed to forward speed:

$$Sr = \frac{2\Delta h f}{U_\infty} \tag{3.3}$$

Considering an equal effective angle of attack, the Strouhal number of a pitching airfoil can be derived as:

$$Sr = \frac{2\tan\widehat{\alpha}_\text{p}}{\pi} \tag{3.4}$$

where $\widehat{\alpha}_\text{p}$ is amplitude of the pitching oscillation. For an airfoil encountering a sinusoidal vertical gust of amplitude $\widehat{v}_\text{g}$, the effective angle of attack approach yields:

$$Sr = \frac{2\widehat{v}_\text{g}}{U_\infty} \tag{3.5}$$

Figure 3.3 visualizes the relationships for the flow situations relevant in this study.

plunge   pitch   vertical gust
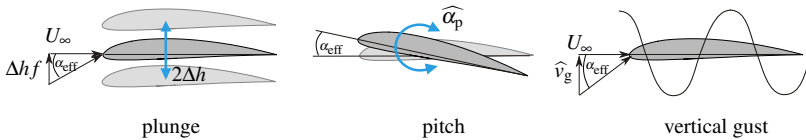
Figure 3.3.: Definition of the Strouhal number on a plunging airfoil (left) and equivalent formulations on a pitching airfoil (middle) and an airfoil entering a sinusoidal vertical gust (right).

The perturbation height experienced by wind turbines is difficult to estimate as it depends highly on the inflow velocity field. According to Sutherland [93], current practice is to describe the inflow velocity field by a vertical velocity, superimposed by wind shear and a turbulence intensity. This is also the recommendation of IEC Standards Comity [39]. Rezaeiha et al. [79] followed the IEC standard and calculated the angle of attack α caused by turbulence, wind shear, yawed inflow and tower shadow on the *DTU-10MW-RWT* reference wind turbine. They compared the results

- Yaw missalignment: $10°$
- Wind shear: power law
- Tower shadow
- Turbulence intensity: 0.16
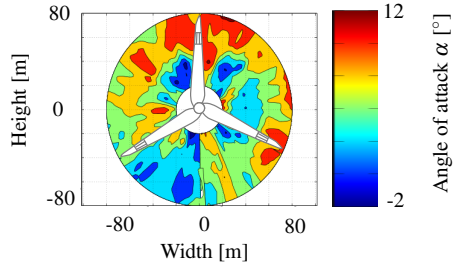
Figure 3.4.: Angle of attack on the rotor plane of the *DTU-10MW-RWT* reference wind turbine under representative operating conditions, taken from Rezaeiha et al. [79].

to the angle of attack on the same wind turbine under constant inflow. According to their calculations, the tower shadow has a negligible effect on the angle of attack fluctuation α' encountered during one rotation. Wind shear, modeled by a power law and and a $10°$ yaw misalignment increase α' by $2 - 4$ times, compared to the clean inflow. The highest impact is observed when changing the turbulence intensity T_u: α' increases $10 - 14$ times for $T_u = 0.16$. A reproduction of Rezaeiha's results is given in Figure 3.4 on the right. The angle of attack fluctuations on a blade section during one revolution of up to $\alpha' \approx 12°$ occur. According to Rezaeiha, the inflow scenario is representative for the operating conditions of multi-megawatt turbines. In nature, fully developed turbulence is characterized by intermittent fluctuations of the wind velocity comprising nonlinear and non-Gaussian properties, which are not accounted for by the IEC norm. Boettcher et al. [11] analyzed an excerpt of atmospheric wind measurements collected with a frequency of $4\,Hz$ over one year. They found wind to be highly intermittent, meaning that strong gusts occur more often than predicted by Gaussian distribution, which would result in even higher α' on a wind turbine blade section.

It can thus be assumed that angle of attack fluctuations of several degrees are commonly encountered by wind turbine blades. Depending on the blade section's mean angle of attack, the flow remains attached to the airfoil surface or separates. The underlying physics during both flow situations differ fundamentally.

3.2. Attached Flow Regime

If the total angle of attack of the unsteady flow remains below the static stall angle, the flow stays attached to the airfoil surface. In the attached flow regime, pressure forces dominate over viscous forces. A constant linear dependence between airfoil lift and angle of attack exists under quasi-steady conditions. Under dynamic conditions the lift follows the perturbed angle of attack with a certain amplitude and phase shift that depend on the reduced frequency of the perturbation, independent of the perturbation amplitude. Unsteady thin airfoil theory is the classical low order approach to estimate the unsteady airfoil response under attached flow conditions. Section 3.2.1 summarizes the assumptions leading to **unsteady thin airfoil theory**. Traditionally, unsteady thin airfoil theory is used to obtain the unsteady lift response of an airfoil in frequency domain, using so-called transfer functions. Transfer functions can be obtained by approaches of different complexities: Assuming a spatially constant undisturbed velocity field and linearizing the kinematic boundary condition yields classical first-order transfer functions. Closed form solutions for rigid airfoils, derived in the 1920s and 1930s are briefly summarized. Section 3.2.2 presents explicit **first-order solutions for the rigid airfoil** for flow scenarios relevant in this thesis, namely the pitching and plunging rigid airfoil and a fixed rigid airfoil submitted to a sinusoidal vertical gust. **First-order solutions for the adaptive camber airfoil** are given by Spiegelberg and reviewed in section 3.2.3. Second-order solutions are obtained by accounting for a spatially variable velocity field and a coupling between steady and unsteady flow solutions. Section 3.2.4 illustrates the major difference between first and second-order models and reviews a closed form **second-order solution for the rigid airfoil** for a sinusoidal vertical and horizontal gust that will be relevant later in this study. Although transfer functions based on thin airfoil theory are extensively used in flutter calculations, a very limited amount of experimental validation data exists. Section 3.2.5 gives a **literature review of experimental investigations** relevant to this thesis.

3.2.1. Unsteady Thin Airfoil Theory

Thin airfoil theory uses potential flow to represent an airfoil by its camber line only. For an airfoil of small camber, singularities are distributed on the x-axis in such a way that the induced velocity fulfills the kinematic boundary condition at the camber line. This assumption comprises the interchangeability of a vertically moving camber line with an additional vertical velocity component v of opposite direction. An illustrative example is depicted in Figure 3.5. Different boundary condition scenarios can thus be distinguished by the spatial and temporal occurrence of relative velocities between airfoil and surrounding flow. Steady thin airfoil theory differs fundamentally from dynamic thin airfoil theory. A schematic visualization of the considerations leading to this statement is shown in Figure 3.6. Besides fulfilling the kinematic boundary condition, each singularity induces a tangential velocity. This tangential velocity is
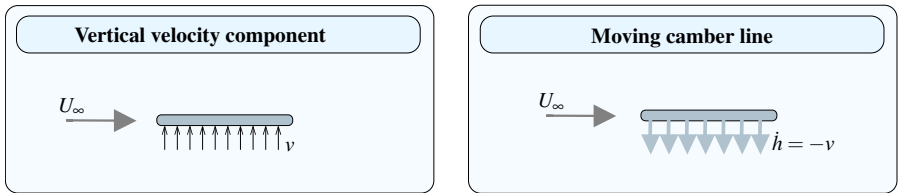
Figure 3.5.: Example of the interchangeability of boundary conditions in thin airfoil theory: A constant vertical velocity component v that appears at every point of the airfoil chord at the same time (left) imposes the same boundary condition as an airfoil, plunging with a purely vertical velocity $\dot{h} = -v$ (right).
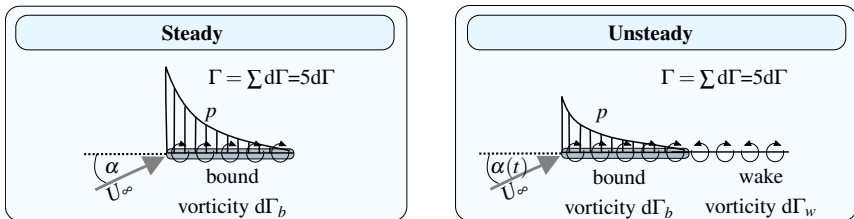
Figure 3.6.: Visualization of the considerations leading to unsteady thin airfoil formulation: Kelvins Theorem imposes the shedding of opposite sign vorticity in the wake if the boundary conditions on the airfoil are altered. This wake vorticity changes the airfoil's lift, compared to steady conditions.

related to the static pressure via Bernoulli's equation. Integration of the pressure distribution in terms of singularities yields the lift of the thin airfoil. The total bound circulation of the airfoil is proportional to the exhibited lift. According to Kelvin's circulation theorem (see for example Spurk [89]), the total circulation of a material contour is constant in time. In the unsteady case, the boundary conditions are time dependent. This leads to a time dependence of the integrated bound circulation. In order to fulfill Kelvin's circulation theorem for each change in bound circulation the same amount of opposite sign vorticity has to be shed in the flow. This shed vorticity in turn induces a tangential velocity on the airfoil that changes the pressure distribution and integrally alters the total lift.

Depending on the order of approximation of the surrounding flow and the linearization of the boundary conditions, solutions to the thin airfoil problem of different complexities can be derived. First-order transfer functions assume an uniform steady flow solution U_∞ and linearized boundary conditions. This leads to a complete uncoupling of steady and fluctuating flow and allows closed form solutions. Closed form solutions for selected boundary conditions, motivated by various physical inflow scenarios, were derived in the 1920s and 1930s and are still referred to today. According to Dowell [22] (p. 449) and Hodges and Pierce [35], these first-order transfer functions are the most commonly used design tool in unsteady aerodynamic engineering problems today. A detailed review of the different methods to obtain first-order transfer functions is provided by Johnston [41]. A schematic overview of the most common transfer functions is given in Figure 3.7. Solutions can be divided into the treatment in time domain and the treatment in frequency domain. The transient response of the airfoil to a perturbation in time domain is described by an impulse response function, the counterpart in frequency domain is a transfer function. Wagner [103] presented a time domain solution of an airfoil submitted to a sudden change in angle of attack. This is equivalent to a constant vertical velocity component imposed over the whole chord. The corresponding impulse response of the lift is referred to as Wagner function. Küssner [56] derived a time domain solution for the lift evolution due to a vertical traveling gust. This impulse response function is the Küssner function. Because it is more convenient for flutter calculations, similar results have been obtained in the frequency domain. Theodorsen [94] presented the frequency domain solution for an airfoil (with an aileron) oscillating sinusoidally
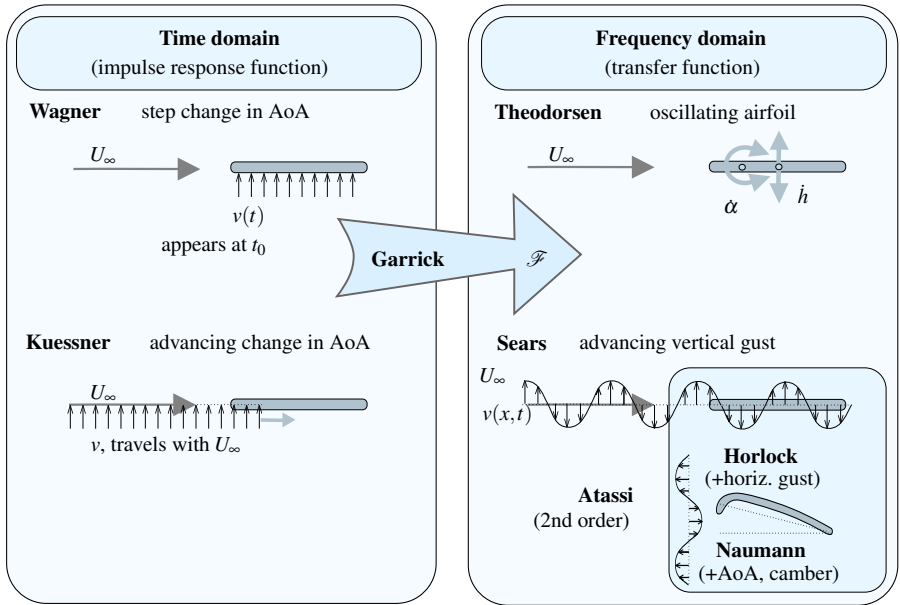
Figure 3.7.: Schematical representation of different boundary conditions leading to the classical first-order solutions in thin airfoil theory. Time domain and frequency domain solutions are connected by Fourier transformation.

with a small amplitude, using the perturbing vertical velocity component v as boundary condition. His solution is known as the Theodorsen function $C(k)$. An identical result was obtained by Schwarz [82], who imposed a corresponding movement of the camber line. Sears [83] introduced the transfer function for an airfoil entering a sinusoidal vertical gust. This transfer function is referred to as the Sears function $S(k)$. The relationship between impulse response functions in time domain and the transfer functions in frequency domain was pointed out by Garrick [25]. He showed that the Wagner function is connected to the Theodorsen function and that the Küssner function is connected to the Sears function by Fourier transformation. The linear assumptions in the derivation of thin airfoil first-order transfer functions allow the superposition of the results. Karman and Sears [102] presented the solution for a pitching and plunging airfoil entering a sharp edged gust. Sears [84] summarized the works of Küssner [56], Theodorsen [94] and Karman and Sears [102] and applied

them to a fan blade operating in the wake of other blades.

Recently, different authors have derived solutions for parts of the airfoil section instead of the whole airfoil, to investigate on the influence of flaps or a generally deforming camber line. Gaunaa [26] gave analytical expressions for the unsteady forces on an airfoil with variable geometry undergoing arbitrary motion. Johnston et al. [42] pursued a similar goal and submitted an airfoil with general deforming camber to a vertical gust. The case of an airfoil with adaptive camber mechanism, where the balance of moments around leading-edge and trailing flap defines the camber line was treated by Spiegelberg [88].

3.2.2. 1$^{\text{st}}$ Order Solutions for the Rigid Airfoil

As explained in section 3.2.1 the dynamic lift L_{dyn} differs from the quasi-steady lift L_{qs}, cf. Figure 3.6, p. 23. According to Karman and Sears [102] and graphically illustrated in Figure 3.8, L_{dyn} can be expressed as the complex sum of three different lift contributions:

- the quasi-steady lift L_{qs}

- the apparent mass lift $L_{\text{app. mass}}$ and

- the lift due to the presence of the wake L_{wake}.

The magnitude of each lift contribution corresponds to the vector length in Figure 3.8. The perturbing velocity v serves as a phase reference and is aligned with the real axis. The angle enclosed by the lift contribution vector and the real axis physically signifies the phase φ between the lift contribution and v. The quasi-steady lift L_{qs} is in phase with the velocity perturbation v. L_{qs} is produced by the bound circulation on the airfoil in the steady case and is obtained by steady thin airfoil theory. $L_{\text{app. mass}}$ physically signifies the lift due to fluid acceleration caused by the perturbing velocity v and leads v by $90°$. It is obtained by integrating the change of bound vorticity on the airfoil in the unsteady case. The lift contribution of the wake L_{wake} tends to diminish L_{dyn} and causes a lag behind v. Mathematically, L_{wake} is accounted for by the Theodorsen Function $C(k)$, derived by Theodorsen [94]. $C(k)$ is a complex function that depends on the reduced frequency k of the velocity perturbation v
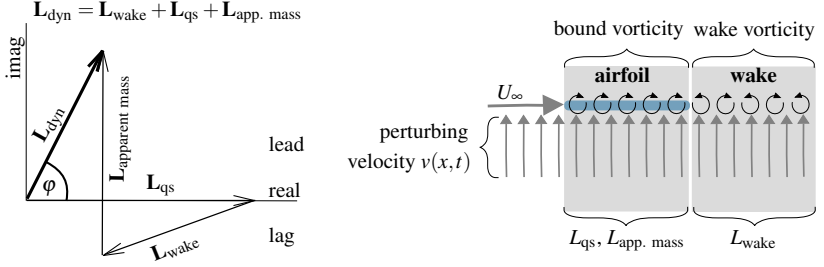
Figure 3.8.: Left: Vector diagram for the unsteady lift of an oscillating airfoil, adapted from Karman and Sears [102]. The dynamic lift is obtained by complex addition of different lift contributions: $\mathbf{L}_{dyn} = \mathbf{L}_{wake} + \mathbf{L}_{qs} + \mathbf{L}_{app.\ mass}$. The perturbing velocity $v(x,t)$ is aligned with the real axis and serves as a phase reference. Right: Representation of the origin of the lift contributions. The bound vorticity on the airfoil generates L_{qs} and $L_{app.\ mass}$, while the shed vorticity in the wake is responsible for L_{wake}.

only and is defined as

$$C(k) = F(k) + iG(k). \tag{3.6}$$

F and G are the real and the imaginary parts of C and are given in terms of Bessel functions of first and second-order, see Theodorsen [94]:

$$F(k) = \mathbb{R}[C(k)] = \frac{J_1(J_1 + Y_0) + Y_1(Y_1 - J_0)}{(J_1 + Y_0)^2 + (J_0 - Y_1)^2} \tag{3.7}$$

$$G(k) = \mathbb{I}[C(k)] = \frac{Y_1 Y_0 + J_1 J_0}{(J_1 + Y_0)^2 + (J_0 - Y_1)^2} \tag{3.8}$$

For harmonic velocity perturbations, the dynamic lift L_{dyn} can be expressed in terms of the perturbing velocity $v(x,t)$ and the Theodorsen function $C(k)$. Relating the dynamic lift L_{dyn} to the quasi-steady lift L_{qs} effectively normalizes the lift amplitude and yields the transfer function h.

$$h = \frac{L_{dyn}}{L_{qs}} = h(C(k), v(x,t)) \tag{3.9}$$

The magnitude of h is the ratio of the dynamic and quasi-steady lift amplitude and φ is the angle enclosed by the vector of L_{dyn} and the real axis in the complex plane.

$$|h(k)| = \left| \frac{\widehat{L}_{dyn}}{\widehat{L}_{qs}} \right|, \qquad \varphi = \arctan\left(\frac{\mathbb{I}(h)}{\mathbb{R}(h)} \right) \tag{3.10}$$

27

For quasi-steady conditions at $k = 0$, the dynamic lift equals the quasi-steady lift and $|h(k)| = 1$ and $\varphi = 0$. Under dynamic conditions, the lift contributions of L_wake and $L_\text{app. mass}$ alter $|h(k)|$ and φ. For a given $v(x,t)$, the transfer function h is a function of k only. Representing h as a vector in the complex plane and connecting all vectors of $h(k)$ for $k = 0 \to \infty$ yields the classical representation of aerodynamic transfer functions. Figure 3.9 shows such transfer functions for the flow situations of a plunging and pitching airfoil and a fixed airfoil submitted to a sinusoidal vertical gust. The evolution of h in terms of k depends on not solely on the imposed perturbation velocity v, but also on the definition of the quasi-steady lift L_qs and the choice of the reference system. Different authors use different definitions of the quasi-steady lift and the reference system, which sometimes leads to confusion. Table 3.1 gives an overview of the flow scenarios, corresponding boundary conditions, dynamic lift solutions and corresponding transfer functions relevant to this study. Parameters for the plunging airfoil are taken from Karman and Sears [102], for the pitching airfoil from Leishman [64] and the sinusoidal vertical gust problem is taken from Sears [84].

Experimental Transfer Function of the Pressure Difference

Most solutions of unsteady thin airfoil theory consider the unsteady lift response, which is the integral of the unsteady pressure distribution. The unsteady pressure distribution is an intermediate, but not often reported result when obtaining the unsteady lift response, as it is related to the tangential velocity on the airfoil surface via the unsteady Bernoulli equation. The tangential velocity is directly obtained from the singularity distribution on the airfoil's chord line and wake. Postel and Leppert [75] give an expression of the pressure distribution of an oscillating airfoil and Mateescu and Abdo [68] present a closed form solution for the same problem based on velocity singularities. Integration of the transfer function of the pressure distribution yields again the Theodorsen function.
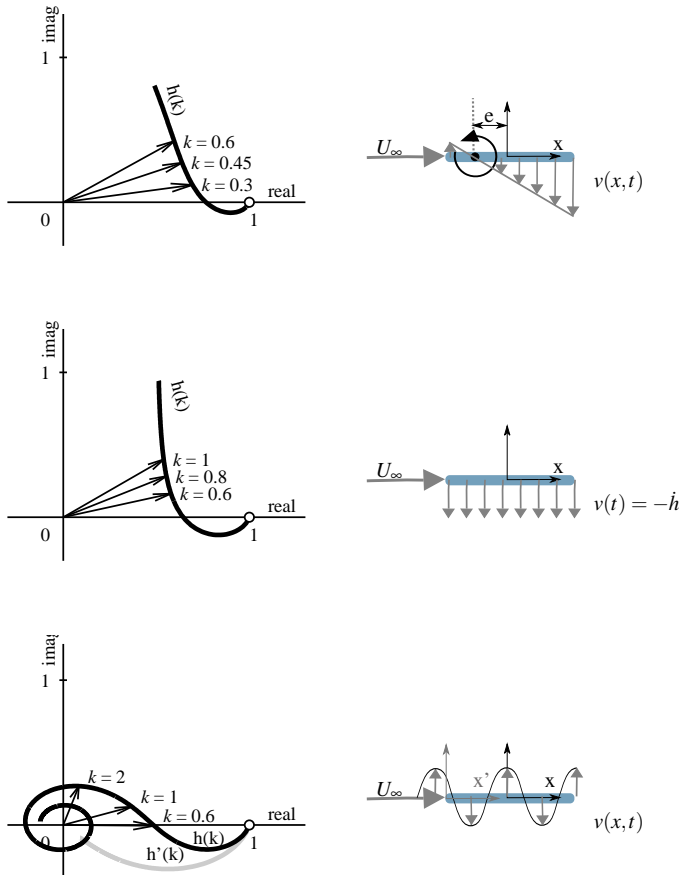
Figure 3.9.: Transfer function $h(k)$ in the complex plane for different velocity perturbations. Top: Pitch around elastic axis e, measured in half chords from the airfoil center. Middle: Plunge. Bottom: Sinusoidal vertical gust referenced to the mid-chord (black line) and to the leading-edge (gray line). The exact definitions of the perturbing velocity v and the definition of the quasi-steady lift L_{qs} are given in table 3.1. If not indicated otherwise, the reference system is fixed to the airfoil's mid-chord and distances are counted in semi-chords $b = c/2$.

Flow situation	Translatory oscillation (plunge) $h = \hat{h}e^{-i\omega t}$	Pitch around elastic axis e $\alpha = \hat{\alpha}e^{-i\omega t}$	Sinusoidal vertical gust $v = \hat{v}_g e^{-i\omega t}$
Perturbing velocity $v(x,t)$	$v(t) = -\dot{h} = -\frac{d}{dt}\left(\hat{h}e^{-i\omega t}\right)$ $= i\omega\hat{h}e^{-i\omega t} = i\omega h$	$v(x,t) = \dot{\alpha}(x-x_0) + \alpha U_\infty$	$v(x,t) = \hat{v}_g e^{-i(\omega t - kx)}$
Effective AoA amplitude $\hat{\alpha}_{\text{eff}}$	$\hat{\alpha}_{\text{eff}} = \tan\left(\frac{\hat{h}}{U_\infty}\right) \simeq \left(\frac{\hat{h}}{U_\infty}\right)$	$\hat{\alpha}_{\text{eff}} = \hat{\alpha}$	$\hat{\alpha}_{\text{eff}} = \tan\left(\frac{\hat{v}_g}{U_\infty}\right) \simeq \left(\frac{\hat{v}_g}{U_\infty}\right)$
Quasi-steady C_L $C_{L,\text{qs}} = 2\pi\hat{\alpha}_{\text{eff}}$	$2\pi\frac{\hat{h}}{U_\infty}$	$2\pi\hat{\alpha}$	$2\pi\frac{\hat{v}_g}{U_\infty}$
Quasi-steady lift $L_{\text{qs}} = C_{L,\text{qs}}\frac{\rho}{2}U_\infty^2 c$	$2\pi\frac{\rho}{2}U_\infty c\hat{h}$	$2\pi\frac{\rho}{2}U_\infty^2 c\hat{\alpha}$	$2\pi\frac{\rho}{2}U_\infty c\hat{v}_g$
Transfer Function $h(k) = \frac{L_{\text{dyn}}}{L_{\text{qs}}}$	$C(k) + i\frac{k}{2}$	$\left(1 + \left(\frac{1}{2} - e\right)ik\right)C(k) + \frac{1}{2}k(i - ke)$	$S(k) = (J_0 - iJ_1)C(k) + iJ_1$

Table 3.1.: Overview of the first-order transfer functions used in this study. The perturbing velocity is the relative velocity between airfoil surface and surrounding flow imposed by the airfoil motion or the oncoming gust. From this perturbing velocity an effective angle of attack amplitude $\hat{\alpha}_{\text{eff}}$ is calculated that serves to estimate the quasi-steady lift L_{qs}. Relating the dynamic to the quasi-steady lift yields the transfer function.

3.2.3. 1st Order Solutions for the Adaptive Camber Airfoil

In the following section, transfer functions of the adaptive camber airfoil from the work of Spiegelberg [88] are reviewed. Spiegelberg gives a complete description of the aeroelastic problem of a pitching and plunging adaptive camber airfoil submitted to a sinusoidal gust. In his notation, the adaptive camber airfoil possesses three degrees of freedom (heaving, pitching and flap-deformation), combined in the vector $\boldsymbol{p}$. It exhibits a normal force and a pitching moment, included in the force vector $\boldsymbol{f}$. These values can be non-dimensionalized and expressed in the force and moment coefficient vector $\boldsymbol{c}$. Bold letters mark vectors $\boldsymbol{y} = (y_1, y_2, y_3)$. Each vector component takes the form of a sinusoid $y_1 = \widehat{y}_1 \sin(\omega t + \varphi_{y_1})$ of amplitude $\widehat{y}_1$ and a phase φ_{y_1}. A transfer function $\boldsymbol{h}_{\text{(r)(e)}}$ connects a response of type $\mathbf{r}$ to an excitation of type $\mathbf{e}$. If only one vector component is considered, the transfer function reduces to

$$h_{re} = \frac{r}{e} = \frac{\widehat{r}}{\widehat{e}}\frac{e^{i\omega t + \varphi_r}}{e^{i\omega t}} = \frac{\widehat{r}}{\widehat{e}}e^{i(\omega t + \varphi_r) - i\omega t} = \frac{\widehat{r}}{\widehat{e}}e^{i\varphi_r} \tag{3.11}$$

The magnitude $|h_{re}| = \widehat{r}/\widehat{e}$ relates the amplitude of the response to the amplitude of the excitation. The argument $arg(h_{re}) = \varphi$ contains information about the phase between excitation and response. The response can consist of a motion or a (non-dimensional) force, the excitation can be a motion, a (non-dimensional) force or a sinusoidal gust. Here, only three experimentally accessible and for the description of the adaptive camber airfoil's performance relevant transfer functions are considered. Their relationship is visualized in Figure 3.10 and they are namely

- the **Aerodynamic Transfer Function** $h_{c_g g}$ that relates the non-dimensional aerodynamic forces c_g exhibited by a (rigid) airfoil to the fluctuating angle of attack due to a sinusoidal vertical gust g.

In the case of an airfoil with adaptive camber, aerodynamic forces are not only dependent on the inflow, but also on the shape of the airfoil, which is itself dependent on the aerodynamic forces. The aerodynamic transfer function is then replaced by

- the **Aeroelastic Transfer Function of the Load** $h_{c_f g}$ that relates the load response of the deformed adaptive camber airfoil c_f to the fluctuating angle of attack due to a sinusoidal vertical gust g.

The deformation of the adaptive camber airfoil is described by

- the **Aeroelastic Transfer Function of Motion** h_{pg} that connects the motion response p of the adaptive camber airfoil to the fluctuating angle of attack due to a sinusoidal vertical gust g.

The aeroelastic transfer function is also helpful for a prediction of the performance of the adaptive camber airfoil, as its load reduction capabilities depend largely on the amplitude and the phase of the trailing flap deflection.
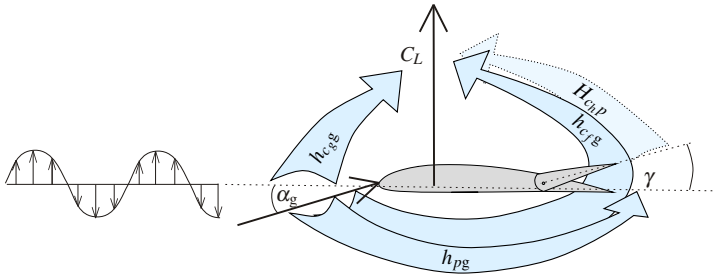
Figure 3.10.: Transfer functions in the aeroelastic system of the adaptive camber airfoil. The aeroelastic transfer function h_{pg} connects the adaptive camber airfoil's motion response to the fluctuating angle of attack. The load response is described by the aerodynamic transfer function $h_{c_g g}$.

For an adaptive camber airfoil fixed in a wind tunnel and submitted to a sinusoidal vertical gust, these three general transfer functions can be simplified. In order to facilitate a later comparison with experimental results, the notation is adapted to match the experimental notation. As the only considered excitation **e** is the excitation due to a gust, the index 'g' is omitted for clarity.

Transfer Function of the Load on a Rigid Airfoil of a Certain Shape

The aerodynamic transfer function $h_{c_g g}$ (Spiegelberg [88], p. 83) connects the non-dimensional aerodynamic forces due to a sinusoidal gust c_g to the corresponding sinusoidal gust α_g on an airfoil with a certain shape.

$$h_{c_g g} = \frac{c_g}{\alpha_g} \tag{3.12}$$

For the assessment of the adaptive camber airfoil in terms of gust load reduction, only the normal force is considered, and c_g that comprises force and moment coefficients, reduces to the lift coefficient C_L.

$$h_{c_g g} \rightarrow h_{L,\text{rigid}} = \frac{C_{L,\text{rigid}}}{\alpha_g} \tag{3.13}$$

$h_{L,\text{rigid}}$ is a function of the reduced frequency, the elastic axis and the airfoil shape. In the case of an airfoil with leading and trailing flap, the airfoil shape depends on the flap length and the flap deflections. If the flaps are set at $\gamma = 0°$, equation 3.12 is connected to the Sears function S (see Sears [83] or section 3.2.2) by

$$S = \frac{C_L}{\alpha_g (\partial C_L / \partial \alpha)} = \frac{h_{L,\text{rigid}}}{\partial C_L / \partial \alpha} = \frac{h_{L,\text{rigid}}}{2\pi} \tag{3.14}$$

where the lift curve slope is $\partial C_L / \partial \alpha = 2\pi$ according to steady thin airfoil theory.

Transfer Function of Motion

The aeroelastic transfer function $\boldsymbol{h}_{pg}$ (Spiegelberg [88], p. 87) connects the response of the airfoil's degree of freedom $\mathbf{p}$ (plunge, pitch and flaps) to the excitatory gust angle of attack α_g and is given as

$$\boldsymbol{h}_{pg} = \left(-\omega^{+2} \tilde{\boldsymbol{M}} + i\omega^+ \tilde{\boldsymbol{D}} + \tilde{\boldsymbol{K}} \right)^{-1} \boldsymbol{h}_{c_g g} (U^*)^2 \tag{3.15}$$

Retaining the formulation of Spiegelberg, the pitching eigenfrequency ω_2 is used to non-dimensionalize the equations of motion. $U^* = U_\infty / b\omega_2$ is the reduced free-stream velocity, $\omega^+ = \omega / \omega_2$ is the non-dimensional excitation frequency and b is half of the airfoil's chord length c. $\tilde{\boldsymbol{M}}$, $\tilde{\boldsymbol{D}}$ and $\tilde{\boldsymbol{K}}$ are the structural mass, damping and stiffness matrices of the system, respectively. The denominator on the right side $(-\eta^2 \tilde{\boldsymbol{M}} + i\eta \tilde{\boldsymbol{D}} + \tilde{\boldsymbol{K}})$ takes the classical form of the transfer function of a linear dynamical system. This highlights the influence of the structural parameters. $\boldsymbol{h}_{c_g}$ is the aerodynamic transfer function of the load for an airfoil of a certain shape, as defined above. Scaled with the dynamic pressure, $\boldsymbol{h}_{c_g g} (U^*)^2$ represents the influence of the aerodynamic properties on the adaptive camber airfoil's transfer function of motion. If the pitching and plunging degree of freedom are blocked, the vector $\mathbf{p}$

reduces to the flapping degree of freedom, represented by the trailing flap angle γ and the transfer function of motion can than be written as

$$\boldsymbol{h_{pg}} \rightarrow h_{\gamma} = \frac{\gamma}{\alpha_{\mathrm{g}}} \tag{3.16}$$

Transfer Function of the Load on the Adaptive Camber Airfoil

The aeroelastic transfer function $\boldsymbol{h_{c_f g}}$ (Spiegelberg [88], p. 92) connects the dimensionless aerodynamic forces on the adaptive camber airfoil to the gust angle of attack, while taking the deformation of the airfoil into account. It is defined as

$$\boldsymbol{h_{c_f g}} = \boldsymbol{H_{c_h p}} \boldsymbol{h_{pg}} + \boldsymbol{h_{c_g g}} \tag{3.17}$$

where $\boldsymbol{H_{c_h p}}$ is a matrix of transfer functions that connects the aerodynamic forces to the motion of the airfoil. Most entries of $\boldsymbol{H_{c_h p}}$ cannot be accessed in the performed experiments. Considering only the lift response to the flap degree of freedom, $\boldsymbol{H_{c_h p}}$ is reduced to $\frac{C_L}{\gamma}$. The transfer function of motion $\boldsymbol{h_{pg}}$ reduces to h_{γ} and the aerodynamic transfer function $\boldsymbol{h_{c_g g}}$ reduces to $h_{L,\mathrm{rigid}}$ as described above. The load response of the adaptive camber airfoil can than be written as

$$\boldsymbol{h_{c_f g}} \rightarrow h_{L,\mathrm{adaptive}} = \frac{C_L}{\gamma} \boldsymbol{h_{\gamma}} + h_{L,\mathrm{rigid}} = \frac{C_{L,\mathrm{adaptive}}}{\alpha_{\mathrm{g}}} \tag{3.18}$$

Where $\frac{C_L}{\gamma} \boldsymbol{h_{\gamma}}$ represents the load response to the flap motion due to the excitatory gust and $h_{L,\mathrm{rigid}}$ is the transfer function of the load for a certain airfoil configuration, as described above. The adaptive camber airfoil's load response can thus be described by the sum of the aerodynamic forces due to the deformation of the airfoil and the aerodynamic forces on the airfoil itself.

3.2.4. 2nd Order Solutions for the Rigid Airfoil

First-order transfer functions represent a thin flat plate without angle of attack at low speeds reasonably well. In most engineering applications however, these assumptions are violated. One important limitation is the assumption of a spatially constant steady velocity field. The physical origin of this non-uniform flow fields ranges from

shock waves in transonic flows over separated flows to the mere presence of a lifting airfoil. One possibility to account for the non-uniform steady velocity field are time linearized models, their solutions are referred to as **2nd order transfer functions**. Figure 3.11 graphically illustrates the differences between the assumptions leading to first- and second-order transfer functions.

1st order	2nd order
U_∞	$U_\infty(\vec{x})$
uniform constant velocity field	spatial variable velocity field
unsteady velocity field uncoupled	distorted perturbation
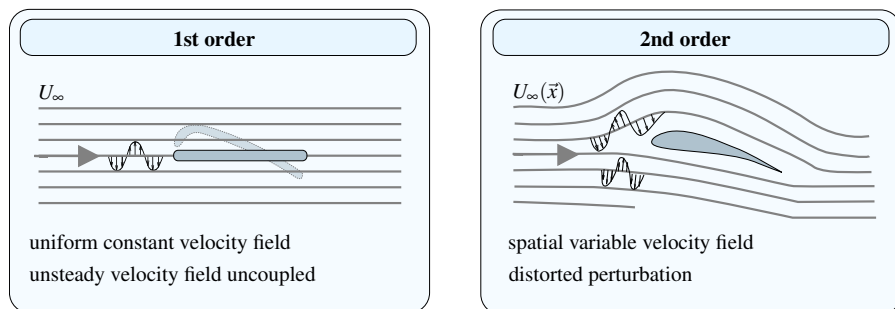
Figure 3.11.: Illustration of the different assumptions leading to first and second-order transfer functions. First-order transfer functions assume a spatially constant steady flow solution U_∞. Second-order transfer functions account for the distortion of the steady flow solution, for example due to the presence of a lifting airfoil.

First-order theories assume that the steady surrounding flow and the unsteady perturbations are not influenced by one another. The individual solutions of the surrounding flow and the perturbations are summed up to obtain the solution of the combined problem. Second-order theories are motivated by the idea that the steady velocity field around an airfoil couples back on a superimposed perturbation. If a perturbation passes through such a spatially variable velocity field, its characteristics are altered. Retaining the restrictions of small perturbations and potential flow assumptions, second-order solutions can be obtained by a combination of a solution for the spatially variable steady flow field and a perturbation approach (see e.g. Dowell and Hall [22], p. 453). Closed form solutions of second-order are more challenging to find and to some extend more complex in implementation than first-order models. Still, they are cheap with respect to computing power. Numerous second-order solutions have been derived for transonic flows and the associated compression shock and are widely accepted in the community. For the case of a lifting airfoil, only few and little noticed theories exist, although the physical motivation is identical: The pres-

ence of a lifting airfoil causes an acceleration of the flow on the suction side of the airfoil and a deceleration on the pressure side. An oncoming velocity perturbation propagates faster over the suction side, leading to an increased wavelength, compared to the pressure side. The sinusoidal shape is distorted. The coupling between the airfoil thickness and the oncoming gust was partially accounted for by Horlock [37]. He extended the solution of the Sears problem to a fluctuation in mainstream direction. Investigating the transfer functions for a flat plate under sinusoidal vertical and horizontal gusts, he found that a horizontal gust has only an influence on the airfoil response if the airfoil possesses a mean angle of attack. The influence of a small camber was added to Horlock's extension by Naumann and Yeh [72]. Goldstein and Atassi [29] accounted for the dependence of the fluctuating lift on the wavenumber of the gust in the direction perpendicular to the airfoil, caused by the distortion of the initial gust. For a flat plate of zero thickness, Goldstein's theory leads to a closed form solution that consists of a simple but important correction of Sears function. Atassi [4] used these results to derive specific lift formulas for an airfoil with zero thickness, camber and mean angle of attack. The airfoil is submitted to a velocity perturbation with vertical and horizontal components of the respective reduced frequencies k_1 and k_2. Atassi's closed form solution of the transfer function

$$h = \frac{L_{\text{dyn}}}{L_{\text{qs}}} = h_0 + \alpha\beta \cdot h_\beta + \alpha m \cdot h_m \tag{3.19}$$

can be constructed by linear superposition of the effects of airfoil thickness, camber αm and angle of attack $\alpha\beta$, despite the non-linearity of the underlying theory. The effect of airfoil thickness h_0 is found to be proportional to the Sears function S.

$$h_0 = \frac{k_1}{k} S(k_1) \tag{3.20}$$

with k being defined as $k = k_1 + ik_2$. The influence of camber h_m and angle of attack h_β depend in a complex way on the Sears, Hankel and Bessel functions, defined in terms of the reduced frequencies k_1 and k_2, as well as k_1 and k_2 themselves.

$$h_\beta = f(S(k_1), k_1, k_2), \qquad h_m = f(S(k_1), k_1, k_2) \tag{3.21}$$

For explicit formulas, the reader is referred to Atassi [4], p.116.

36

3.2.5. Literature Review of Experimental Investigations
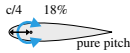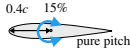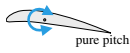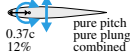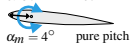
Despite the extensive use of first-order transfer functions in engineering applications, very little experimental validation has been performed. This section provides an overview of a thorough research of relevant literature on this topic. For an airfoil oscillating in pitch and/or plunge, the so-called **Theodorsen problem**, a hand full of experiments were performed in the middle of the 20th century. These experiments aimed to experimentally verify the Theodorsen function, which is the first-order solution to this problem. Second-order solutions of the Theodorsen problem, namely for transonic flows, became popular in the 1980s and a couple of validation experiments were performed at this time. While measuring transient forces on an oscillating airfoil is a difficult task, generating repeatable two-dimensional fluctuating inflow is even more challenging. Accordingly fewer attempts to experimentally verify of the so-called **Sears problem**, an airfoil encountering a sinusoidal vertical gust, have been performed. Experimental work concerned with the Theodorsen problem is discussed first, followed by an overview of the experimental validation of the Sears problem. The different objectives, investigated parameters and setups of the experiments make a direct comparison of the results difficult. In order to provide an overview and give orientation, a table summarizes the discussed work.

Theodorsen problem of an oscillating airfoil

Table 3.2 summarizes the work discussed on the experimental validation of the Theodorsen problem. The first two columns give information about the author and the experiment. The last two columns comment on the agreement of the obtained results with the Theodorsen function in terms of magnitude and phase.

In 1939, Silverstein and Joyner [87] investigated the phase of the dynamic lift response of a symmetric two-dimensional airfoil of 0.127 m (5 in) chord and 18 % thickness. The airfoil was pitched around its quarter chord with a reduced frequency of $0.06 < k < 2$. According to Theodorsen, the dynamic lift of an airfoil in this setup lags the excitation for small reduced frequencies. Then a change in phase occurs at $k = 0.15$ and the unsteady lift leads the excitation for higher reduced frequencies. Silverstein found acceptable agreement with theory for higher reduced frequencies

Table 3.2.: Overview of the experimental investigations on pitching and plunging airfoils. The last two columns indicate agreement with the Theodorsen function.

Author	Exp. setup	Parameter	Magnitude	Phase
Silverstein 1939	c/4 18% pure pitch	$k = 0.06 - 2$	not investigated	underpredicted
Reid 1940	0.4c 15% pure pitch	$0 < k < 0.7$	ok	ok
		$0.7 < k$	opposite	opposite
Bratt 1945	pure pitch	pitching moment	opposite	opposite
Halfmann 1952	0.37c 12% pure pitch pure plunge combined	pure motion	ok	ok
Rainey 1957	0.5c 10% α_m pure pitch	small α_m	ok	ok
		high α_m	opposite	opposite
Davis 1957	0.25c 10% $\alpha_m = 4°$ pure pitch	transsonic	opposite	opposite

above $k = 0.2$. For low excitation frequencies, where theory predicts a lag of the unsteady lift, he found the unsteady lift to lead. A lag was never observed in his experiments.

One year later, Reid [78] pitched four NACA 0015 profiles of different chord length and elastic axis with an oscillation amplitude of $\pm 2°$ and oscillation frequencies between $6.66 < f < 10$ Hz. The reduced frequency was varied by changing the oscillation frequency, chord length and inflow speed. For reduced frequencies above $k = 0.7$, he found rather good quantitative agreement of both the magnitude and the phase of the dynamic lift response. Below reduced frequencies of $k = 0.7$, magnitude and phase of the dynamic lift response varied in a sense opposite to that predicted by linear theory.

In 1945, Bratt [12] investigated the effect of mean angle of attack, oscillation amplitude, shape and aspect ratio on the dynamic response of the pitching moment. He did not comment on the lift response, but found substantial quantitative and qualitative discrepancies to linear theory especially at higher mean angles of attack and high

oscillation amplitudes for the pitching moment response.

In 1952, Halfmann [31] examined a two-dimensional NACA 0012 airfoil of 0.305 m (1 ft) chord and 0.61 m (2 ft) span in pure pitch, pure plunge, and combined pitch/plunge motion with and without a mean angle of attack. The airfoil was pitched around its 0.37c axis with an oscillation amplitude of $\pm 6.7\,°$ and $\pm 13.5\,°$ at reduced frequencies between $0.05 < k < 0.46$. For the pure motions, Halfmann observed good agreement of theoretical and experimental data, with larger deviations for small reduced frequencies.

In 1957 Rainey [77] oscillated a two-dimensional NACA 65A010 airfoil in pitch around its mid-chord and reported on the magnitude and phase of the dynamic lift and moment response. The reduced frequency was varied between $0.2 < k < 0.63$ at Mach numbers of $M = 0.35$ and 0.7 and different mean angles of attack. He observed a clear dependence of the transfer functions on the Mach number and the mean angle of attack, which is not accounted for in first-order theory. The best agreement of experiments and theory was observed for small Mach numbers and low mean angles of attack in both phase and magnitude of the transfer functions. For high mean angles of attack above $\alpha_\mathrm{m} = 4\,°$, the experimentally derived transfer functions showed a behavior inverse to the theoretical transfer functions of Theodorsen. While the magnitude of the unsteady lift was supposed to decrease with increasing reduced frequency, Rainey observed a significant increase. The phase, which is supposed to change from a lag to a lead at $k = 0.25$, changed from a lead to a lag. At high Mach numbers, the qualitative behavior of the transfer functions was acceptable for small angles of attack, but systematically under predicted by theory.

Taking into account the effects of compressibility, Leishman [62] compared impulse response functions of second-order of the normal force and pitching moment to experimental data originating from different authors. The experimental data depended significantly on the airfoil shape and Mach number. Even though his second-order transfer functions are not of closed form and were tuned with experimental data, he observed a significant discrepancy between theory and experiment, especially at low reduced frequencies.

Davis and Malcolm [20] examined an oscillating NACA 64A010 airfoil under transonic conditions for low reduced frequencies below $k = 0.4$ to investigate the effect of compressibility on transfer functions. The airfoil was pitched around its quarter
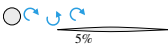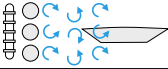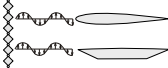
chord with an amplitude of $1°$ about a mean angle of attack of $\alpha_m = 4°$ and a Mach number of $M = 0.8$. The experimental transfer functions differed significantly from the theoretical first-order functions and Davis and Malcolm underlined the importance of Mach number effects.

A comparison among the different experiments is difficult due to differences in the experimental setups such as airfoil shape (thickness and camber), type of motion (pitch, plunge or combined), mean incidence angle, amplitude of oscillation, the location of the elastic axis, aspect ratio, Reynolds number and Mach number. Nevertheless, some overall conclusions can be drawn. In none of the experiments does the experimentally derived transfer function match the theoretical transfer function quantitatively and qualitatively in amplitude and phase. The best agreement is found by Halfmann, but even his data differs by about 30% from theoretical values. The largest discrepancies are observed at small reduced frequencies. Generally, the agreement between theory and experiment is best for small mean angles, moderate reduced frequencies and low Mach numbers. In the case of a lifting airfoil with $\alpha_m \neq 0°$, experimentally obtained transfer functions show a completely different behavior than the one obtained by first-order approximations.

Sears Problem of an oscillating inflow

Table 3.3 summarizes the discussed work on the experimental validation of the Sears problem. As above, the first two columns provide information on the author and the experimental setup. The last two columns state on the general agreement of the experimental results with the Sears function in terms of magnitude and phase.

Table 3.3.: Overview of the experimental investigations on airfoils in an oscillating air stream. The last two columns state on the agreement with the Sears function.

Author	Exp. setup	Parameter	Magnitude	Phase
Commerford 1973	5%	$k = 3.9$	under-predicted	ok
Larose 1999		$0.1 \leq k \leq 0.7$	opposite	not investigated
Hatakana 2002		$0.01 \leq k \leq 0.8$	overpredicted opposite	not investigated

The first attempt to verify the Sears function was carried out by Commerford and Carta [18] in 1973. They used the wake of a cylinder to approximate a sinusoidal vertical gust. The vortex shedding frequency of a cylinder is proportional to the in-flow velocity, hence the reduced frequency is fixed for one setup ($k = 3.9$, in their case). Phase and magnitude of the dynamic lift response for this reduced frequency were taken at different mean angles of attack. The magnitude was underpredicted by theory; the error was in the order of 50 - 100 %, the phase agreed better. No correlation of the phase or magnitude with the mean angle of attack was observed.

In civil engineering gust loadings and aeroelastic response are of importance for the stability of buildings. Typically, structures used in civil engineering are bluff bodies such as cylinders or building blocks, which do not fall in the category of slender, lifting surfaces. Bridge decks however can be abstracted as a non-symmetric edgy airfoil. One famous example, illustrating that these structures are also subject of aeroelastic phenomena such as flutter is the collapse of the Tacoma Narrows Bridge in 1940. Motivated by the need for a correct modeling of gust loads on bridge decks, Larose [58] measured the aeroelastic response of such a bridge deck in 1999. The Deck, resembling a tick and edgy airfoil, was mounted on a wind tunnel balance and submitted to turbulent inflow, generated upstream by large spires and a fixed grid. The transfer function, referred to as admittance in the community of civil engineering, was derived from a power spectra. Hence, only a comparison of the magnitude is possible, phase information is lost. Laroses experimental data showed a behavior

not predicted by theory. While the Sears function decreases steadily with increasing frequency, the experimental values increased with increasing frequency until a maximum at $k = 0.02$ was reached and decreased afterwards.

Also motivated by bridges Hatanaka and Tanaka [33] sought to verify the Sears function in 2002.They submitted a two-dimensional NACA 0012 airfoil and a flat box bridge deck to large scale turbulence employing an active gust generator. Comparing the magnitude of the admittance functions for very low reduced frequencies of 0.01 < k < 0.8 to the theoretical values of the Sears function, they found the experimental values to be under predicted by theory, especially for low reduced frequencies. In the case of the bridge deck, they even observed an increase in magnitude above the quasi-steady value of 1, while theory always predicts dynamic values inferior to their quasi-steady counterpart, due to the positive aerodynamic damping of the wake.

Despite the small number of data sets, it can be concluded that linear first-order transfer functions do not account for all effects contributing to the dynamic lift response of an airfoil in an oscillating flow. In the case of symmetric non-lifting surfaces, theory and experiments agree reasonably well. Non-symmetric, lifting surfaces are not captured by first-order theory.

3.3. Detached Flow Regime

In attached flow, the unsteady airfoil response depends only on the reduced frequency k and can be described by linear transfer functions. Increasing the mean angle of attack such that the fluctuating angle of attack surpasses the static stall angle results in a domination of viscous forces over pressure forces. A non-linear dependence of the airfoil response on the perturbation, accompanied by high force excursions, is observed. This phenomenon is commonly referred to as dynamic stall and the main events during the **dynamic stall cycle** are explained in subsection 3.3.1. It has been known for a long time that animals exploit dynamic stall during flapping flight. For some technical applications such as micro air vehicles, exploiting the high lift might be advantageous. If dynamic stall occurs unintentionally, as it can be the case on helicopter or wind turbine blades, the high fluctuating loads can be destructive. For this reason, a correct prediction of the dynamic loads is of interest for industry

and research. Current approaches to **model dynamic stall** are briefly summarized in section 3.3.1. In contrast to the few systematic experimental investigations of the dynamic airfoil response in attached flow regime that were presented in section 3.2.5, numerous experimental studies of the dynamic airfoil response above the static stall angle have been carried out. A **review of experimental investigations** focusing on aspects relevant to this study is given in subsection 3.3.2 and parameters that influence vortex behavior during dynamic stall are presented. The section closes with a discussion of prospective **implications for the adaptive camber airfoil** regarding dynamic stall.

3.3.1. Dynamic Stall Cycle

In 1932, Kramer [54] was the first to observe that an airfoil generates higher lift under dynamic conditions for a short period of time than it does under steady conditions. It took until the 1970s for Carr, McAlister and McCroskey [15,16,69] to relate the force history on a dynamically oscillating airfoil to the presence of vortical structures. Pitching a NACA 0012 airfoil dynamically above its static stall angle, they observed the cycle of events schematically displayed in Figure 3.12:

At stage ⓐ, flow reversal appears at the airfoil's surface and large eddies begin to form in the boundary-layer. The lift continues to increase at a constant rate. At ⓑ, flow reversal spreads over the airfoil and a coherent vortex forms near the leading-edge. During ⓒ, this leading-edge vortex (LEV) moves towards the trailing-edge. The airfoil's lift curve slope increases and exceeds the static value of 2π. At ⓓ the vortex passes the airfoil's trailing-edge and a rapid lift breakdown is observed, followed by full stall at ⓔ. During downstroke ⓕ, the flow begins to reattach and the lift value approaches its initial value, forming a hysteresis loop.

In their work, Carr, McAlister and McCroskey investigated different airfoil geometries, Reynolds numbers, oscillation frequencies and oscillation amplitudes. Macroscopically, they observed similar force histories over a wide range of parameters, which lead Carr to his vision: 'to introduce the possibility of a method that may allow the prediction of engineering parameters without exhaustive dynamic testing of an airfoil'. However, Carr already pointed out that although force cycles and macroscopic vortex behavior are similar, the underlying physical mechanisms of formation,
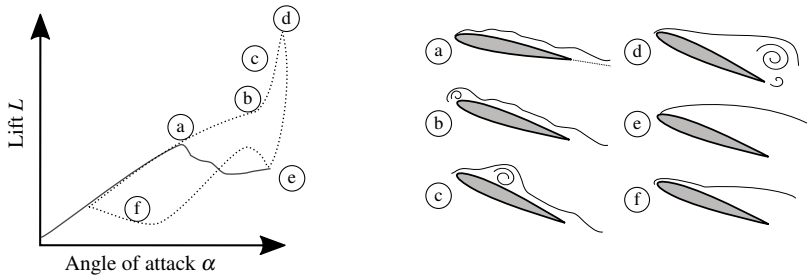
Figure 3.12.: Dynamic stall cycle on a continuously pitching NACA 0012 airfoil, adapted from Carr et al. [15]. The left side shows the quantitative behavior of steady (rigid line) and dynamic lift (dotted line). The corresponding flow structures for typical points of the dynamic stall cycle are depicted on the right.

growth, propagation and detachment might differ significantly.

Modeling of Dynamic Stall

During dynamic stall, reversed flow and vortical structures appear and viscous forces become predominant. The potential flow approximations that lead to the derivation of thin airfoil theory and transfer functions in attached flow regime, cf. section 3.2, p. 22, are no longer justified. Numerous extensions to attached thin airfoil theory that phenomenologically model dynamic stall exist. Larsen et al. [59] categorize these attempts in three groups:

- Models that take basic physical relationships into account,
- models that modify the lift curve in a certain manner and
- models that modify the effective angle of attack.

Dynamic stall is a highly complex phenomenon that still lacks full understanding. Its characteristics depend on various parameters and none of the developed dynamic stall models is universally valid. All have to be tuned with a significant number of empirical coefficients obtained from experiments. From these semi-empirical dynamic stall models, the Beddoes-Leishman model [65], developed by Leishman and Beddoes, is the most established. Like most dynamic stall models, the Beddoes-Leishman model was initially developed to predict fluctuating loads on helicopter

blades. Wind turbines operate at smaller Mach number and have thicker airfoil profiles than helicopters. Momentum effects due to compressibility and leading-edge separation can be neglected. Hansen et al. [32] adapted the Beddoes-Leishman model for wind turbine applications. For deformable airfoils, Andersen et al. [2] coupled Hansen's model to Gaunaa's [26] thin airfoil solution of an airfoil with deformable trailing-edge in unsteady flow. For an airfoil with adaptive camber mechanism, no dynamic stall model exists so far. Holierhoek et al. [36] and Larsen et al. [59] compare different semi-empirical dynamic stall models, amongst them the Beddoes-Leishman model. Although tuned with experimental coefficients, none of the semi-empirical dynamic stall models captured the phenomenon accurately.

Contrary to semi-empirical models, higher order numerics do not have to be tuned with experimental coefficients. Kitsios et al. [49] compared two-dimensional simulations and three-dimensional LES models. They found that the less cost intensive two-dimensional calculations are not capable of resolving turbulent separation during dynamic stall adequately. LES models show better agreement with experimental observations, but the need of a third dimension makes them more costly in terms of computing time. Ekaterinaris and Platzer [23] reviewed commonly used LES schemes and their solutions and found that the obtained lift depends on the accurate prediction of laminar to turbulent boundary-layer transition as well as the point of boundary-layer separation. The underlying physics of these processes are yet not completely understood, which encourages experimentalists to investigate the subject.

3.3.2. Literature Review of Experimental Investigations

Influencing Parameters of Coherent Vortex Development

Several different vortex shedding mechanisms exist and their occurrence depends on a set of parameters which influence and depend on each other, namely the frequency and the amplitude of the airfoil oscillation, the kind of motion (pitch, plunge, combined, rotational), the Reynolds number, the two-dimensionality of the problem (interaction with tip vortices), the time history (interaction with wake vortices), the airfoil shape (thickness and camber), leading-edge geometry and the two-dimensionality of the flow. Numerous studies have been performed, investigating the influence of
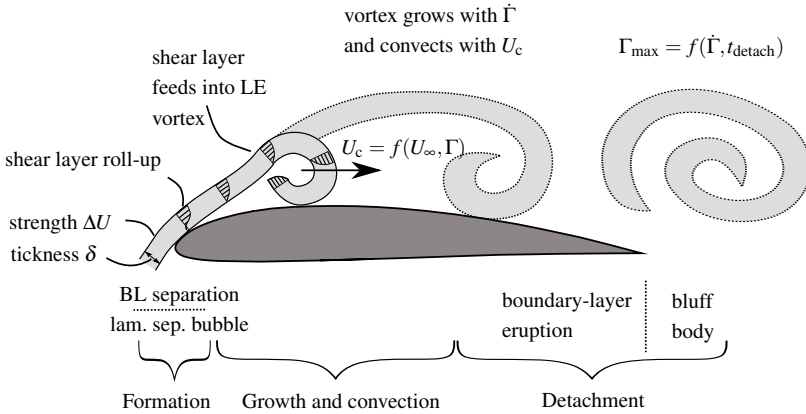
Figure 3.13.: Schematic overview of parameters governing the dynamic stall cycle in the two-dimensional case: Vortex formation is initialized by boundary-layer separation or a laminar separation bubble. The shear layer rolls up and feeds into a LEV. The LEV grows at a rate $\dot{\Gamma}$ and accumulates circulation Γ as it convects downstream with the convection velocity U_c. The vortex detaches by boundary-layer eruption or by bluff body mechanism at its maximum circulation Γ_{max}

more or less isolated parameters on more or less isolated quantities during one of the regimes. Shyy et al. [86] give a good overview of research performed before 2010 on the subject for the flapping wing cases. Akkala [1] gives an extensive review of recent research on rigid airfoils. Some basic relationships and key findings necessary to understand the complexity of the subject are visualized in Figure 3.13. The vortex life cycle can be roughly divided into four stages: vortex formation, growth, convection and detachment. Basic physical relationships and influence parameters during each of the stages are summarized below.

It is common understanding that **vortex formation** occurs at the leading-edge due to a roll up of the shear layer. The shear layer roll up is contributed to two different mechanisms. According to Carr et al. [15] and McCroskey et al. [69], the airfoil's leading-edge shape and the airfoil's camber determine which vortex formation mechanism takes place. They investigated a sinusoidally pitching NACA 0012 with different leading-edge geometries. Shear layer roll up due to boundary-layer separation and due to the burst of a laminar separation bubble were observed. The boundary-

layer separation mechanism is the most commonly observed reason for shear layer roll up. As the angle of attack increases, the stagnation point moves on the pressure side of the airfoil away form the leading-edge. The outer flow has to overcome a higher pressure gradient when passing the leading-edge on the suction side. When the momentum of the boundary-layer is not sufficient to overcome the pressure gradient, flow reversal occurs and a coherent LEV starts to form at the leading-edge. The second mechanism leading to shear layer roll up is the separation bubble mechanism. Theoretical considerations to this mechanism are given by Cebeci et al. [17]: the outer flow adapts almost instantaneously (with the speed of sound) to the higher pressure gradient, since it can be seen as non-viscous. The boundary-layer around the airfoil however is dominated by viscous effects and reacts much slower to the changes imposed by the incoming flow and a separation bubble is formed out of which the LEV develops. In both mechanisms, the shear layer strength and pressure difference around the airfoil's leading-edge are key parameters.

During **vortex convection** from the airfoil's leading-edge towards its rear part, the LEV remains connected to the leading-edge via the feeding shear layer. The convection of the LEV is slower than the mainstream velocity U_∞. According to McCroskey et al. [69], the convection velocity is in the order of $U_c \sim 1/3\text{-}1/4 \ U_\infty$. A simple formula for the convection velocity is given by Doligalski et al. [21], obtained from the convection of an infinite vortex line over an infinite wall $U_c = U_\infty - \frac{\Gamma}{4\pi a}$, where a is the distance of the LEV to the wall. The convection velocity depends thus mainly on the inflow velocity U_∞ and the circulation of the vortex Γ.

The circulation of the LEV Γ is determined by the **vortex growth rate** $\dot{\Gamma}$. It is commonly accepted that the main source of vortex growth is the shear layer that feeds into the LEV and its strength and thickness are key parameters that influence vortex growth. Already Carr et al. [16] anticipated the importance of the relationship between the feeding shear layer in the dynamic stall cycle: 'The mechanism by which the boundary-layer vorticity transfers into the tight, strong vortex ... is probably the key to stall modification'. Widmann and Tropea [105] used the Falkner-Skan solution to estimate the shear layer thickness δ and found the vortex growth rate to scale with the integrated vorticity flux over the shear layer thickness. Other authors found

the feeding shear layer to be an important, but not the only source that transfers vorticity into the leading-edge vortex. Wojcik and Buchholz [108] performed a flux analysis on a rotating blade. They concluded that opposite sign vorticity is drawn into the LEV from the surface on a rotating blade, which regulates LEV circulation and causes the vortex to remain close to the airfoil's surface. Since the flow on a rotating blade is three dimensional by definition, Wojcik and Buchholz did not further investigate out-of-plane vorticity flux. Panah et al. [73] confirmed the findings of Wojcik and Buchholz and quantified the flux of negative vorticity to be approximately half of the positive vorticity flux coming from the feeding shear layer. They additionally found that there is a small but non-negligible out-of-plane vorticity flux on two-dimensional plunging flat plates, especially at high reduced frequencies of up to $k = 2.09$.

At some point, the LEV is cut from the feeding shear layer and **vortex detachment** takes place. Different mechanisms leading to vortex detachment exist. Their occurrence depends mainly on the ratio of the convection velocity U_c of the LEV to the stroke period of the airfoil. The definition of the reduced frequency illustrates the problem. The reduced frequency relates the convection time of a particle in the undisturbed outer flow to the time of one airfoil oscillation. For high reduced frequencies, the airfoil performs several oscillations, while the particle passes the airfoil. For low reduced frequencies, the particle 'sees' only a small part of the oscillating motion, while it passes the airfoil. Similar considerations can be made for the LEV that convects with a velocity $U_c < U_\infty$ over the airfoil. For high oscillation frequencies, the vortex has only convected over a small part when the angle of attack is inverted. For low oscillation frequencies, the vortex reaches the TE before the angle of attack is inverted. Mulleners and Raffel [71] performed high speed PIV on a harmonically pitching airfoil. They found two different regimes, dependent on whether the LEV can reach the airfoil's trailing-edge or not. Light dynamic stall was observed if the angle of attack was inverted before vortex reaches trailing-edge. Deep dynamic stall was observed if the LEV had time to reach the airfoil's trailing-edge. The physical reason for this phenomena was studied in more detail by Widmann and Tropea [105]. They investigated pitching and plunging flat plate airfoils at constant reduced frequency, Strouhal number and Reynolds number, with variable chord length. Two

detachment mechanisms were found, the bluff body mechanism and the boundary-layer eruption. In the first case, the vortex is able to reach the plate's trailing-edge, where it interacts with a counter rotating trailing-edge vortex and detaches. This regime was found for low reduced frequencies, where the vortex had enough time during downstroke to reach the trailing-edge. At high reduced frequencies, where the vortex was too slow to reach the trailing-edge, the boundary-layer eruption process was observed.

The **maximal circulation** $\Gamma_{\max}$ of a LEV is determined by the vortex growth rate and the time until vortex detachment occurs. In the case of bluff body detachment, Widmann [105] found the chord length c of the flat plate airfoil to be the limiting factor in vortex growth. In this case, $\Gamma_{\max}$ scales with $\dot{\Gamma}$ and c . If the vortex detaches via boundary-layer eruption, the limiting factor in vortex growth is the time of vortex detachment. According to Gharib et al. [28], the time of vortex detachment can be approximated by the maximal dimensionless formation time $\hat{T}$. A forming vortex accepts vorticity flux until a maximal dimensionless formation time of $\hat{T} = \frac{C\Gamma}{D\Delta U}$ is reached. C is a constant factor depending on the physical configuration of the vortex generator, ΔU quantifies the strength of the shear layer and D is a characteristic length scale. For a plunging plate, a maximal dimensionless formation time of $\hat{T} = 4$ has been reported. Beyond this time, additional vorticity flux is rejected and a secondary vortex forms instead. These considerations are confirmed by Rival et al. [80], who found vortex formation times of $4.4 < \hat{T} < 5.0$ for modified and pure sinusoidal plunging motions of an asymmetric SD7003 airfoil. If the vortex detaches by boundary-layer eruption, $\Gamma_{\max}$ scales hence with $\dot{\Gamma}$ and $\hat{T}$.

The Relationship Between Coherent Vortices and Aerodynamic Forces

Ever since Carr, McAlister and McCroskey's [15, 16, 69] investigations in the 1970s, agreement exists that the force excursion during dynamic stall is caused by the presence of vortical structures. The exact relationship between vortical structures and dynamic lift has only recently been quantified. Jones and Babinsky [44] related the normalized circulation of coherent vortical structures on an unsteady rotating flat plate wing to measured lift and drag forces. They found a proportionality between the

unsteady lift and the normalized circulation of the coherent LEV for all investigated wing kinematics. Beyond the static stall angle, when the first LEV is formed, lift and normalized circulation increase linearly. After the first LEV separates, both lift and normalized circulation drop rapidly. A second coherent LEV starts to form. Lift and normalized circulation increase again, but with a smaller rate and to a smaller maximal value than in the first vortex shedding cycle. Only very recently, Akkala [1] combined time resolved PIV and surface pressure measurements to relate the vortical structures to the pressure distribution exhibited by a plunging plate. He found the LEV to have a very localized influence on the lift. The LEV causes a suction peak underneath its center which enhances as the LEV grows in size and accumulates circulation. The suction peak propagates downstream towards the trailing-edge along with the convecting LEV. The suction peak disappears as the LEV detaches and is drawn away by the outer flow. Akkala showed the lift due to the presence of the vortex to be about 40 % of the total lift and to be produced very locally, in the direct vincinity of the LEV.

Understanding and effective manipulation of vortex life, its formation, its growth and its maximal size during dynamic stall can be the key to lift control on dynamically oscillating airfoils.

3.3.3. Implications for the Adaptive Camber Airfoil

Significant differences of the dynamic stall cycle on the rigid and the adaptive camber airfoil are expected only if the aerodynamic forces are high enough to actuate the adaptive camber mechanism. According to Akkala [1] the LEV induces a very localized suction peak in its vicinity that contributes approximately 40 % to the total dynamic lift. The adaptive camber airfoil is designed to operate in the attached flow regime. Since the dynamic lift in detached flow is typically higher than lift in attached flow and the LEV is formed on the leading-edge, the suction peak induced by the LEV is presumed to be sufficiently high to actuate the adaptive camber mechanism. The key parameter in LEV formation, growth and convection during dynamic stall is the feeding shear layer. This feeding shear layer is manipulated by the adaptive camber airfoil and its rotatable leading-edge. The no-slip condition alters the velocity difference between airfoil surface and outer flow, which is an important fac-

tor in shear layer strength. Additionally, the combined flap motion alters the airfoil's camber, which alters the pressure gradient over the airfoil. It can thus be anticipated that a rotating leading-edge and the change of camber will have significant impact on all stages in the LEV life cycle.

4. Sinusoidal Vertical Gust Experiment

In this thesis, two different wind tunnel experiments are performed to assess the adaptive camber airfoil's gust load alleviation performance under unsteady conditions. This chapter is concerned with the first experiment, the sinusoidal vertical gust encounter. The experimental approach is schematically visualized in Figure 4.1.
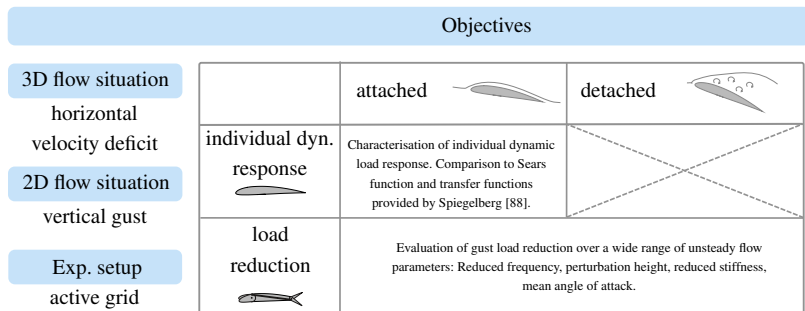
Figure 4.1.: Schematic visualization of the pursued experimental approach.

In the rotating frame of a wind turbine a horizontal velocity deficit expresses itself as a vertical gust on the blade section. Horizontal velocity deficits are frequently encountered by wind turbine blades. The cyclic passage of the blade through the atmospheric boundary-layer or through the tower shadow corresponds to a horizontal velocity deficit. Also, horizontal wind gusts or large scale turbulence provoke these kind of perturbations that are responsible for a majority of the fatigue loading. Accordingly, the sinusoidal vertical gust presents an important test case for the gust load alleviation performance on the two-dimensional adaptive camber airfoil. The first objective of this chapter is to

- evaluate the adaptive camber airfoil's gust load alleviation performance over a wide range of unsteady flow parameters.

All experiments are performed in the University of Oldenburg's active grid wind tunnel. This facility offers the unique opportunity to generate vertical sinusoidal gusts of variable wavelength. The reduced frequency of the perturbation can be varied while keeping all other parameters constant. Thereby, the influence of gust frequency, gust amplitude, reduced system stiffness and mean angle of attack can be studied individually. In attached flow conditions, the sinusoidal vertical gust encounter of a rigid airfoil corresponds to the theoretical formulation of the Sears problem. It is discussed in section 3.2.5, p. 37 that the corresponding transfer function, the Sears function, still lacks systematic experimental validation in terms of frequency dependence. The same holds for the transfer function of the adaptive camber airfoil encountering a sinusoidal vertical gust given by Spiegelberg [88] and presented in section 3.2.3, p. 31. The experimental setup offers the opportunity to

- verify the first-order transfer functions of the Sears problem on the rigid and adaptive camber airfoil in terms of reduced frequency dependence.

The **experimental setup**, comprising the Oldenburg active grid wind tunnel and the adaptive camber airfoil model, is presented in section 4.1. A description of the **objectives and investigated parameter space** is given in section 4.2, followed by an explanation of the procedure of **data acquisition and reduction** in section 4.3. The obtained **experimental results** are presented in section 4.4.

4.1. Experimental Setup

First, the **active grid wind tunnel** at the university of Oldenburg and the generated dynamic inflow are presented. Then, the **adaptive camber airfoil** model used in the experiments is briefly introduced.

4.1.1. Active Grid Wind Tunnel
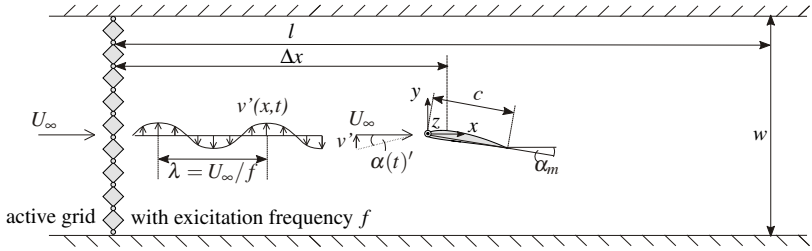
Figure 4.2.: Top view of the experimental setup: The active grid upstream the test section allows the generation of sinusoidal vertical gusts of variable amplitude and frequency. An airfoil equipped with adaptive camber mechanism is installed on a wind tunnel balance downstream the active grid. The gust angle of attack α_g is measured with a cross wire prior to the airfoil experiments at the airfoil's leading-edge position ($x = 0$, $y = 0$, $z = h/2$).

Figure 4.2 shows a schematic overview of the experimental setup. The wind tunnel has a closed test section of $w = 1\,\mathrm{m}$ width, $h = 0.8\,\mathrm{m}$ height and $l = 2.6\,\mathrm{m}$ length. An active grid is installed in front of the test section to generate variable, yet repeatable turbulence of large scales. The active grid consists of nine vertical and seven horizontal axes with square flaps. Each axis is driven individually by a stepper motor according to a control protocol. More information about the active grid and its performance is given by Knebel et al. [51]. Only the vertical axes of the active grid are used to generate two-dimensional periodic fluctuations in v' in y-direction, while blockage and the mainstream velocity U_∞ in x-direction are kept nearly constant. The velocity fluctuations, from now on referred to as sinusoidal vertical gust, are approximated by

$$v' = \widehat{v}_g \sin\left(2\pi f t\right) = \widehat{v}_g \sin\left(\omega t\right) \tag{4.1}$$

The gust has an amplitude of $\widehat{v}_g$ and is uniform in z−direction over the wind tunnel height. Together with the constant mainstream velocity and a small angle approximation, this results in sinusoidal, two-dimensional angle of attack variations

$$\alpha' = \widehat{\alpha}_g \sin(2\pi f t) = \widehat{\alpha}_g \sin(\omega t) \tag{4.2}$$

The frequency f of the gust and the angle of attack oscillation coincides with the excitation frequency of the active grid. The angular frequency ω used in the theoretical deviation of first-order transfer function in section 3.2, p. 22 is related to the excitation frequency of the grid by $\omega = 2\pi f$. The gust amplitude $\widehat{v}_g$ and angle of attack amplitude $\widehat{\alpha}_g$ depend on the amplitude of the oscillation of the active grid middle axis and are adjustable by changing the active grid's control protocol. A two-dimensional airfoil with adaptive camber mechanism is mounted vertically on a three-component wind tunnel balance $\Delta x = 1.1$ m behind the active grid, reaching from wind tunnel top to bottom. The airfoil can be rotated around its c/4-axis to change its mean angle of attack α_m. The total fluctuating angle of attack is then

$$\alpha = \alpha_m + \alpha' = \alpha_m + \widehat{\alpha}_g \sin(2\pi f t). \tag{4.3}$$

All parameters in equation 4.3 (α_m, $\widehat{\alpha}_g$ and f) as well as the inflow velocity U_∞ can be varied individually. This allows a systematic investigation of the influence of all parameters on the individual airfoil response and on the gust load alleviation capabilities of the adaptive camber airfoil.

4.1.2. Adaptive Camber Airfoil

A picture of the adaptive camber airfoil model is shown in Figure 4.3. The airfoil has a Clark Y section with a chord length of $c = 0.18$ m and span of $s = 0.8$ m. It is manufactured from polyamide by direct laser sintering. The coupling mechanism is completely incorporated in the airfoil. To avoid very short levers and minimize backlash, a two rod coupling system is chosen. The restraining spring system, schematically shown in Figure 4.4, is realized by tension springs. The total system stiffness κ can be varied from 0 to 23 Nm/rad in 16 discrete steps. The maximal pre-cambering moment is $M_0 = 2.4$ Nm. A detailed report on the construction of the model is given by Brötz [13]. Two different airfoil configurations are tested, from now on referred

to as configuration $\textcircled{a}$ and configuration $\textcircled{b}$. Both configurations are schematically shown in Figure 4.4. Configuration $\textcircled{a}$ has a system stiffness of $\kappa = 2.88$ N/rad and a pre-cambering moment of $M_0 = 0.28$ Nm. When no flow is present, the airfoil has a maximal cambering of $\gamma = 15°$, limited by mechanical stoppers. Configuration $\textcircled{b}$ is twice as stiff ($\kappa = 5.76$ Nm/rad). The springs are mounted in the restraining spring mechanism in such a way that no pre-cambering moment is exhibited ($M_0 = 0$ Nm). Without flow being present, the airfoil has the original Clark Y airfoil shape ($\gamma = 0°$). The airfoil is equipped with two pressure taps at the suction and pressure side, located at the leading edge flap at $x/c = 0.09$. Pressure differences are taken at two spanwise positions $y/s = 0.33$ and $y/s = 0.66$, in order to check on the two-dimensionality of the flow during the unsteady experiments. Steel tubes are glued underneath the airfoil's polyamide skin and pressure taps are drilled through the skin and the steel tubes. The steel tubes are connected to *First Sensor HCL* differential pressure sensors via plastic hoses. Pressure sensors connected to the suction side possess a full scale of 25 mbar, those connected to the pressure side have a 12.5 mbar full scale. The sensor output signals of 20 mV is amplified to the maximal input of the data acquisition device with in-house fabricated adjustable amplifiers in order to obtain maximal resolution. The trailing flap angle γ serves as a measure for the deformation of the adaptive camber airfoil and is monitored by an *ams AS5162* rotary hall sensor. The sensor provides a linear analog output over a full turn of 360° and allows a programming of start and stop positions in order to increase full scale resolution for smaller measurement ranges. Start and stop positions are set at the maximal and minimal flap deflections, to optimally exploit the data acquisition device input range.

Figure 4.3.: Picture of the adaptive camber airfoil model used in the Oldenburg active grid wind tunnel experiments. The two rod coupling mechanism is chosen to minimize backlash and is restrained by a spring system (not shown).

(a) Configuration ⓐ
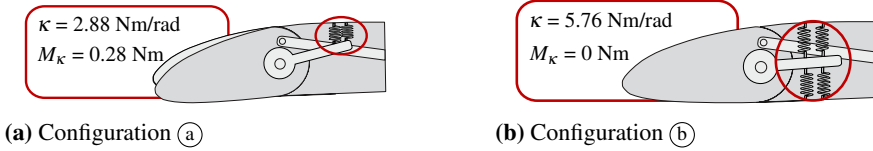
(b) Configuration ⓑ

Figure 4.4.: Schematic representation of the adaptive camber airfoil's restraining spring system: In configuration ⓐ, the springs are mounted asymmetrically leading to a pre-cambering of the airfoil. In configuration ⓑ, the springs are mounted symmetrically. No pre-cambering moment is applied and the adaptive camber airfoil has the original Clark Y airfoil profile.

4.2. Objectives and Investigated Parameter Space

The active grid wind tunnel offers the unique opportunity to vary individual parameters of the unsteady flow, while keeping all other parameters constant. An extensive investigation is carried out, varying the mean angle of attack α_m, the gust amplitude $\widehat{\alpha}_g$, the gust frequency f, the inflow velocity U_∞ and the configuration of the adaptive camber airfoil's restoring spring system. The rigid and the adaptive camber airfoil are submitted to equally fluctuating inflow. The individual airfoil response is assessed by comparing the dynamic lift response to quasi-steady approximations. The gust load alleviation potential is assessed by comparing the dynamic lift responses of the rigid and the adaptive camber airfoil. This section provides an overview of all experimentally varied parameters. Table 4.1 shows all performed measurements. The experiments are divided into three sets. Each set is carried out for the rigid and the adaptive camber airfoil, the corresponding objectives are described below.

Set ① - Influence of the mean angle of attack α_m
In set ① the adaptive camber airfoil is investigated in two different configurations of the restraining spring system, the suppler and pre-cambered configuration ⓐ and the stiffer configuration ⓑ without pre-camber. In this set, the airfoils are tested over the whole range of mean angle of attack α_m. The mean angle of attack is varied from $-10° < \alpha_m < 20°$ in steps of $2°$ by rotating the airfoil around its c/4 axis. At each α_m, the airfoil is submitted to the same dynamic inflow, keeping the gust amplitude at $\widehat{\alpha}_g = 6.2°$ and gust frequency at $f = 5\,\mathrm{Hz}$. This is done for two different inflow

velocities $U_\infty = 10\,\mathrm{m/s}$ and $U_\infty = 15\,\mathrm{m/s}$, which leads to two different reduced frequencies k and two different reduced stiffnesses κ^+ for each adaptive camber airfoil configuration. The intention of this set is twofold: The theoretical transfer functions are independent of α_m due to the linearity of the underlying theory, as discussed in section 3.2.1. The first intention is to verify this assumption. The second intention is to test the adaptive camber airfoil's performance over all possible flow regimes of attached and detached flow. From the experimental data, three different mean angles are identified that represent different flow regimes: $\alpha_\mathrm{m} = 2\,^\circ$, $8\,^\circ$ and $14\,^\circ$. For $\alpha_\mathrm{m} = 2\,^\circ$, the total fluctuating angle of attack remains completely below the static stall angle. For $\alpha_\mathrm{m} = 8\,^\circ$, the total fluctuating angle of attack passes the static stall angle during each load cycle and for $\alpha_\mathrm{m} = 14\,^\circ$ the fluctuating angle of attack remains almost completely in the region of detached flow. At these three α_m, further investigations on the influence of the gust amplitude, excitation frequency and inflow velocity are carried out.

Set ② - Influence of the gust amplitude $\widehat{\alpha}_\mathrm{g}$

In set ② the influence of the gust amplitude is studied. In the other sets, the excitatory gust amplitude is set to $\widehat{\alpha}_\mathrm{g} = 6.2\,^\circ$. The choice for such a high gust angle amplitude is motivated by the fact that the adaptive camber airfoil needs a certain driving aerodynamic moment. The theoretical transfer functions are derived using linear theory of small perturbations. The theory assumes that a small change in angle of attack $\alpha_\mathrm{m} + \widehat{\alpha}_\mathrm{g}$ leads to a change in airfoil response, such that the ratio of excitation and response stays constant. The theoretical transfer function h is thus independent of the gust amplitude $\widehat{\alpha}_\mathrm{g}$. Having this in mind the question arises, whether the assumption of small perturbations is fulfilled for a gust amplitude of $\widehat{\alpha}_\mathrm{g} = 6.2\,^\circ$ and whether the experimental airfoil response is also independent of $\widehat{\alpha}_\mathrm{g}$. For an airfoil in pure pitching motion it was shown by Halfmann [31] that the influence of the pitch amplitude is insignificant compared to the influence of mean angle of attack or airfoil shape. In fact, he even observed a slightly better agreement with theory for high pitching amplitudes of $\widehat{\alpha}_\mathrm{p} = 13.5\,^\circ$ than for smaller amplitudes of $\widehat{\alpha}_\mathrm{p} = 6.7\,^\circ$. For a vertical gust encounter, no experimental data concerning the influence of the gust angle amplitude $\widehat{\alpha}_\mathrm{g}$ is available. To fill this gap, measurement set ② is performed. At five different gust amplitudes $\widehat{\alpha}_\mathrm{g} = 4.5\,^\circ, 5.7\,^\circ, 6.6\,^\circ, 7.7\,^\circ$ and $8.5\,^\circ$ experiments

Table 4.1.: Overview of the parameter variations during the experimental campaign.

	No influence according to 1st order theory		Influence on parameters used in 1st order theory		Parameters used in 1st order theory			Procedure and purpose
Set	Mean angle of attack α_m in [°]	Gust amplitude $\hat{\alpha}_g$ in [°]	Inflow velocity U_∞ in [m/s]	Gust frequency f in [1/s]	Reduced frequency $k = \frac{\pi f c}{U_\infty}$ in [-]	Reduced stiffness $\kappa^+ = \frac{2}{c^2}\frac{\kappa_f}{\rho U_\infty^2}$ in [-] config. (a)	config. (b)	
①	$-10:2:20$	6.2	10	5	0.28	1.5	3	α_m is varied by pitching the airfoil around its c/4 axis. In linear theory, α_m has no influence on the transfer functions.
			15		0.19	0.65	1.3	
	Influence of mean angle of attack α_m							
②	2, 8, 14	4.5, 5.7, 6.6, 7.7, 8.5	10	5	0.28	1.5		$\hat{\alpha}_g$ is varied by changing the oscillation amplitude of the active grid. In linear theory, $\hat{\alpha}_g$ has no influence on the transfer functions.
			12.5		0.23	0.95		
			15		0.19	0.65		
			17.5		0.16	0.48		
			20		0.14	0.37		
	Influence of gust amplitude $\hat{\alpha}_g$					configuration (a)		
③	2, 8, 14	6.2	10	$2:1:6$	$0.11\ldots0.34$	1.5		k is varied either by changing f or U_∞. For a distinct U_∞, the reduced stiffness κ^+ is constant and the influence of f can be studied individually.
			12.5	$2:1:6$	$0.09\ldots0.28$	0.95		
			15	$2:1:9$	$0.08\ldots0.23\ldots0.34$	0.65		
			17.5	$2:1:6$	$0.06\ldots0.19$	0.48		
			20	$2:1:6$	$0.05\ldots0.17$	0.37		
	Dependence on excitation frequency f					configuration (a)		

are carried out at a constant gust frequency of $f = 5\,\text{Hz}$. The inflow velocity is varied between $10\,\text{m/s} < U_\infty < 20\,\text{m/s}$ in steps of 2.5 m/s. This results in five different reduced frequencies and simultaneously in five different reduced system stiffnesses, as both variables depend on U_∞.

Set ③ - Influence of the Reduced Frequency k

In set ③, the influence of the reduced frequency k is studied. The reduced frequency is proportional to the ratio of the excitation frequency f and the inflow velocity U_∞. In the case of a rigid airfoil, the transfer function depends on the reduced frequency only. As long as the ratio f/U_∞ stays constant, the transfer function remains unchanged. In the case of the adaptive camber airfoil, an additional dependence of the transfer function on the reduced system stiffness κ^+ exists and the transfer function depends on the dynamic pressure. The active grid offers the opportunity to change f independently from the U_∞. In this way, the reduced frequency k can be varied without changing the reduced system stiffness κ^+, which is convenient for the assessment of the adaptive camber airfoil. Additionally, the influence of f and U_∞ on k can be studied individually. To do this, the excitation frequency is changed from $2\,\text{Hz} < f < 6\,\text{Hz}$. This is done for five different inflow velocities of $10\,\text{m/s} < U_\infty < 20\,\text{m/s}$. For $U_\infty = 15\,\text{m/s}$, additional measurements at excitation frequencies of up to 9 Hz are performed. In this way, set ③ forms a good basis to verify theoretical transfer functions of the rigid and the adaptive camber airfoil. This is particularly interesting, as the Sears function and the corresponding transfer function on the adaptive camber airfoil still lack a systematic experimental validation.

4.3. Data Acquisition and Reduction

Measurements linked to the airfoil (pressure transducers and trailing flap angle) are collected with a *NI 6210* A/D converter, operating at an input range of 5 V. Wind tunnel data are recorded with a *NI 6281* A/D converter and wind tunnel balance data with a *NI 6211* A/D converter. The corresponding measurement uncertainties are given in appendix A.1. All data are sampled at a sampling frequency of $f_\text{s} = 1000\,\text{Hz}$ over a period of $T = 30\,\text{s}$. For stationary measurements, a simple arithmetic mean is taken to describe the measuring point. For the dynamic measurements, the post

processing of the raw data is explained in the following section. In section 4.3.1, the **phase averaging and synchronisation** procedure is described. The dynamic airfoil response is characterized using **experimental transfer functions**. Their derivation from experimental data is explained in section 4.3.2. For a quantitative assessment of the adaptive camber airfoil's load reduction capabilities, the **load reduction factor** is defined in section 4.3.3.

4.3.1. Phase Averaging and Synchronization

The flow behind the active grid is periodic with the excitation frequency f of the active grid. Even though the repeatability from period to period is good, it is superimposed by random processes. To find mean values for one load cycle and to improve the signal-to-noise (SNR) ratio, a phase averaging is applied. Each measured time series X, sampled at a sampling rate f_s over a time interval T_s, is divided into N segments. Each segment has the length $T = 1/f$ and comprises one load cycle. All cycles are summed up and averaged, resulting in a phase averaged quantity $\tilde{X}$

$$\tilde{X}\left(\tilde{t} = 0...\frac{1}{f}\right) = \frac{1}{N}\sum_{n=1}^{N} X\left(t = \frac{n-1}{f}....\frac{n}{f}\right). \tag{4.4}$$
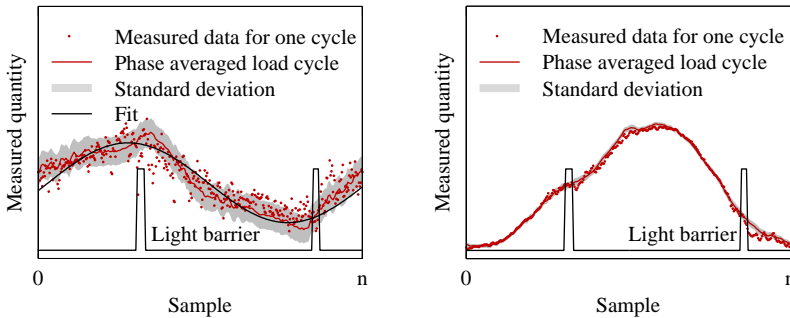
(a) Hotwire data   **(b)** Airfoil lift

Figure 4.5.: All acquired data are phase averaged. Light barrier signals from the active grid's middle axis, acquired during both hotwire (a) and load measurements (b), allow a synchronization of the airfoil response and the instantaneous angle of attack.

This is done with hotwire measurements as well as with the subsequently measured airfoil response. Figure 4.5 shows instantaneous data for one cycle, as well as the phase averaged value of the same quantity. In Figure 4.5a, hotwire data are shown and Figure 4.5b shows the airfoil's lift response. The hotwire data for one load cycle exhibits high scatter due to the turbulent nature of the flow. The phase averaging separates fluctuations due to random processes from fluctuations present in every load cycle. The phase averaged data contains only repeatable large scale information and yields a significant improvement of the signal-to-noise ratio. Integral measured variables such as the lift, shown in Figure 4.5b, are less sensitive to small scale turbulence. These variables scatter less around their phase averaged mean. The narrower gray band graphically illustrates the smaller standard deviation at one point in time from load cycle to load cycle. During both hotwire and airfoil measurements, light barrier signals from the active grid's middle axis are taken. Their location allows a synchronization of the airfoil's load response and the instantaneous angle of attack. If not indicated otherwise, all presented data are phase averaged mean values, shifted to match the phase of a pure sinusoidal change in angle of attack.

4.3.2. Experimental Transfer Functions

The exemplary shown phase averaged data of Figure 4.5 reveals a phase lag between the instantaneous angle of attack and the dynamic airfoil response. Additionally, the dynamic airfoil response differs in terms of amplitude from quasi-steady approximations. This difference is conveniently described with transfer functions. The derivation of two different experimental transfer functions is described in this section: The **transfer function of the motion**, which characterizes the shape response of the adaptive camber airfoil, and the **transfer function of the load** which relates dynamic lift of the adaptive camber or the rigid airfoil to its quasi-steady counterpart. The experimentally obtained transfer functions correspond to the theoretically derived transfer functions of section 3.2.3. An asterisk distinguishes between theoretical transfer functions h and experimental transfer functions h^*.

Experimental Transfer Function of Motion h_γ^*

The experimental transfer function of motion h_γ^* is derived by relating the adaptive camber airfoil's fluctuating trailing flap angle γ' to the fluctuating gust angle of attack α'. When submitted to a fluctuating inflow at the total angle of attack

$$\alpha(t) = \alpha_\mathrm{m} + \alpha' = \alpha_\mathrm{m} + \widehat{\alpha}_\mathrm{g} \sin(\omega t) \tag{4.5}$$

the adaptive camber airfoil de-cambers to a mean trailing flap angle of γ_m and oscillates around this mean angle, such that the total trailing flap angle is

$$\gamma = \gamma_\mathrm{m} + \gamma' = \gamma_\mathrm{m} + \widehat{\gamma}\sin\left(\omega t + \varphi_\gamma\right). \tag{4.6}$$

Following the definition of the theoretical transfer function 3.2.3, p. 31, the transfer function of motion h_γ^* can be written as

$$h_\gamma^* = \frac{\widehat{\gamma}}{\widehat{\alpha}_\mathrm{g}} \frac{e^{i(\omega t + \varphi_\gamma)}}{e^{i\omega t}} = \frac{\widehat{\gamma}}{\widehat{\alpha}_\mathrm{g}} e^{i(\omega t + \varphi_\gamma) - i\omega t} = \frac{\widehat{\gamma}}{\widehat{\alpha}_\mathrm{g}} e^{i\varphi_\gamma}. \tag{4.7}$$

The amplitude ratio $\frac{\widehat{\gamma}}{\widehat{\alpha}_\mathrm{g}}$ and the phase angle φ_γ between fluctuating angle of attack α' and the fluctuating trailing edge angle γ' are derived from the phase averaged measurements. The experimental transfer function of motion h_γ^* corresponds then to the theoretical transfer function of motion $\boldsymbol{h}_\gamma$ derived by Spiegelberg [88]. The transfer function of motion is the dynamic counterpart to the quasi-steady rate of de-cambering $(\partial\gamma/\partial\alpha)_\mathrm{qs}$. Its magnitude $|h_\gamma^*|$ can be interpreted as the inverse of the dynamic stiffness, or rather a dynamic system elasticity. The phase φ_γ between trailing flap response and perturbing angle of attack corresponds to the combined time delay caused by sensor, controller and actuator in active systems.

Experimental Transfer Function of the Load h_L^*

The quasi-steady lift L_qs is traditionally displayed over the angle of attack α, while the dynamic lift L_dyn is naturally displayed over time. When the dynamic lift is transfered to the quasi-steady representation and displayed over the (instantaneous) angle of attack, as in Figure 4.6a, the difference between quasi-steady and dynamic lift response is revealed: The dynamic lift forms an oval loop around the quasi-steady values. This hysteresis is due to the phase difference φ_L between dynamic lift response

and instantaneous angle of attack. The hysteresis loop is tilted, which corresponds to a difference of the quasi-steady and dynamic lift amplitudes $\widehat{L}_{qs} - \widehat{L}_{dyn}$. Likewise, the quasi-steady lift can be displayed for a time series of angle of attack $\alpha(t)$ over time, as in Figure 4.6b. In this representation, the phase difference and the difference of the lift amplitudes can be recognized. Both representations of Figure 4.6 contain the same information: the quasi-steady lift response L_{qs} and the dynamic lift response L_{dyn} differ in terms of amplitude $\widehat{L}$ and phase φ_L.
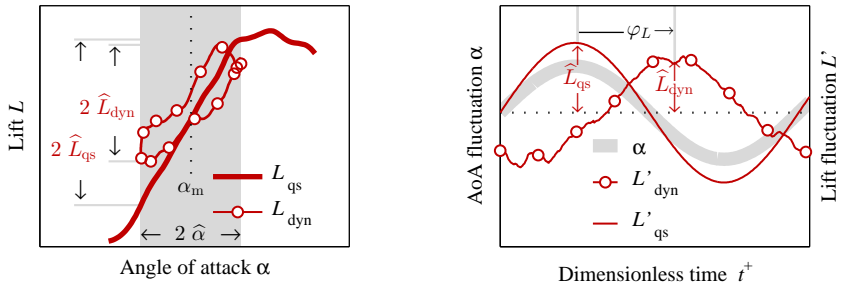
(a) Representation of the dynamic and quasi-steady lift in terms of angle of attack α.

(b) Representation of the same quantities over the dimensionless time t^+

Figure 4.6.: The experimental transfer function of the load h_L^* is derived by assigning the quasi-steady lift approximation to the measured dynamic lift response. The phase angle φ_L is the phase shift of the two curves, the amplitude ratio gives the magnitude of the transfer function h_L^*.

Traditionally, transfer functions relate an input to an output signal. Here, the input signal is the fluctuating angle of attack α', the output signal is the airfoil's lift response L_{dyn}. Adopting the approach of the theoretically derived first-order transfer functions of the load of section 3.2, the dynamic airfoil response is not related to the fluctuating angle of attack but to the quasi-steady lift response L_{qs} of the airfoil. In the quasi-steady assumption, the airfoil's lift response is proportional to the instantaneous angle of attack $\alpha(t)$. This effectively leads to a normalization of the transfer function. Following the definition of the theoretical transfer function 3.2.3, p. 31, the

experimental transfer function of the load h_L^* is defined as:

$$h_L^* = \frac{\widehat{L}_{\mathrm{dyn}} e^{i(\omega t + \varphi_L)}}{\widehat{L}_{\mathrm{qs}} e^{i\omega t}} = \frac{\widehat{L}_{\mathrm{dyn}}}{\widehat{L}_{\mathrm{qs}}} e^{i(\omega t + \varphi_L) - i\omega t} = \frac{\widehat{L}_{\mathrm{dyn}}}{\widehat{L}_{\mathrm{qs}}} e^{i\varphi_L} \tag{4.8}$$

The magnitude of the transfer function of the load corresponds to the ratio of the dynamic and the quasi-steady lift amplitude

$$|h_L^*| = \frac{\widehat{L}_{\mathrm{dyn}}}{\widehat{L}_{\mathrm{qs}}}. \tag{4.9}$$

For values of $|h_L^*| < 1$, the dynamic lift is smaller than its quasi-steady value. The quasi-steady lift amplitude $\widehat{L}_{\mathrm{qs}}$ is derived from quasi-steady measurements

$$\widehat{L}_{\mathrm{qs}} = \frac{\partial L}{\partial \alpha} \cdot \widehat{\alpha}_{\mathrm{g}}, \tag{4.10}$$

where $\frac{\partial L}{\partial \alpha}$ is the lift curve slope in the linear region of the lift curve and $\widehat{\alpha}_{\mathrm{g}}$ is the gust amplitude. The dynamic lift amplitude $\widehat{L}_{\mathrm{dyn}}$ and the phase angle φ_L between the fluctuating angle of attack α_{g} and the lift response L_{dyn} are derived directly from phase averaged measurements

$$L_{\mathrm{dyn}}(t) = \widehat{L}_{\mathrm{dyn}} \sin\left(\omega t + \varphi_L\right). \tag{4.11}$$

For positive values of φ_L, the load response leads the excitatory gust input. The transfer function of the load h_L^* is derived for the adaptive camber airfoil $h_{L,\mathrm{ad}}^*$ and the rigid airfoil $h_{L,\mathrm{rig}}^*$ individually. $h_{L,\mathrm{ad}}^*$ and $h_{L,\mathrm{rig}}^*$ are related to the theoretical transfer functions $h_{L,\mathrm{ad}}^* = h_{L,\mathrm{ad}}/2\pi$ and $h_{L,\mathrm{rig}}^* = h_{L,\mathrm{rig}}/2\pi = S$, where S is the Sears function. The experimental and theoretical transfer functions provide phase information in relation to the gust angle of attack. As the gust travels over the airfoil with U_∞, a reference point has to be chosen. In the experiments, this reference point is set at the airfoil's leading-edge, as hotwire measurements are performed at this position. In the deviation of first-order transfer functions, the phase reference is traditionally set at the airfoil's mid chord. This is accounted for by an additional phase shift, see Figure 3.9, p. 29.

4.3.3. Load Reduction Factor

A measure for the fluctuation around a mean value is the standard deviation. The normalized difference in standard deviation of the rigid and the adaptive camber airfoil's lift response

$$LR = \frac{\sigma\left(L_{\text{dyn,rigid}}\right) - \sigma\left(L_{\text{dyn,adaptive}}\right)}{\sigma\left(L_{\text{dyn,rigid}}\right)} \tag{4.12}$$

serves as a measure for the effectiveness of the adaptive camber airfoil's performance in terms of gust load alleviation, as proposed by Lambie [57]. For a purely sinusoidal dynamic load response, the standard deviation is connected to the amplitude by the factor of $\sqrt{2}$ and the load reduction factor reduces to

$$LR = \frac{\frac{\widehat{L}_{\text{dyn,rigid}}}{\sqrt{2}} - \frac{\widehat{L}_{\text{dyn,adaptive}}}{\sqrt{2}}}{\frac{\widehat{L}_{\text{dyn,rigid}}}{\sqrt{2}}} = \frac{\widehat{L}_{\text{dyn,rigid}} - \widehat{L}_{\text{dyn,adaptive}}}{\widehat{L}_{\text{dyn,rigid}}} \tag{4.13}$$

A load reduction factor of $LR = 1$ means that all fluctuations are alleviated by the adaptive camber airfoil. For equally fluctuating loads on the adaptive camber and the rigid airfoil, the load reduction factor takes the value of $LR = 0$. Negative values of LR indicate enhanced fluctuating loads on the adaptive camber airfoil, compared to the rigid reference airfoil.

4.4. Experimental Results

The mean aerodynamic properties of an airfoil in non-uniform flow differ from the behavior under uniform inflow conditions. For example, gliders perform better in turbulent than in calm air. The so-called Knoller-Betz effect or Katzmeyr effect was theoretically described by Knoller [52] in 1913 and experimentally verified by Katzmayr [47] in 1922. An airfoil, placed in an air stream, exhibits a directed force. By definition, the part of this force in flow direction is called drag, the part perpendicular to the flow direction is called lift. If the flow direction is altered, so is the direction of lift and drag. The fact that the drag is typically an order of magnitude smaller than the lift results in a perceived diminuation of the mean drag in a fluctuating air stream, if the reference system is not varied with the instantaneous angle of attack. This is

neither the case in a sailplane nor in the experimental setup, where the wind tunnel balance constitutes the laboratory fixed reference system. The same systematic error occurs when looking at the lift, but to a smaller extend. For a rigid airfoil, the difference between mean dynamic and steady lift is negligible. The same holds for the adaptive camber airfoil, which is justified in appendix C.1. In this study the airfoils performance is characterized by its lift only. Mean dynamic lift and quasi-steady lift are very similar on the rigid and the adaptive camber airfoil. A comprehensive study of the adaptive camber airfoil under quasi-steady conditions was performed by Lambie [57]. The analysis of the dynamic experimental results is therefore limited to the fluctuating part, mean values are omitted. Quasi-steady values that serve as a reference for the dynamic measurements and are shown in appendix B.

The presentation of the experimental results is divided into three parts: In section 4.4.1 the **dynamic motion response** of the adaptive camber airfoil is shown. When expressed in terms of the reduced frequency, the dynamic motion response corresponds to the transfer function of motion. The motion response is important for an interpretation of the adaptive camber airfoil's load alleviation capabilities. Better load manipulation is expected for high flap deflections that follow the perturbing angle of attack with a small phase shift.

In section 4.4.2 the **dynamic lift response** of the adaptive camber and the rigid airfoil is presented. When expressed in terms of reduced frequency, the dynamic lift response corresponds to the transfer function of the lift. For parameters satisfying the assumptions of thin airfoil theory, the experimental results are compared to theoretical transfer functions from literature that are introduced in section 3.2.

The **gust load reduction** potential of the adaptive camber airfoil is assessed in section 4.4.3. This is done by comparing the dynamic lift response of the adaptive and the rigid airfoil.

All results are presented following the order of the unsteady parameters presented in section 4.2. Generally, results for the **adaptive camber airfoil** are represented in red, the **rigid airfoil** in blue and the **load reduction factor** in green.

4.4.1. Dynamic Motion Response

In this section, the dynamic motion response of the adaptive camber airfoil is assessed using the magnitude of the transfer function of motion $|h_\gamma|$, which relates the fluctuating trailing flap angle γ to the perturbing gust angle of attack α_g. The experimental $|h_\gamma^*|$ is obtained from phase averaged data as explained in section 4.3.2 and compared to the theoretical motion response obtained with the description of Spiegelberg [88], see section 3.2.3. The theoretical h_γ depends on the reduced frequency $k = \frac{\pi f c}{U_\infty}$ and the reduced system stiffness $\kappa^+ = \frac{\kappa}{c^2 \frac{\rho}{2} U_\infty^2}$ and is independent of the gust amplitude $\widehat{\alpha}_g$ and the mean angle of attack $\widehat{\alpha}_g$. Best load manipulation is expected for high magnitudes $|h_\gamma|$ and small phase angles φ_γ. For phase angles $|\varphi_\gamma| \approx \pi$, the working principle of the adaptive camber airfoil is inverted and fluctuating loads are enhanced.

Influence of the Mean Angle of Attack α_m on the Motion Response

The influence of the mean angle of attack on the experimentally derived motion response is illustrated in Figure 4.7 using the measuring points of set ①. Values for the adaptive camber airfoil in configuration ⓐ are shown in Figure 4.7a, values for the adaptive camber airfoil and configuration ⓑ are shown in Figure 4.7b. The airfoils were tested over the entire range of mean angles of attack from $-10° \leq \alpha_m \leq 20°$ at two different inflow velocities $U_\infty = 10\,\text{m/s}$ and 15 m/s. According to theoretical considerations, the motion response is independent of the mean angle of attack α_m, which does not agree with the experimental findings: $|h_\gamma^*|$ depends heavily on α_m. The dependence is more pronounced for the less stiff configuration ⓐ. Highest values of $|h_\gamma^*|$ are found at high α_m, where the flow is presumed to separate from the airfoil. According to theory, $|h_\gamma|$ is higher for the less stiff configuration ⓐ and for higher inflow velocities U_∞. This behavior is recovered in the experimental data: $|h_\gamma^*|$ of the adaptive camber airfoil in configuration ⓐ is generally about twice as high for the stiffer configuration ⓑ. For higher U_∞, the higher aerodynamic moment around the leading-edge results in higher flap deflection and a higher value of $|h_\gamma^*|$.
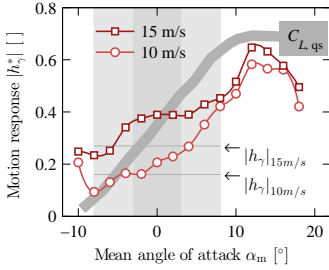
(a) Configuration (a)
$\kappa_\gamma = 2.88\,\text{Nm/rad}, M_\kappa = 0.28\,\text{Nm}$
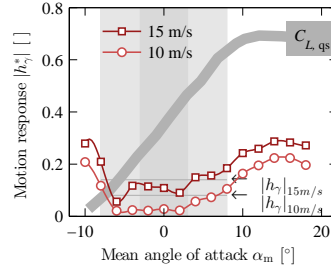
(b) Configuration (b)
$\kappa_\gamma = 5.76\,\text{Nm/rad}, M_\kappa = 0\,\text{Nm}$

Figure 4.7.: The motion response of the adaptive camber airfoil, quantified by the magnitude of the experimental transfer function of motion $\left|h_\gamma^*\right| = \widehat{\gamma}/\widehat{\alpha}_g$. The total angle of attack is $\alpha = \alpha_m + \widehat{\alpha}_g \sin(2\pi f t)$. The gust amplitude is held constant at $\widehat{\alpha}_g = 6.2\,°$, the gust frequency is set to $f = 5$ Hz. This leads to a trailing flap movement of $\gamma = \widehat{\gamma}\sin(2\pi f t + \varphi)$, from which the motion response h_γ^* is derived. Theoretical values of the motion response $\left|h_\gamma\right|$ for the respective inflow velocities and airfoil configurations are indicated as thin gray lines. The quasi-steady lift coefficient $C_{L,\text{qs}}$ is plotted in the background to provide an orientation of attached and detached flow regime in the steady case. The region of attached flow is highlighted with a light gray background. Linear assumptions are justified, if the total angle of attack $\alpha = \alpha_m \pm \widehat{\alpha}_g$ remains in the region of attached flow. This region between $-2\,° < \alpha_m < +2\,°$ is highlighted with a dark gray background.

Influence of the Gust Amplitude $\widehat{\alpha}_g$ on the Motion Response

The experimentally derived motion response for the parameters corresponding to set (2) is shown in Figure 4.8. The adaptive camber airfoil in configuration (a) is submitted to unsteady flow of variable gust amplitudes $\widehat{\alpha}_g$ at a constant gust frequency f and five different inflow velocities U_∞, yielding five different reduced system stiffnesses κ^+ and five different reduced frequencies k. Results for $\alpha_m = 2\,°$ are shown on the left, results for $\alpha_m = 8\,°$ are shown on the right. According to linear theory, the motion response $\left|h_\gamma\right|$ increases with increasing U_∞ (i.e. with decreasing κ^+ and decreasing k for one series of bars from left to right) and is independent of $\widehat{\alpha}_g$. The experimentally obtained values of $\left|h_\gamma^*\right|$ for $\alpha_m = 2\,°$ agree well with the theoretical values of $\left|h_\gamma\right|$. An increase of $\left|h_\gamma^*\right|$ with U_∞ for one distinct $\widehat{\alpha}_g$ is observed. The influence of $\widehat{\alpha}_g$ on the velocity dependence and the order of magnitude of $\left|h_\gamma^*\right|$ is small.
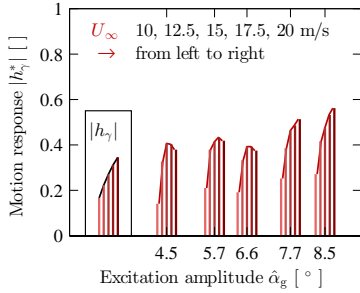
(a) $\alpha_{\mathrm{m}} = 2^{\circ}$
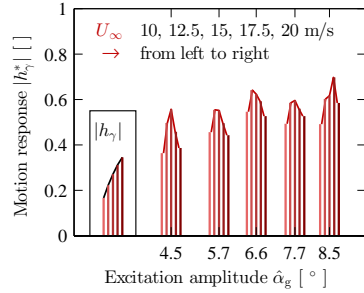
(b) $\alpha_{\mathrm{m}} = 8^{\circ}$

Figure 4.8.: The influence of the gust amplitude $\widehat{\alpha}_{\mathrm{g}}$ on the experimentally obtained motion response $|h_{\gamma}^{*}|$. The results are depicted as a series of bars and dispersed for better visibility around each investigated excitation amplitude $\widehat{\alpha}_{\mathrm{g}}$. The inflow velocity U_{∞} increases for one series of bars from left to right, the gust frequency is held constant at $f = 5\,\mathrm{Hz}$. The theoretical values of the transfer function of motion $|h_{\gamma}|$, obtained with the description of Spiegelberg, are depicted in a black box on the left side of each figure. As the underlying theory is linear, the values of $|h_{\gamma}|$ are identical for both α_{m} and independent of $\widehat{\alpha}_{\mathrm{g}}$.

At $\alpha_{\mathrm{m}} = 8^{\circ}$, the values of $|h_{\gamma}^{*}|$ are generally higher than for $\alpha_{\mathrm{m}} = 2^{\circ}$, which is in accordance with the results shown above. The theoretically predicted increase of $|h_{\gamma}^{*}|$ with increasing velocity U_{∞} is not seen: $|h_{\gamma}^{*}|$ takes a peak value at medium velocities and decreases again for higher velocities. This is not due to a mechanical resonance, as the excitation frequency f is held constant in this experimental data set. $\alpha_{\mathrm{m}} = 8^{\circ}$ is located close to the steady stall angle. Non-linear separation effects are highly sensitive to the reduced frequency and the Reynolds number, which both depend on U_{∞}. This sensitivity could be the reason for the difference of the velocity dependence of $|h_{\gamma}|$ and $|h_{\gamma}^{*}|$.

Influence of Excitation Frequency f on the Motion Response

The theoretical motion response of the adaptive camber airfoil $|h_{\gamma}|$ takes the structural and the aerodynamic properties of the system into account, as it is pointed out in section 3.2.3, p. 31. The structural properties of the adaptive camber airfoil (with only the flap's degree of freedom considered) resemble an ordinary spring-mass-damper system. These systems typically follow an excitation until their eigenfrequency with
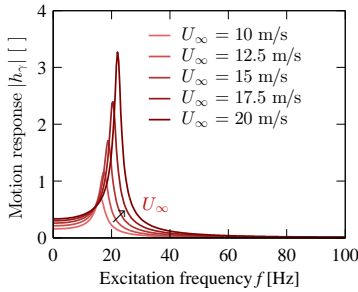
(a) Evolution of $|h_\gamma|$ over the entire frequency range.
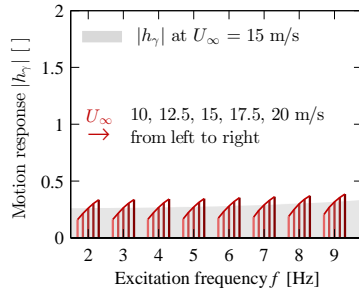
(b) Evolution of $|h_\gamma|$ over the parameter range investigated in the experiments.

Figure 4.9.: Magnitude of the theoretical transfer function of motion $|h_\gamma|$ for the adaptive camber airfoil in configuration Ⓐ, obtained with the results from Spiegelberg [88]. (a) graphically illustrates how higher aerodynamic damping shifts the resonance frequency for increasing inflow velocity to higher values. (b) shows that the influence of the inflow velocity for one distinct excitation frequency is more important than the influence of the excitation frequency at constant inflow velocity in the experimentally investigated parameter range. The representation is chosen to match the experimental results.
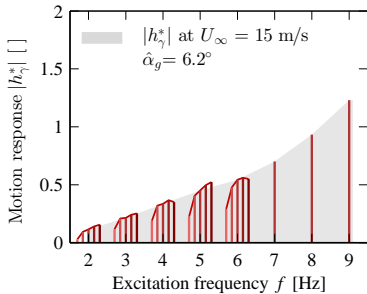
(a) Mean angle of attack $\alpha_m = 2°$
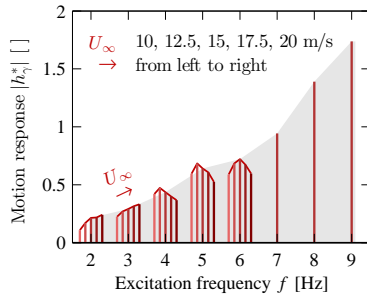
(b) Mean angle of attack $\alpha_m = 8°$

Figure 4.10.: The magnitude of the experimental transfer function of motion $|h_\gamma^*|$, obtained from parameter set ③, displayed as a set of bars around each integer-number excitation frequency. For one set of bars, U_∞ increases from $10\,\text{m/s} \leq U_\infty \leq 20\,\text{m/s}$ in steps of 2.5 m/s. The values for $U_\infty = 15\,\text{m/s}$ are depicted in gray to emphasize frequency dependent evolution at constant reduced system stiffness κ^+.

an increasing response magnitude. Around the resonance frequency, the system response experiences a step change in phase and the response magnitude takes a peak value. The resonance frequency is not only a function of the structural, but also of the aerodynamic properties of the system. For higher velocities, aerodynamic restoring forces become more important and the aerodynamically damped resonance frequency is shifted to higher frequencies. Figure 4.9a illustrates this behavior for different inflow velocities. When the aerodynamically damped resonance frequency is crossed, the phase of the motion response (not shown) changes by roughly π and reverses the working principle of the adaptive camber airfoil. A comprehensive representation of the dynamics of the system and the importance of the placement of the system eigenfrequencies in the excitation spectrum is given by Spiegelberg [88], p. 90). In the present study, only excitation frequencies below the flap's eigenfrequency are investigated. This is motivated by the desire to optimally exploit the adaptive camber airfoil's gust load alleviation capabilities and by the limitations of the maximal producible excitation frequency.

For the adaptive camber airfoil in configuration ⓐ, the calculated flaps eigenfrequency is located at $f_{res} = 13\,\text{Hz}$, without any damping being considered. This sets the value of the aerodynamically damped resonance frequency well beyond the maximal achievable excitation frequency of the active grid of $f_{max} = 9\,\text{Hz}$. In the investigated frequency region, the adaptive camber airfoil should suppress load fluctuations. $\left|h_\gamma^*\right|$ is supposed to increase with increasing excitation frequency. Figure 4.9b shows the magnitude of the theoretical transfer function $\left|h_\gamma\right|$ in the experimentally investigated parameter range, the representation is chosen to match the representation of the experimental results. Figure 4.10 shows the corresponding experimentally derived motion response $\left|h_\gamma^*\right|$ obtained with parameter set ③ over the excitation frequency f for $\alpha_m = 2°$ (left) and $\alpha_m = 8°$ (right). The general trend of the experimentally obtained motion response agrees with theory: $\left|h_\gamma^*\right|$ increases with increasing f when approaching the flaps aerodynamically damped resonance frequency. Quantitative discrepancies in the frequency dependence become obvious when comparing the experimental results of Figure 4.10 to the theoretical values in Figure 4.9. In Figure 4.9b, where the limiting values are set to match the limiting values of the experimentally derived data, the dependence of the $\left|h_\gamma\right|$ on f is insignificant compared to

the influence of U_∞. In the experimental data, the influence of f is more pronounced than the influence of U_∞. For $\alpha_m = 2°$, the value of $\left|h_\gamma^*\right|$ is generally smaller than for $\alpha_m = 8°$. This is in accordance with the results obtained above, where an increase of $\left|h_\gamma^*\right|$ with α_m was observed. When looking at a series of bars, the same trend as above is recovered; the dependence of $\left|h_\gamma^*\right|$ on U_∞, i. e. reduced stiffness, agrees with theoretical considerations for $\alpha_m = 2°$. At $\alpha_m = 8°$, the agreement is only observed for small gust frequencies f.

Dependence of the Motion Response on the Reduced Frequency k

For completeness and better comparison with the classical transfer functions for rigid airfoils, the motion response of the adaptive camber airfoil is presented as a function of the reduced frequency k. Figure 4.11 shows the magnitude $\left|h_\gamma^*\right|$ (left) and the phase φ_γ^* (right) of the transfer function of motion for $\alpha_m = 2°$ (a), $\alpha_m = 8°$(b) and $\alpha_m = 8°$(c). No major differences of the experimental values $\left|h_\gamma^*\right|$ and φ_γ^* are observed between $\alpha_m = 2°$ and $\alpha_m = 8°$. Even at the highest investigated mean angle of attack $\alpha_m = 14°$ the quantiative evolution of magnitude and phase of the motion response is similar to $\alpha_m = 2°$ and $\alpha_m = 8°$. The theoretical transfer function captures the trend of the experimental data for the magnitude $\left|h_\gamma^*\right|$ and the phase φ_γ^*. An increase of the magnitude $\left|h_\gamma^*\right|$ is observed with increasing reduced frequency k. The increase is stronger for higher U_∞, respectively smaller reduced system stiffnesses κ^+. As it is shown before, the dependence of the motion response on f is more pronounced in the experimental data than in theoretical predictions. This results in an over prediction of the experimental values for small k and an under prediction for high k. The influence of κ^+, visualized by the distance between the curves of constant U_∞, shows good agreement between experiments and theory. The phase of the motion response φ_γ^* decreases with increasing k. The influence of the inflow velocity U_∞ (and accordingly the reduced system stiffness κ) is negligible in the investigated range of k. Experimental values φ_γ^* and theoretical values φ_γ decrease at the same rate. A constant offset between experimental and theoretical values of about $(\varphi_\gamma^* - \varphi_\gamma) \approx 20°$ periods is observed. This offset might be due to the experimental and post-processing procedure as explained in section 4.3. Angle of attack fluctuations that serve as a phase reference are measured prior to the airfoil experiments in
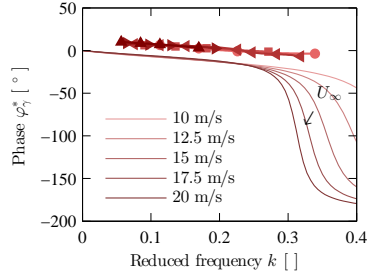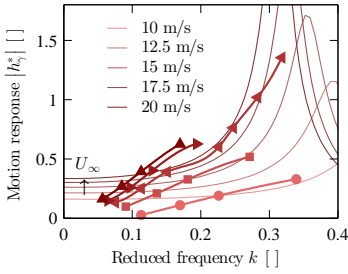
(a) Mean angle of attack $\alpha_\mathrm{m} = 2\,^\circ$
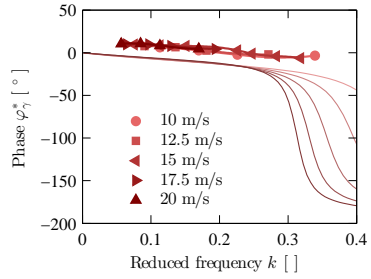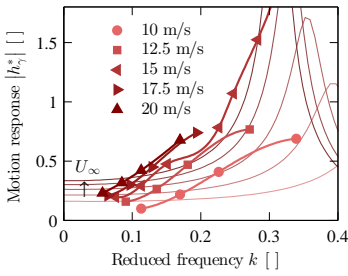
(b) Mean angle of attack $\alpha_\mathrm{m} = 8\,^\circ$
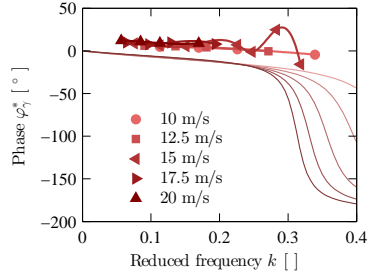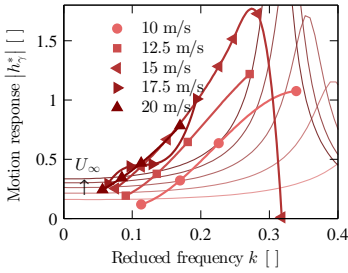
(c) Mean angle of attack $\alpha_\mathrm{m} = 14\,^\circ$

Figure 4.11.: The magnitude $\left| h_\gamma^* \right|$ (left) and phase φ_γ^* (right) of the aeroelastic transfer function as a function of the reduced frequency k for $\alpha_\mathrm{m} = 2\,^\circ$ (a), $\alpha_\mathrm{m} = 8\,^\circ$ (b) and $\alpha_\mathrm{m} = 14\,^\circ$ (c). Data points for constant U_∞ (and constant κ^+) are represented by the same marker symbols. The corresponding theoretical values are displayed as solid lines, color coded for the different investigated U_∞.

the empty wind tunnel. The phase is assigned by the light barrier signal of the active grids middle axis, which is collected during both measurements. An unintended displacement of the active grid's middle axis in-between both measurement campaigns could be the reason for the constant offset.

Conclusions

Qualitatively,

- the overall agreement between the theoretical motion response h_γ and the experimentally derived motion response h_γ^* is acceptable.

The magnitude $\left|h_\gamma^*\right|$ increases with increasing k and the phase φ_γ^* decreases with increasing k, as predicted by theory. The assumptions of linear theory, that the gust amplitude $\hat{\alpha}_g$ has a negligible influence on the magnitude $\left|h_\gamma\right|$, is verified. Under attached flow conditions at $\alpha_m = 2^\circ$, the dependence of the experimental $\left|h_\gamma^*\right|$ on U_∞ is captured by theory. This results in a correct representation of the reduced system stiffness κ^+. Experimental and theoretical $\left|h_\gamma\right|$ increase with increasing excitation frequency f, but the quantitative agreement is poor.

- The frequency dependence of the experimental $\left|h_\gamma^*\right|$ is significantly more pronounced than in the theoretical prediction.

The discrepancy increases with increasing k. It will be shown in the subsequent section that this is not caused by a faulty structural model, but due to a deviating prediction of the driving aerodynamic forces by linear theory.

Experimental and theoretical φ_γ decrease with increasing k at the same rate, but an offset is observed between experimental and theoretical values. This offset might be due to the procedure of phase assignment. Although not completely captured by the theoretical model, the

- experimental results of the motion response are promising regarding the adaptive camber airfoil's load alleviation capabilities.

Recall that higher gust load alleviation is expected for higher flap deflections and small phase angles between excitation and response. The highest motion response is

observed at high α_{m}, where the mean load is high and an effective damping of fluctuating loads is especially favorable. It is shown that the motion response $\left|h_{\gamma}^{*}\right| = \widehat{\gamma}/\widehat{\alpha}_{\mathrm{g}}$ is independent of the gust amplitude $\widehat{\alpha}_{\mathrm{g}}$. Higher gust amplitudes that would cause higher load fluctuations result in higher flap deflections and a more effective load manipulation. The amplitude of the motion response $\left|h_{\gamma}^{*}\right|$ increases with increasing k, i.e. with increasing unsteadiness of the flow. This is also favorable in terms of gust load alleviation as high frequency perturbations do not contribute to the wind turbine's energy output but are responsible for most of the fatigue loads. The phase φ_{γ} decreases steadily with increasing k. A rapid change in phase, which indicates the passage through the flaps aerodynamically damped eigenfrequency and a reversion of the adaptive camber airfoil's working principle was not provoked. The adaptive camber airfoil is thus expected to alleviate fluctuating loads at all investigated parameter combinations.

4.4.2. Dynamic Load Response

In this section, the dynamic load response of the rigid and the adaptive camber airfoil is assessed using the magnitude of the experimental transfer function of the load $\left|h_{L}\right|$. The transfer function of the load relates the dynamic lift response L_{dyn} of an airfoil in adaptive or rigid configuration to its respective quasi-steady value L_{qs}. The magnitude of the dynamic load response corresponds to the amplitude ratio of dynamic and steady lift response $\left|h_{L}\right| = \widehat{L}_{\mathrm{dyn}}/\widehat{L}_{\mathrm{qs}}$. The theoretical h_{L} is derived in section 3.2.3. For the adaptive camber airfoil, $h_{L,\mathrm{ad}}$ is calculated using the results of Spiegelberg [88]. For the rigid airfoil, Spiegelberg's solution $h_{L,\mathrm{rig}}$ is proportional to the Sears function S, the classical first-order transfer function of the sinusoidal gust problem. Experimental and theoretical transfer functions are relied by $h_{L,\mathrm{ad}}^{*} = h_{L,\mathrm{ad}}/2\pi$ and $h_{L,\mathrm{rig}}^{*} = h_{L,\mathrm{rig}}/2\pi = S$. In the representation of the results, the theoretical h is scaled with 2π such that the representation corresponds to the classical first-order transfer function. The theoretical $h_{L,\mathrm{rig}}$ depends on the reduced frequency k only, the theoretical $h_{L,\mathrm{ad}}$ depends additionally on the reduced system stiffness κ^{+}. The experimental values of h_{L}^{*} are obtained from dynamic and steady wind tunnel balance measurements, cf. section 4.3.1 and are additionally influenced by the mean angle of attack α_{m} and the gust amplitude $\widehat{\alpha}_{\mathrm{g}}$. The influence of these additional parameters is dis-

cussed first. Then, the experimental h_L^* is presented in terms of the reduced frequency and compared to the theoretical h_L for both the adaptive and the rigid airfoil. It will be shown that first-order theories do not capture the dynamic load response adequately. Therefore, a comparison to a higher order model is given at the end of this section.

Influence of the Mean Angle of Attack α_m on the Load Response

Figure 4.12 shows the magnitude of the transfer function of the load $|h_L|$ for the adaptive camber airfoil and the rigid airfoil as a function of the mean angle of attack α_m. The dynamic flow parameters correspond to set ①. On the left, values for the adaptive camber airfoil in configuration ⓐ are shown, the right side shows the same values for the adaptive camber airfoil in configuration ⓑ.
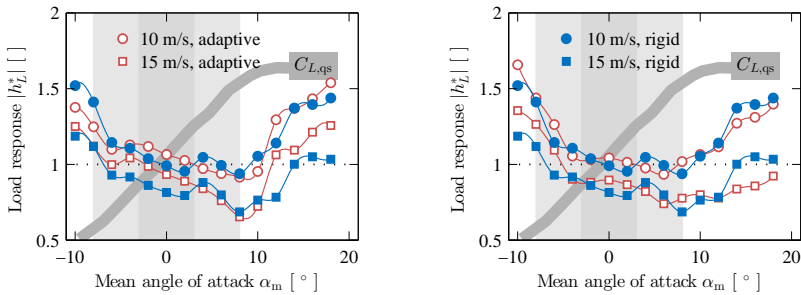
(a) Flexible airfoil in configuration ⓐ vs. rigid airfoil

(b) Flexible airfoil in configuration ⓑ vs. rigid airfoil

Figure 4.12.: Influence of the mean angle of attack α_m on the dynamic load response $|h_L^*|$. The gust amplitude is held constant at $\widehat{\alpha}_\mathrm{g} = 6.2\,°$, gust frequency is set to $f = 5\,\mathrm{Hz}$. Values of $|h_{L,\mathrm{ad}}^*|$ of the adaptive camber airfoil are indicated with open marker symbols, values of $|h_{L,\mathrm{rig}}^*|$ of the rigid airfoil are represented with filled marker symbols. Each inflow velocity U_∞ (indicated by the same marker symbol) results in one distinct reduced frequency k and reduced system stiffness κ^+, c.f. Table 4.1. The steady lift coefficient $C_{L,\mathrm{qs}}$ of the rigid Clark Y airfoil is plotted as a gray thick line in order to provide orientation of the flow regimes in the steady case. The area of attached flow under steady conditions is highlighted in light gray, mean angles of attack for which the total fluctuating angle of attack remains in the region of attached flow are highlighted in dark gray.

The general trend of the load response $|h_L^*|$ is similar for each parameter combina-

tion. In the region of moderate α_m, highlighted with a gray background, $\left|h_L^*\right|$ decreases with increasing α_m. Maximal values of $\left|h_L^*\right|$ are observed at very high and very low α_m, where the flow separates from the airfoil. In this region, the added angle of attack fluctuation provokes dynamic flow separation including the generation and interaction of large coherent vortices. This phenomenon, known as dynamic stall, typically provokes high force excursions. Recall that h_L relates the dynamic lift response of an airfoil to the quasi-steady lift of the same airfoil. h_L quantifies the differences between dynamic and steady lift response, but does not contain any information about the differences of the rigid and the adaptive camber airfoil. No significant differences between $\left|h_L^*\right|$ on the rigid and the adaptive camber airfoil in configuration ⓐ and configuration ⓑ are observed. This indicates that dynamic inflow has a similar influence on both the rigid and the adaptive camber airfoil.

Influence of the Gust Amplitude $\widehat{\alpha}_g$ on the Load Response

The influence of the gust amplitude on the load response is studied using the experimental data of parameter set ②. The results are presented in Figure 4.13, where the magnitude of the transfer function of motion $\left|h_L^*\right|$ is shown over the excitatory gust amplitude $\widehat{\alpha}_g$. The experimental results show that $\widehat{\alpha}_g$ has no influence on the order of magnitude of $\left|h_L^*\right|$, neither for the rigid, nor for the adaptive camber airfoil. Considering the influence of U_∞, by looking at a series of bars, reveals a qualitative discrepancy between theoretical prediction and experimental results. For the rigid airfoil, an increase in U_∞, i.e. decrease of k, leads to an increase of the dynamic load response. The inverse behavior is observed in the experimental data. In the case of the adaptive airfoil, the simultaneous decrease of k and κ^+ with increasing U_∞ leads to a decrease in the motion response $\left|h_\gamma^*\right|$. In the experimental $\left|h_\gamma^*\right|$, a decrease is observed for small $\widehat{\alpha}_g$, while for higher $\widehat{\alpha}_g$ an increase is observed. This change in behavior is due to the higher motion response $\left|h_\gamma^*\right|$ of the adaptive camber airfoil with increasing gust amplitudes, compare Figure 4.8, p. 71. An equivalent behavior is observed for $\alpha_m = 8°$ and $\alpha_m = 14°$ (not shown here) for the rigid airfoil. In the case of the adaptive camber airfoil, the change in velocity dependence (increase or decrease within one series of bars) is shifted to smaller $\widehat{\alpha}_g$, but the general trend stays similar. In all investigated cases, the order of magnitude of the experimental load re-

(a) Rigid airfoil **(b)** Adaptive camber airfoil
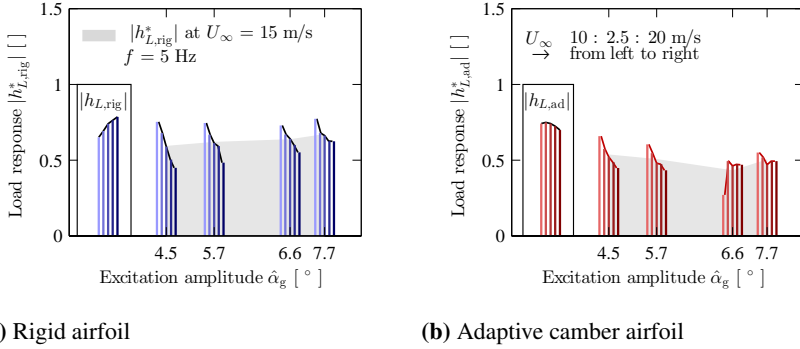
Figure 4.13.: Influence of the gust amplitude $\widehat{\alpha}_g$ on the load response $\left|h_L^*\right|$ for the rigid (a) and the adaptive camber airfoil (b). The mean angle of attack is set to $\alpha_m = 2\,°$ and the gust frequency is held constant at $f = 5\,\mathrm{Hz}$. U_∞ is varied from $10\,\mathrm{m/s} \leq U_\infty \leq 20\,\mathrm{m/s}$, leading to a decrease of k and κ^+ for one series of bars from left to right. The corresponding theoretical values $\left|h_L\right|$ are given for the rigid and the adaptive camber airfoil on the left of each figure.

sponse $\left|h_L^*\right|$ matches the theoretical values of $\left|h_L\right|$. The dependence on the reduced frequency k due to a change in U_∞ of the experimental $\left|h_L^*\right|$ and the theoretical $\left|h_L\right|$ does not agree.

Influence of the Excitation Frequency f on the Load Response

Figure 4.14 shows the evolution of the theoretical load response $\left|h_L\right|$ of the rigid (left) and the adaptive camber airfoil (right) over the excitation frequency f, color coded for different inflow velocities from $10\,\mathrm{m/s} \leq U_\infty \leq 20\,\mathrm{m/s}$. The load response of the rigid airfoil decreases steadily with increasing f from the quasi-steady value of $\left|h_{L,rig}\right| = 1$ at $f = 0\,\mathrm{Hz}$. The adaptive camber airfoil's load response $\left|h_{L,ad}\right|$ exhibits a resonance at the aerodynamically damped resonance frequency of the flaps f_{res}. For $f > f_{res}$, the behavior of $\left|h_{L,ad}\right|$ resembles $\left|h_{L,rig}\right|$. For $f < f_{res}$, which corresponds to the experimentally investigated frequency range, $\left|h_{L,ad}\right|$ decreases more rapidly than $\left|h_{L,rig}\right|$ and the velocity dependence is inverted. Figure 4.15 illustrates this behavior. The representation in Figure 4.15 is chosen to match the representation of the experimental results of Figure 4.16. For each integer number gust frequency f, $\left|h_L\right|$ is displayed as a series of bars, with U_∞ increasing from

(a) Rigid airfoil   **(b)** Adaptive camber airfoil
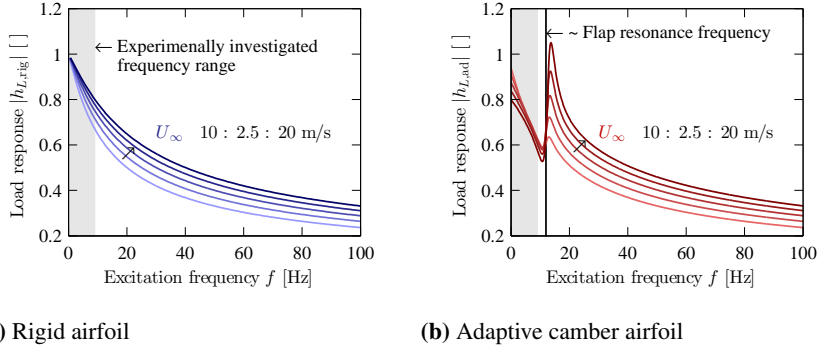
Figure 4.14.: The influence of the excitation frequency f on the theoretical transfer function of the load $|h_L|$ for the rigid and the adaptive camber airfoil. Parameters (chord length, flap length, reduced stiffness) correspond to the experimental setup. The range of experimentally investigated frequencies is indicated with a gray background. The adaptive camber airfoil exhibits a resonance at the aerodynamically damped eigenfrequency of the flaps. Below that frequency $|h_L|$ decreases with increasing f for both the rigid and the adaptive camber airfoil. At one distinct f, an increase of U_∞ provokes an increase of $|h_{rig}|$ and a decrease of $|h_{L,ad}|$.

left (10 m/s) to right (20 m/s). Both transfer functions $|h_{L,rig}|$ and $|h_{L,ad}|$ depend on the reduced frequency $k = \pi f c / U_\infty$. In the case of the rigid airfoil, $|h_{L,rig}|$ is a function of k only. The load response of the adaptive camber airfoil $|h_{L,ad}|$ possesses an additional dependence on the reduced system stiffness $\kappa^+ \propto 1/U_\infty^2$. Figure 4.15 allows to separate the influence of f and U_∞ on $|h_{L,rig}(k)| = |h_{L,rig}(\pi f c / U_\infty)|$ and $|h_{L,ad}(k, \kappa^+)| = |h_{L,ad}(\pi f c / U_\infty, 1/U_\infty^2)|$. The load response of both airfoils decreases with increasing f, the decrease is more pronounced for $|h_{L,ad}|$ than for $|h_{L,rig}|$. As it was shown above, decreasing k by increasing U_∞ leads to a decrease of $|h_{L,rig}|$ for one series of bars. $|h_{L,ad}|$ increases for the same parameters, due to the additional decrease of κ^+.

The experimental load response $|h_L^*|$, displayed in Figure 4.16, differs from the theoretical $|h_L|$ in both frequency and velocity dependence. For both the rigid (left) and the adaptive camber airfoil (right), the experimental $|h_L^*|$ increases with increasing excitation frequency. It was shown in section 4.4.1, p. 71 that the experimental
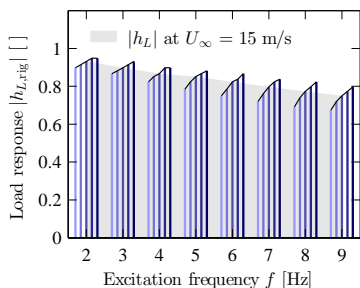
(a) Rigid airfoil
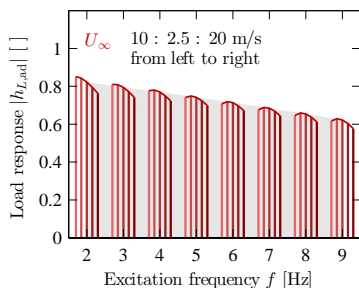
(b) Adaptive camber airfoil

Figure 4.15.: The theoretical load response $|h_L|$ for the rigid (a) and the adaptive camber airfoil (b), displayed over the excitation frequency f. The representation matches the representation of the experimental results for better comparison. $|h_L|$ is displayed as a series of bars for each integer number excitation frequency. The inflow velocity U_∞ increases from left to right for each series of bars, resulting in a decrease of the reduced frequency k and reduced stiffness κ^+. Values for $|h_L|$ at $U_\infty = 15\,\mathrm{m/s}$ are emphasized with a gray background to highlight the frequency dependence at constant κ^+.
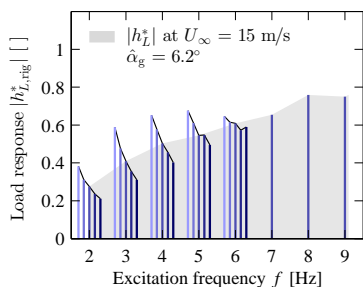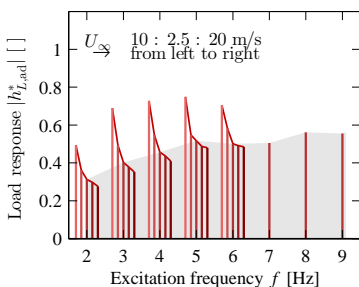
(a) Rigid airfoil

(b) Adaptive camber airfoil

Figure 4.16.: The experimental load response $|h_L^*|$ for the rigid (a) and the adaptive camber airfoil (b), displayed over the excitation frequency f. The gust amplitude is set to $\hat{\alpha}_g = 6.2°$, the mean angle of attack is set to $\alpha_m = 2°$. The velocity is varied from $10\,\mathrm{m/s} < U_\infty < 20\,\mathrm{m/s}$ in steps of 2.5 m/s. This modifies the reduced frequency k and in the case of the adaptive camber airfoil additionally the reduced system stiffness κ^+. The corresponding theoretical values are displayed in Figure 4.15.

motion response $\left|h_\gamma^*\right|$ increases stronger with the excitation frequency f than the theoretical $\left|h_\gamma\right|$. This behavior can now be explained. The driving aerodynamic moment around the leading-edge is proportional to the total load on the airfoil. The poor prediction of the frequency dependence of the load response leads to an equally poor prediction of the driving aerodynamic moment. This causes the difference between experimentally observed and theoretical motion response.

At all investigated excitation frequencies, $\left|h_L^*\right|$ decreases for one series of bars. This is not in agreement with theoretical values. A similar behavior is observed for $\alpha_m = 8°$.

Dependence of the Load Response on the Reduced Frequency k

Combining the influence of the inflow velocity U_∞ and the excitation frequency f leads to the classical representation in terms of the reduced frequency k. Figure 4.17 shows the transfer function of the load for the rigid airfoil $\left|h_{L,\mathrm{rig}}\right|$ and the adaptive camber airfoil $\left|h_{L,\mathrm{ad}}\right|$ as a function of k. In Figure 4.17a, the mean angle of attack is set to $\alpha_m = 2°$, in Figure 4.17b to $\alpha_m = 8°$ and in Figure 4.17c to $\alpha_m = 14°$. The corresponding phases φ_L^* are shown in Figure 4.18.

It is shown above that the theoretical load response $\left|h_L\right|$ fails to capture the influence of the reduced frequency, regardless whether U_∞ or f are varied. When displayed in terms of reduced frequency, the fundamental difference between theoretical and experimental load response becomes even clearer. While theory predicts an decrease of $\left|h_L\right|$ with increasing k, the experimental values show an opposite behavior. $\left|h_L^*\right|$ increases for both the rigid and the adaptive camber airfoil with increasing k. A similar discrepancy is observed for the phase of the load response φ_{h_L}. While the discrepancy between experimental and theoretical values in terms of amplitude and phase is significant, the experimental values show a very similar behavior for all investigated α_m. For $\alpha_m = 2°$ magnitude and phase almost fall in line when displayed over k. With increasing α_m, the absolute value of the magnitude increases and values for the phase scatter wider. The global behavior however stays similar.

A systematic measurement error, for example due to the eigenfrequency of the force balance, can be excluded. The pressure difference at the leading-edge, which is proportional to the total lift, exhibits the same behavior as the load response in terms of

(a) $\alpha_{\mathrm{m}} = 2°$

(b) $\alpha_{\mathrm{m}} = 8°$

(c) $\alpha_{\mathrm{m}} = 14°$
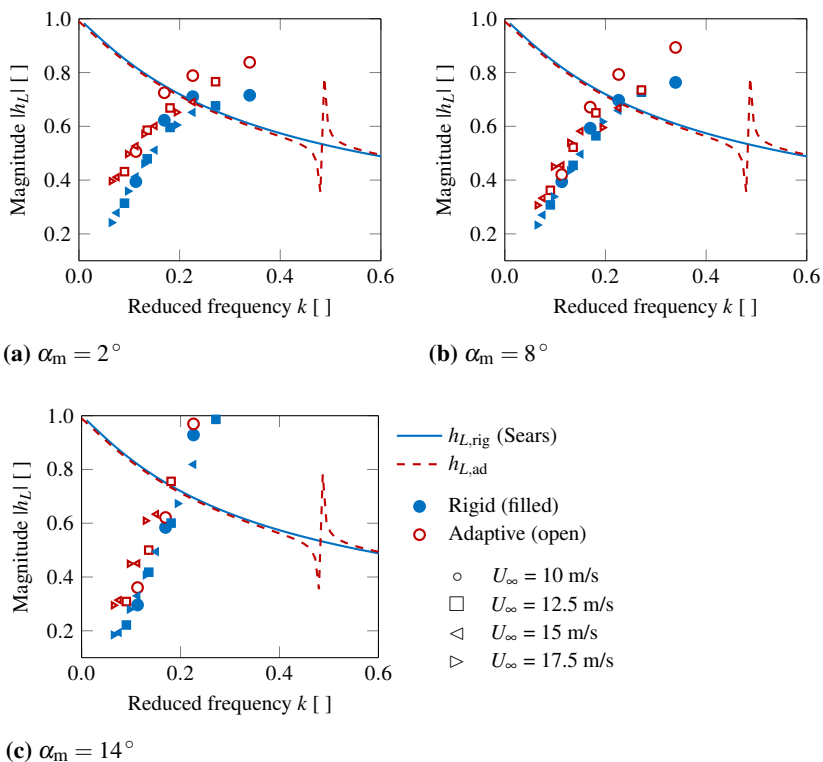
Figure 4.17.: Magnitude of the load response $\left| h_L \right|$ of as a function of the reduced frequency k at $\alpha_{\mathrm{m}} = 2°$ (a), $\alpha_{\mathrm{m}} = 8°$ (b) and $\alpha_{\mathrm{m}} = 14°$ (c). Experimental values of the rigid airfoil are represented by filled marker symbols, values for the adaptive camber airfoil are represented with open marker symbols. Equal marker symbols stand for equal inflow velocities, i.e. constant reduced system stiffness of the adaptive camber airfoil. The gust amplitude is set to $\widehat{\alpha}_{\mathrm{g}} = 6.2°$. The theoretical first-order transfer functions $h_{L\mathrm{rig}}$ corresponds to the Sears function, $h_{L\mathrm{ad}}$ is obtained from the results of Spiegelberg [88]. $h_{L\mathrm{ad}}$ depends on κ^+ and thus on U_∞. For clarity, only $h_{L\mathrm{ad}}$ at $U_\infty = 15\,\mathrm{m/s}$ is shown.

magnitude and phase. Comparison with other authors is difficult, as very few experimental data exists. Hatanaka and Tanaka [33] observed a similar behavior for the magnitude of the aeroelastic response of a bridge deck.

The theoretical load response is derived using the assumptions of thin airfoil theory. The Clark Y airfoil fulfills the assumptions usually requested when applying thin air-
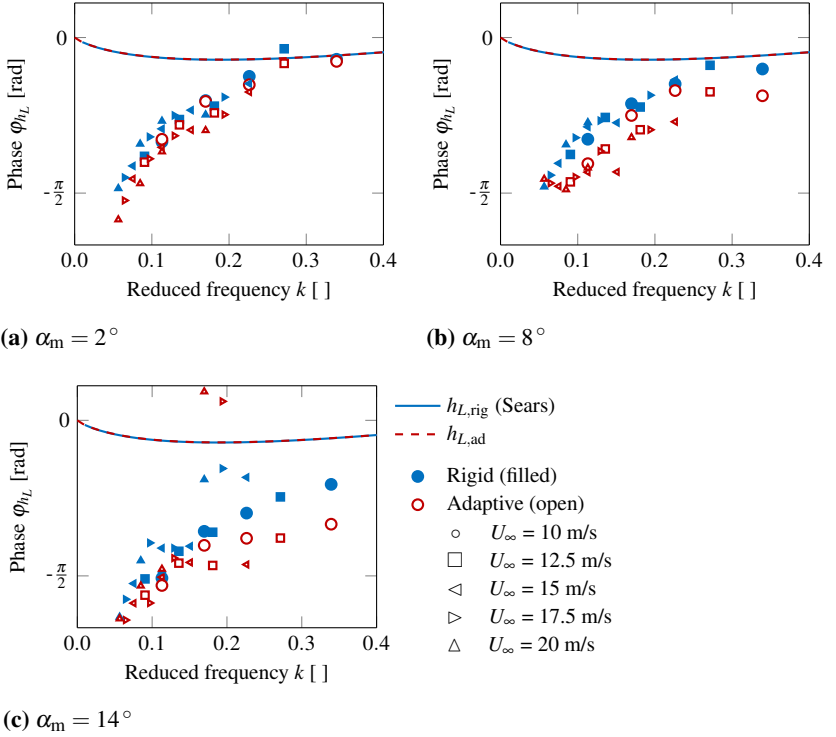
Figure 4.18.: Phase of the load response φ_{h_L} of as a function of the reduced frequency k for $\alpha_m = 2°$ (a), $\alpha_m = 8°$ (b) and $\alpha_m = 14°$ (c). Experimental values of the rigid airfoil are represented by filled marker symbols, values for the adaptive camber airfoil are represented with open marker symbols. Equal marker symbols stand for equal inflow velocities, i.e. constant reduced system stiffness of the adaptive camber airfoil. The gust amplitude is set to $\hat{\alpha}_g = 6.2°$.

foil theory (thin airfoil of 11 % thickness, small camber of 1.7 %, small mean angle of attack of $\alpha_m = 2°$). Still, the Clark Y airfoil possesses a thickness, camber and mean angle of attack and the question arises, whether the discrepancy of theoretical and experimental load response is caused by one of these simplifications. One possibility to take the airfoil's thickness, camber and mean angle of attack into account is the application of a panel code. Similar to thin airfoil theory, panel methods build on potential flow assumptions and fullfill zero penetration boundary conditions

at the airfoil's surface. In contrast to thin airfoil transfer functions, which provide closed form solutions for small harmonic perturbatioins in frequency domain, panel methods can be coupled with random perturbations in time domain. Spiegelberg [88] provides a panel method for the rigid and the adaptive camber airfoil, which is used to simulate the experimental setup. The geometry of the airfoil resembles the Clark Y airfoil at $\alpha_m = 2°$ and the inflow conditions are chosen to match the measured unsteady inflow in the active grid wind tunnel. The resulting calculated load response differs only slightly from the theoretical load response $|h_L|$ obtained by thin airfoil theory, as reported by Jäger [40]. This indicates that none of the simplifications that distinguish thin airfoil theory from panel methods is responsible for the deviating representation of the experimental results.

Figure 4.17 and Figure 4.18 show that the experimentally derived values for $|h_L^*|$ and φ_L^* fall in line for small α_m when displayed over the reduced frequency k. This suggests that k is the correct parameter to describe the problem. The difference between experimental and theoretical quasi-steady values of $|h_L|_{k \to 0}$ indicate a faulty scaling of the problem. The theoretical $|h_L|$ approaches a quasi-steady value of $|h_L| = 1$ at $k = 0$. In the experimental setup, the smallest realizable reduced frequency is $k = 0.05$. At $k = 0.05$, the experimental value is $|h_L^*| \approx 0.2$ with a decreasing trend for $k \to 0$. The lift response h_L is obtained by relating the dynamic to the quasi-steady lift. The quasi-steady lift is approximated by $L_{qs} = (\partial L / \partial \alpha) \widehat{\alpha}_g$. In agreement with the assumptions of thin airfoil theory, that the presence of an airfoil does not alter the surrounding velocity field, the gust amplitude $\widehat{\alpha}_g$ is measured prior to the airfoil experiments in the empty wind tunnel. Obviously, this assumption is violated and the airfoil 'sees' a different gust amplitude than the gust amplitude $\widehat{\alpha}_g$ of the undisturbed flow field. One approach that takes the interaction of a perturbed surrounding flow and the oncoming gust into account are second-order models. A second-order transfer function of an airfoil entering a sinusoidal vertical gust is given by Goldstein and Atassi [29], cf. section 3.2.4, p. 34. The main difference to first-order transfer functions is the back-coupling of a spatially variable steady velocity field on the unsteady perturbation. The result of Atassis model [4], tuned with the parameters of the experimental setup are given in Figure 4.19. The model is applicable for rigid airfoils only. Accordingly, only the experimental load response of the rigid airfoil $|h_{L,rig}^*|$ is plotted. Figure 4.19a shows the magnitude $|h_L|$ and Figure 4.19b shows the phase of
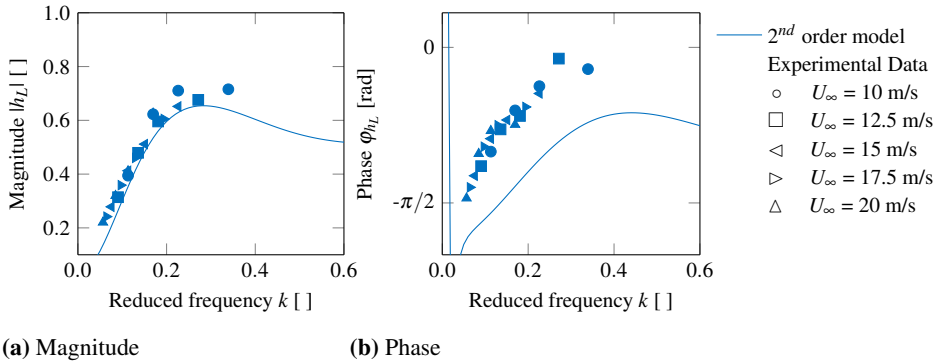
(a) Magnitude   **(b)** Phase

Figure 4.19.: Comparison of the rigid airfoil's experimental load response h_L^* to a second-order model of Goldstein and Attassi [29]. (a) Magnitude $|h_L|$ and (b) Phase φ_{h_L}. The airfoil has a mean angle of attack of $\alpha_m = 2°$ and is submitted to vertical sinusoidal gusts of amplitude $\widehat{\alpha}_g = 6.2°$ and variable reduced frequency k.

the load response.

Other than the load response obtained by transfer functions of first-order, second-order theory captures the experimental data remarkably well; experimental and theoretical values of the magnitude almost collapse. For the phase, an offset of $\varphi h_L - \varphi h_L^*$ is observed. The same offset is observed for the phase of the motion response, cf. Figure 4.11, p. 75, suggesting a systematic error during phase assignment. The magnitudes of experimental and theoretical values approach the same limit for $k \to 0$, which indicates a correct scaling of the problem. At the higher mean angle of attack of $\alpha_m = 8°$, similar agreement between experimental and theoretical values is observed.

Conclusions

The first conclusion of this section is that

- first-order transfer functions of the lift response do not reproduce the dependence on the reduced frequency k correctly.

Linear theory predicts a decrease of the dynamic lift amplitude. In experimental data, an increase of dynamic lift amplitude with increasing k is observed, regardless

whether U_∞ or f are changed to manipulate k. The only parameter obviously violating the assumptions of first-order transfer functions is the gust amplitude which is set to the relatively high value of $\widehat{\alpha}_g = 6.2°$. It was shown with parameter set ② that the gust amplitude has no influence on the experimental transfer functions. Other parameters, usually in agreement with thin airfoil theory (airfoil thickness, camber and mean angle of attack) were taken into account by means of a panel code, but did not alter the diverging frequency dependence. First-order transfer functions are commonly used in industry, especially in flutter calculations. The divergent prognosis of the airfoil response in terms of frequency is an important result that should be kept in mind. Despite the fundamental discrepancy between first-order transfer functions and experimental results, some basic information can be retained, which provide a good basis for further investigations:

- The reduced frequency k is an appropriate parameter to scale the problem.

- The amplitude of the perturbation has no significant influence.

- The mean angle of attack changes the absolute value of the transfer function, but has little influence on the dependence on other parameters.

One promising approach for an adequate theoretical transfer function is the second-order closed form solution proposed by Goldstein and Atassi, which shows good agreement with experimental results. If a transfer function (experimentally or analytically) is found, it provides information over a wide range of parameters. Even at higher mean angles of attack of $\alpha_m = 8°$ and $\alpha_m = 14°$ and high gust amplitudes, where the flow around the airfoil is supposed to separate and the physical mechanisms of lift generation change, it follows the same behavior as in the attached flow regime.

4.4.3. Load Reduction

In this section, the **load reduction** capabilities of the adaptive camber airfoil are evaluated. As a quantitative measure, the load reduction factor LR, cf. section 4.3.3, p.67, is used. A theoretical value for LR can be derived from the dynamic load response $|h_L|$ and steady calculations. As seen above, theoretical first-order models fail to reproduce the frequency dependence of the load response correctly. No second-order

model exists for the adaptive camber airfoil. Therefore, no comparison to theoretical values is drawn and the analysis is limited on the experimental data only. It was shown in the preceding sections that the experimental motion response $|h_\gamma^*|$ and the load response $|h_L^*|$ depend on several parameters (mean angle of attack α_m, gust frequency f, gust amplitude $\widehat{\alpha}_g$). Consequently, the load reduction capabilities of the adaptive camber airfoil also depend on these parameters. This dependence is shown first. Then, the adaptive camber airfoil's load reduction capabilities are assessed as a function of the reduced frequency.

Influence of the Mean Angle of Attack α_m on the Load Reduction

Figure 4.20 shows the load reduction factor *LR* for the adaptive camber airfoil in configuration ⓐ (left) and configuration ⓑ (right) over the mean angle of attack α_m, using the experimental data of parameter set ①. Recall that $LR = 1$ equals complete attenuation of fluctuating loads by the adaptive camber mechanism, while $LR = 0$ stands for equally fluctuating loads on both the adaptive and the rigid airfoil. *LR* remains positive in all cases, indicating a reduction in gust loads by the adaptive camber mechanism for all investigated parameters.
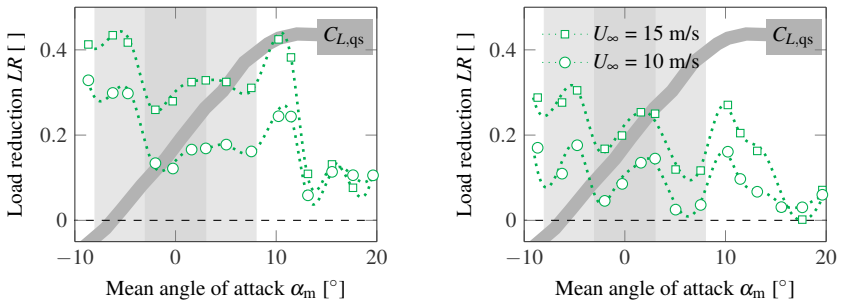
(a) Configuration ⓐ $: k_\gamma = 2.88\,\mathrm{Nm/rad}$
$f = 5\,\mathrm{Hz},\ \widehat{\alpha}_g = 6.2\,^\circ$

(b) Configuration ⓑ $: k_\gamma = 5.76\,\mathrm{Nm/rad}$
$f = 5\,\mathrm{Hz},\ \widehat{\alpha}_g = 6.2\,^\circ$

Figure 4.20.: The load reduction of the adaptive camber airfoil in configuration ⓐ (left) and configuration ⓑ (right) depends largely on the reduced system stiffness κ^+ and the mean angle of attack α_m. Higher load reduction is achieved for lower κ^+, i.e. lower physical stiffness of the resorting spring system κ_γ and higher inflow velocities U_∞.

LR depends largely on the reduced system stiffness $\kappa^+ = 2\kappa/\rho c^2 U_\infty^2$ of the adaptive camber airfoil. Lower reduced system stiffness results in a higher quasi-steady rate of de-cambering $\partial\gamma/\partial\alpha$ (cf. section C.1, p. 175) and a higher dynamic motion response $|h_\gamma|$ (cf. section 4.4.1, p. 69). Accordingly, a more effective manipulation of fluctuating loads is observed for higher U_∞ and the less stiff configuration (a). For configuration (a), κ^+ was chosen such that the airfoil de-cambers completely over the angle of attack range from $-10° \leq \alpha_m \leq 20°$ under quasi-steady conditions, cf. appendix C.1, Figure C.1, p. 176. Smaller κ^+ and accordingly higher *LR* are possible, but are limited by the aerodynamically damped resonance of the flaps degree of freedom, which should be chosen well above the expected excitation frequency. *LR* depends significantly on the mean angle of attack α_m. A maximum in gust load attenuation is obtained at $\alpha_m = 10°$ for both configurations of the adaptive camber airfoil. This is the steady stall angle of the rigid airfoil. Under dynamic inflow conditions, the fluctuating angle of attack passes the static stall angle and provokes dynamic stall and high lift excursions on the rigid airfoil. The adaptive camber mechanism effectively damps these load fluctuations and *LR* takes a peak value. A similarly high load reduction is also observed at $\alpha_m \leq -6°$. The dynamic load response $|h_L|$ shown in section 4.4.1, Figure 4.7, p. 70 exhibits peak values in the same region of angle of attack. This indicates the presence of nonlinear dynamic effects not only for very high, but also very small α_m. These non-linear effects seem to have less influence on the adaptive camber airfoil. In configuration (b), a third maximum in load attenuation at $\alpha_m = 2°$. This is the angle of attack at which the adaptive camber airfoil forms the original Clark Y profile ($\gamma = 0°$) under quasi-steady conditions.

Influence of the Gust Amplitude $\widehat{\alpha}_g$ on the Load Reduction

The influence of the gust amplitude $\widehat{\alpha}_g$, obtained from the experimental data of the parameter set (2), is shown in Figure 4.21. Values for $\alpha_m = 2°$ are shown on the left, values for $\alpha_m = 8°$ are shown on the right. As for the experimental motion response $|h_\gamma^*|$ and the experimental load response $|h_L^*|$, the influence of the gust amplitude $\widehat{\alpha}_g$ plays a minor role on the load reduction capabilities of the system. A slight increase of the *LR* with $\widehat{\alpha}_g$ is observed for the case of $\alpha_m = 2°$, which is also observed for the motion response, cf. Figure 4.8, p. 71. *LR* is a relative measure that compares the

(a) $\alpha_{\mathrm{m}} = 2°$ **(b)** $\alpha_{\mathrm{m}} = 8°$
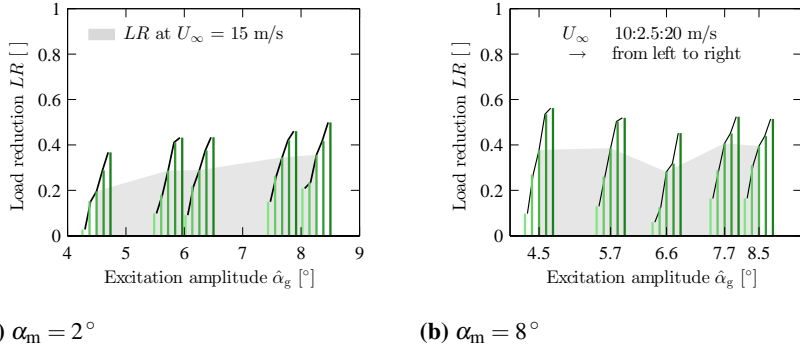
Figure 4.21.: The influence of the gust amplitude $\widehat{\alpha}_{\mathrm{g}}$ on the load reduction. Values of *LR* for the indicated $\widehat{\alpha}_{\mathrm{g}}$ are displayed as a series of bars, dispersed for better visibility. For one series of bars, U_{∞} increases from left to right, leading to a decrease of k and κ^{+} from left to right. The excitation frequency is constant at $f = 5\,\mathrm{Hz}$.

load fluctuations on the adaptive camber airfoil to the load fluctuations on the rigid airfoil under identic unsteady conditions. An independence of *LR* and $\widehat{\alpha}_{\mathrm{g}}$ results in higher absolute reduction of fluctuating loads of high amplitude. This is beneficial for the alleviation of rarely occurring destructive peak loads.

When comparing one series of bars at a certain $\widehat{\alpha}_{\mathrm{g}}$, *LR* increases with U_{∞}, respectively with decreasing k and κ^{+}. An equivalent trend was observed for the motion response of the adaptive camber airfoil at $\alpha_{\mathrm{m}} = 2°$, confirming the existence of a correlation between motion response and load reduction in the attached flow regime. When thinking about gust load alleviation on wind turbines, this is a very favorable result; high velocities, i.e. high dynamic pressures, provoke high load fluctuations at high mean values. These harmful events are more effectively damped by the adaptive camber airfoil than the less harmful fluctuations at low dynamic pressures, where the mean values and the amplitudes of the load fluctuations are small.

Influence of the Excitation Frequency f on the Load Reduction

Figure 4.22 shows the dependence of the gust load reduction *LR* on the gust frequency f, derived from the experimental data of parameter set ③. Values for $\alpha_{\mathrm{m}} = 2°$ are shown on the left, values for $\alpha_{\mathrm{m}} = 8°$ are shown on the right. An increase of *LR*
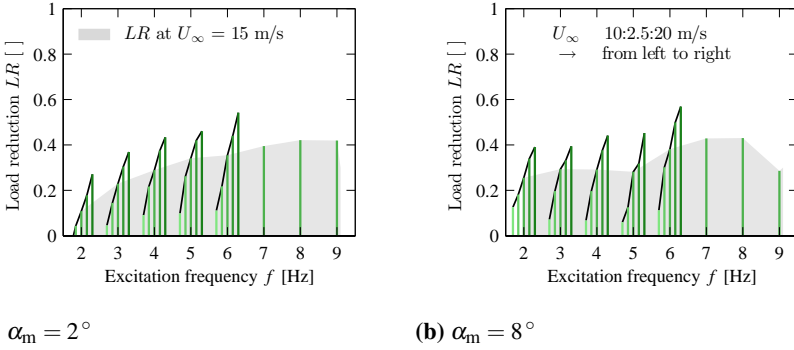
Figure 4.22.: Load reduction LR as a function of the excitation frequency f. The gust amplitude is constant at $\widehat{\alpha}_g = 6.2°$. For each integer number excitation frequency, values of LR obtained at different U_∞ are displayed as series of bars. The values of LR at $U_\infty = 15\,\text{m/s}$ are provided with a gray background in order to emphasize the frequency dependence at one distinct U_∞, i.e. reduced system stiffness κ^+.

with the excitation frequency f is observed for both mean angles of attack. This can be explained by looking at the motion response of the adaptive camber airfoil, cf. Figure 4.10. The motion response increases with increasing frequency due mechanical resonance and due to the increasing driving aerodynamic moments: The aerodynamic moments scale with the total lift. The dynamic lift response, shown in Figure 4.16, p. 82 increases also with increasing f.

Dependence of the Load Reduction on the Reduced Frequency k

Figure 4.23 shows the load reduction factor LR over the reduced frequency k, obtained from the experimental data of parameter set ③ at at $\alpha_m = 2°$ (a), $\alpha_m = 8°$ (b) and $\alpha_m = 14°$ (c). A distinct relation between k, κ^+ and LR is observed for $\alpha_m = 2°$ and $\alpha_m = 8°$. Generally, LR is higher for higher U_∞, i.e. smaller κ^+ and increases with k. For $\alpha_m = 2°$, a steady increase of LR with k is observed for all U_∞. For $\alpha_m = 8°$, an increase of LR with k is only observed for $U_\infty > 10\,\text{m/s}$. The increase is small for small k and becomes more pronounced for higher k. In the case of $U_\infty = 15\,\text{m/s}$, where additional measurements are performed at higher excitation frequencies, LR decreases again after its maximum is reached. This behavior is not

(a) $\alpha_m = 2°$

(b) $\alpha_m = 8°$

(c) $\alpha_m = 14°$
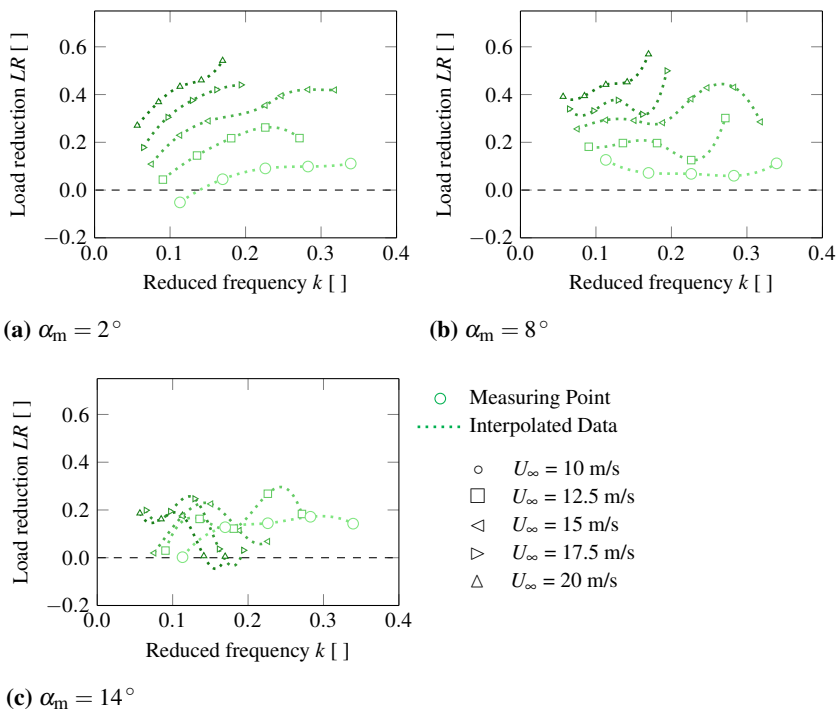
Figure 4.23.: The load reduction LR as a function of the reduced frequency k at $\alpha_m = 2°$ (a), $\alpha_m = 8°$ (b) and $\alpha_m = 14°$ (c). Values obtained at one U_∞ (i.e. constant reduced system stiffness) are represented by the same marker symbols. For one U_∞, f is varied by changing the excitation frequency f. The gust amplitude is held constant at $\widehat{\alpha}_g = 6.2°$.

seen in the motion response. The load reduction factor stays positive in all investigated cases, except for one parameter combination ($\alpha_m = 2°$, $U_\infty = 10\,\text{m/s}$), where the driving aerodynamic moment was not sufficient to efficiently operate the adaptive camber mechanism. For $\alpha_m = 14°$ the load reduction stays between 0 and 0.3, but no distinct dependence on k or κ^+ is observable. It should be noted that even in the detached flow regime, no increase of the load fluctuation due to the adaptive camber mechanism is observed.

Conclusions

The performance of the adaptive camber airfoil in terms of gust load alleviation is extremely promising:

- The adaptive camber mechanism effectively reduces fluctuating loads over the entire investigated parameter range.

Even in the detached flow regime at very high α_m, no augmentation of fluctuating loads is observed. Values of up to $LR = 0.6$ are obtained, meaning that

- The adaptive camber mechanism alleviates up to 60 % of the fluctuating loads.

This is comparable with active systems (van Dam et al. [95]). Due to the passive nature of the adaptive camber mechanism,

- The adaptive camber airfoil is most effective at parameter combinations provoking harmful load fluctuations, i.e. high U_∞ and high α_m.

High inflow velocities result in higher mean and fluctuating loads that contribute more to fatigue than fluctuations at smaller inflow velocities. High inflow velocities also entail higher aerodynamic moments that actuate the adaptive camber mechanism more effectively, leading to higher flap deflections and a higher manipulation of fluctuating loads. Like high inflow velocities, high mean angles of attack result in higher mean loads. Peak values of LR are observed at α_m close to the static stall angle, where dynamic stall typically provokes high force excursions. The experimental results indicate that the adaptive camber airfoil effectively reduces the effect of dynamic stall.
LR compares the mean adjusted values of the lift fluctuation and gives no information about mean values. It should be kept in mind that for a pre-cambered configuration,

- The adaptive camber airfoil generates significantly higher mean loads at non-critical conditions, i.e. small U_∞ and small α_m.

In this section, no comparison between theoretical values and experimental data is drawn, due to the differences between the experimental load response $\left| h_L^* \right|$ and the corresponding theoretical predictions, cf. section 4.4.2, p. 77. It is found that

- *LR* scales with the experimental motion response $\left|h_\gamma^*\right|$

for $\alpha_\mathrm{m} = 2\,^\circ$, where the fluctuating angle of attack remains completely beyond the static stall angle. In this region, *LR* can be predicted by a theoretical model as the one from Spiegelberg [88], if a correct representation of the dynamic load response is found.

5. Sinusoidally Oscillating Airfoil Experiment

This chapter is concerned with the second wind tunnel experiment performed in the scope of this thesis, a sinusoidally oscillating airfoil in pure pitch and pure plunge motion in a constant air stream. The experimental approach is schematically visualized in Figure 5.1.

Objectives		
3D flow situation blade bend and twist	attached	detached
2D flow situation airfoil oscillation	**individual dyn. response** — Verification of Theodorsen function on pitching airfoil, limits of applicability	Investigation of physical mechanisms responsible for gust load alleviation in detached flow.
Exp. setup pitch-plunge rig	**load reduction** — Influence of mass inertia on flap system during blade bending, approximated by pure plunge motion	

Figure 5.1.: Schematic overview of the pursued experimental approach.

Pitch and plunge motion of a two-dimensional airfoil corresponds to the twisting and bending oscillations of a wind turbine blade. During normal operation, these oscillations occur due to the cyclic loading resulting from the passage of the blade through the atmospheric boundary-layer or tower shadow. The cyclic loading contributes to fatigue life and a diminution of the fluctuation amplitudes is desirable. It is shown in Chapter 4 that the adaptive camber mechanism effectively reduces these fluctuating loads, which in turn will lead to smaller blade oscillations during normal operation. Bending oscillations also occur at off normal operation, for example after the impact of a strong gust or due to an emergency stop. On an oscillating airfoil with adaptive camber mechanism, the inertial forces of the flap system contribute to the total sys-

tem behavior and could either enhance or counteract the driving aerodynamic forces. The first objective of this experimental investigation is to

- study the influence of mass inertia on the adaptive camber airfoil's aeroelastic response.

This is done for a pure plunging motion, which approximates blade bending. It is shown in Chapter 4 that the first-order transfer function of a sinusoidal vertical gust encounter, the Sears function, does not agree with experimental results. A two-dimensional airfoil in pure pitching or plunging oscillation corresponds to the Theodorsen problem. The experimental setup offers the possibility to experimentally

- verify first-order transfer functions and investigate their limits of applicability.

This is done for a purely pitching rigid airfoil. In the attached flow regime, the adaptive camber mechanism is primarily pressure driven and its functionality is well understood. At high angles of attack, viscous forces become predominant. It is shown in Chapter 4 that the adaptive camber airfoil alleviates gust loads even above the static stall angle, but no distinct relationship between gust amplitude, reduced frequency, reduced stiffness and adaptive camber airfoil performance is observed. A third objective is thus to

- investigate the physical processes responsible for gust load alleviation in detached flow.

The experiments are carried out at the TU Darmstadt Eiffel wind tunnel, comprising a pitch-plunge rig and a time resolved particle image velocimetry system. The chapter begins with a presentation of the **experimental setup** in section 5.1. The experimental procedure differs significantly between attached and detached flow regime, both regimes are considered individually. Section 5.2 deals with the **attached flow regime** and the influence of mass inertia as well as the verification of first-order transfer functions. Section 5.3 is concerned with the **detached flow regime** and the investigation of the involved physical processes.

5.1. Experimental Setup

First the TU Darmstadt **Eiffel wind tunnel** and its uniform flow properties are briefly presented. Then the **airfoil kinematics** generated with the pitch-plunge are defined and a description of the **adaptive camber airfoil** model and its instrumentation is given.

5.1.1. Eiffel Wind Tunnel

Figure 5.2 shows a schematic view of the TU Darmstadt Eiffel wind tunnel. The inlet has a cross section of 2.2 m x 2.2 m. A nozzle contraction ratio of 24:1 leads to a cross-section of 0.45 m x 0.45 m in the closed test section. The flow is driven by a fan and a 20 kW motor located 6 m downstream the test section, allowing maximum flow speeds in the empty tunnel of up to 60 m/s. Markus [66] reported that the turbulence level T_u is below 0.2 % and the measured flow velocity $U_\infty(y,z)$ deviates from the averaged flow velocity $\overline{U}_\infty$ by less than 1 % at $U_\infty \approx 15$ m/s in the test section.
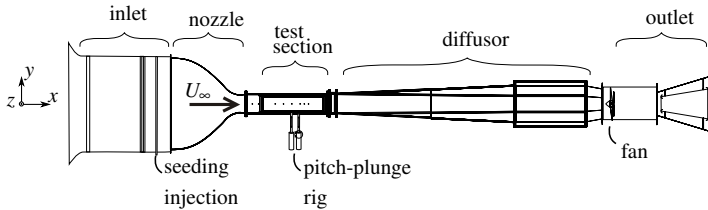
Figure 5.2.: Schematic view of the low speed open return wind tunnel at TU Darmstadt

5.1.2. Airfoil Kinematics

Figure 5.3 shows a schematic view of the pitch-plunge rig. Two linear actuators are installed underneath the test section with a maximal stroke of 240 mm and a maximal speed of 1.7 m/s. The actuators are controlled via *LinMot LinTalk* software and their actual position is traced with two acceleration sensors. If both actuators are in the same vertical position ($\Delta y = 0$), their horizontal distance is 0.085 m. The rigid middle part of the airfoil used in the present study is smaller and is mounted on the actuators pistons via two aluminum adapters. The upstream motor is fixed to

the wind tunnel and its piston is only allowed to perform a vertical movement. The downstream motor can be slightly tilted to account for the change in distance, if the actuators are in different vertical positions ($\Delta y \neq 0$).

(a) Pitch motion   (b) Plunge motion
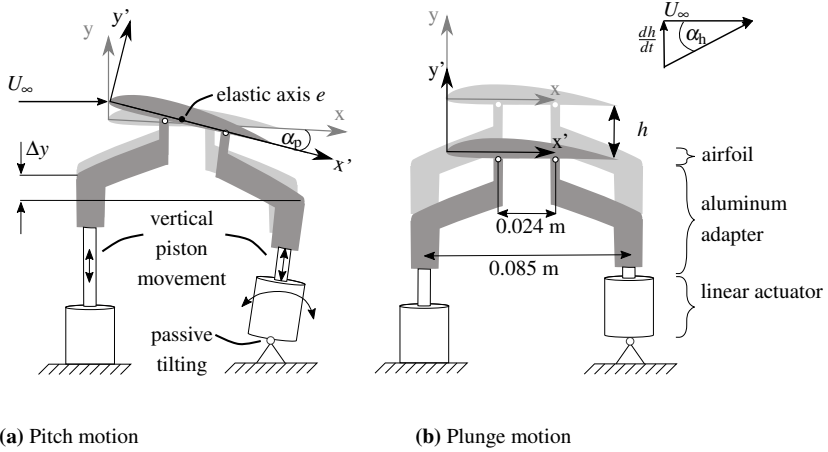
Figure 5.3.: Kinematics of the pitch-plunge rig. The individual control of the two linear actuators allows a variable pitch and plunge motion of the airfoil.

In this study, a pure pitch motion (Figure 5.3a) and a pure plunge motion (Figure 5.3b) are generated. During pitch motion, the linear actuators are moved sinusoidally with different stroke amplitudes and a specified phase such that a sinusoidally varying pitch angle α_p

$$\alpha_p = \widehat{\alpha}_p \sin\left(2\pi f t\right) \tag{5.1}$$

around a fixed elastic axis e is generated. During plunge motion, the actuators are moved sinusoidally with the same stroke amplitude and without phase shift, resulting in a plunge angle of attack α_h of

$$\alpha_h = \widehat{\alpha}_h \sin\left(2\pi f t\right) = \arctan\left(-\frac{1}{U_\infty}\frac{dh}{dt}\right). \tag{5.2}$$

Both α_p and α_h are derived from the motion of the linear actuators and refer to the angle of attack formed between the inflow velocity $U_\infty \vec{e}_x$ and the chordwise direction $\vec{x'}$ of the rigid reference airfoil.

100

5.1.3. Adaptive Camber Airfoil Model

Figure 5.4 gives a schematic view of the two-dimensional airfoil model used during the experimental investigations. The airfoil has a Clark Y profile with a chord length of $c = 0.12$ m and a span of $s = 0.45$ m. Its span covers the entire test section width. The blockage at zero mean angle of attack is 2 % and the maximal blockage at maximal angle of attack of $20°$ is 20 %. The airfoil is manufactured from polyamide by direct laser sintering. Its light weight construction consists of a 0.5 mm skin, reinforced by a truss structure. The total weight of leading-edge and trailing flap is $m_{LE} \approx m_{TE} < 60$ g and the centers of inertia are located at $\Delta x_{LE} = 1$ mm and $\Delta x_{TE} = 3$ mm from the leading-edge and trailing flap hinges, to reduce the effect of mass inertia during the experiments. The airfoil's surface is treated with Rhodamin 6g, which absorbs light at the wavelength of 529.8 nm and fluoresces with 551 nm, see Kubin and Fletcher [55]. The Rhodamin is dissolved in alcohol and blended with clear varnish to generate a heat resistant smooth surface. In combination with an optical bandpass filter, surface reflections on the airfoil from the PIV laser light sheet are efficiently reduced. The restraining spring mechanism is realized by two systems of 11 leg springs, which can be inserted at each side of the airfoil. Each leg spring has a spring stiffness of $\kappa_{\gamma i} = 0.03$ Nm/rad. The system stiffness $\kappa_\gamma = \sum(\kappa_{\gamma_i})$ can be varied from 0.06 to 0.66 Nm/rad in 11 discrete steps. During the experimental investigation presented in this study, two leg springs oppose the upward rotation of the flaps and $\kappa_\gamma = 0.06$ Nm/rad. The coupling of leading-edge and trailing flap is realized via an external two-rod system, which is fixed to both sides of the airfoil. By changing the spring system to a rigid block, the coupling of leading-edge and trailing flap can be fixed in the original Clark Y position. This corresponds to the reference configuration referred to as 'rigid'. A picture of the adaptive camber airfoil model in 'rigid' and 'adaptive' configuration is shown in Figure 5.5. Pressure taps are located on the leading flap at $x/c = 0.06$, 0.11 and 0.14 on both pressure and suction side, at $z/s = 0.1$ from the middle axis. Tubes of 1 mm diameter are located in spanwise direction in the airfoil skin, directly manufactured by laser sintering. Holes of 0.3 mm diameter are drilled through the surface of the airfoil and the polyamide tubes. Plastic hoses are connected to the end of the polyamide tubes and lead the pressure signal to pressure transducers outside the wind tunnel test section. The position of the trailing
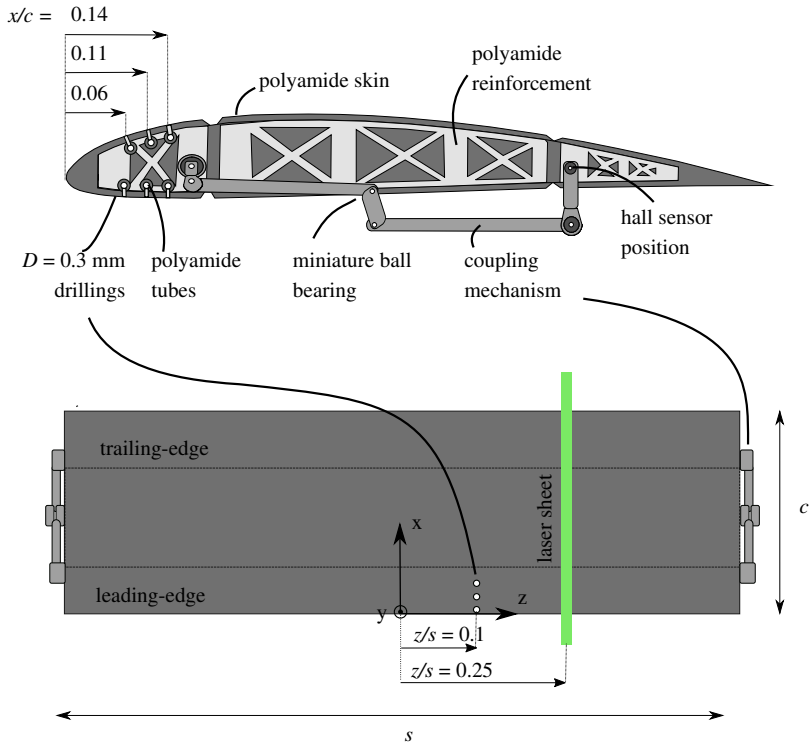
Figure 5.4.: Side and top view of the adaptive camber airfoil model used during the pitch-plunge experiments. The leading-edge is coupled to the trailing flap via an external two-rod coupling mechanism, attached to both sides of the airfoil. The coupling is pre-tensioned by a spring system (not shown) and the trailing flap angle γ is monitored as a measure for the airfoil deformation by a rotary hall sensor. Pressure taps are located at three chordwise positions at the airfoil's leading-edge at $z/s = 0.1$.

flap is measured with an *ams AS5162* rotary hall sensor. The sensor consists of a circuit board and a magnet that rotates over the circuit board, visible in Figure 5.5b. A detailed description of the construction of the airfoil can be found in Klyk [50].
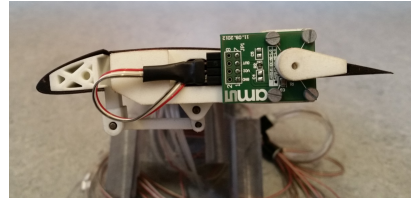
(a) Rigid configuration   **(b)** Adaptive configuration

Figure 5.5.: 2D airfoil model used in the pitch-plunge experiments. (a) Airfoil model in rigid configuration, the coupling between leading-edge and trailing flap is blocked. (b) Airfoil in adaptive configuration, with the rotary hall sensor attached to its trailing flap hinge.

5.2. Attached Flow Regime

In section 5.2.1 the **objectives and investigated parameter space** of the attached flow experiments are explained, which consist of validating first-order transfer functions on the pitching rigid airfoil and investigating the influence of inertial forces due to plunging on the functioning principle of the adaptive camber airfoil. Section 5.2.2 shows the procedure of **data acquisition and reduction**. The section closes with a presentation of the **experimental results** in section 5.2.3.

5.2.1. Objectives and Investigated Parameter Space

The objectives of the oscillating airfoil experiments under attached flow conditions are twofold. On the one hand, the experimental setup offers the opportunity to further investigate first-order transfer functions that describe the unsteady airfoil response in the frequency domain. On the other hand, the pitching and plunging airfoil presents an abstraction of important operating conditions of wind turbines, i.e. a twisting and bending oscillation of the blades. Oscillating motion induces additional inertial forces on the flap system of the adaptive camber airfoil and the effect of inertial effects on the adaptive camber airfoil's performance is studied. All experimentally investigated parameter combinations are summarized in Table 5.1, the pursued objectives are pointed out below.

The experimental parameter set ①️ serves to **verify first-order transfer functions**,

which are introduced in section 3.2, p. 22. This verification is performed for the rigid airfoil only. A verification for the adaptive camber airfoil is omitted, because the first-order transfer function for a forced oscillation is not directly accessible in Spiegelberg's formulation [88]. The first-order transfer function of the unsteady lift response of a rigid airfoil in harmonic pitch motion is the Theodorsen function h_L, cf. section 3.2.2. The direct measurement of unsteady aerodynamic forces on an oscillating airfoil is challenging. Due to the low Reynolds number in the experimental setup, the aerodynamic forces are small and superimposed by inertial forces of the pitching and plunging motion. In the case of the adaptive camber airfoil, additional inertial forces of the flap system occur. In this study, the unsteady lift is not measured directly. During attached flow measurements, the dynamic lift is estimated is estimated by the pressure difference at the leading-edge Δp. A transfer function for the pressure distribution can be derived by means of first-order theory, as shown in section 3.2.2, p. 28, similar to the transfer function of the total lift used in Chapter 4. An integration of Δp yields the total lift L and it is presumed that if the transfer function of the pressure difference $h_{\Delta p}$ agrees with experimental results, the same holds for the Theodorsen function h_L. The linear nature of transfer functions suggests that the ratio between perturbation and response at a distinct reduced frequency remains constant, independent of the perturbation height. This assumption is tested by studying the influence of the pitch amplitude $\widehat{\alpha}_p$ on the pressure response, using the experimental parameter set (1a). In Chapter 4 it is shown that first-order transfer functions do not agree with experimental results in the case of a sinusoidal vertical gust encounter. A hypothesis is conjectured that this disagreement could be due to the fact that first-order theory neglects the distortion of the steady flow field by a lift producing airfoil. Whether the altered steady velocity field is the reason for the disagreement between first-order transfer functions and experimental results is tested with parameter set (1b). Figure 5.6 schematically visualizes the approach. Other than a flat thin plate at zero angle of attack, the presence of a lift producing airfoil distorts the surrounding stream lines. For a cambered airfoil, such as the Clark Y airfoil, the smallest distortion of the velocity field is achieved at the zero-lift angle of attack $\alpha_0 < 0°$. At this mean angle of attack, the assumption of undistorted flow is most likely fulfilled and agreement between theory and experimental results should be best. With increasing mean angle of attack $\alpha_m > \alpha_0$, the presence of an airfoil
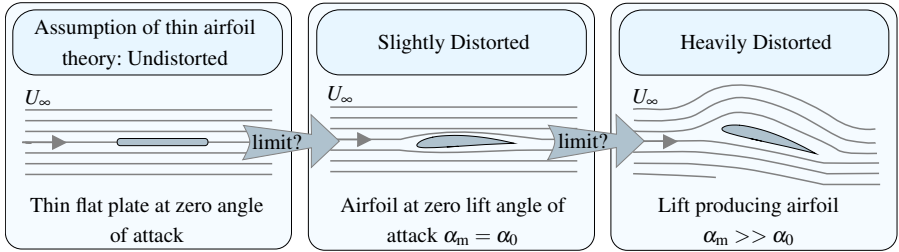
Figure 5.6.: Schematic visualization of the objectives of parameter set ①b : First-order transfer functions assume undistorted flow with straight streamlines. The presence of an airfoil alters the steady velocity field and deflects the stream lines. The limits of applicability of first-order transfer functions are tested by steadily increasing the airfoil's mean angle of attack α_m.

distorts the surrounding velocity field and deflects the stream lines. The assumption of an unperturbed surrounding flow field is violated, which could explain a deviation between and experimental results and theory. The hypothesis is tested by deriving experimental transfer functions at various α_m and comparing the result to the theoretical first-order transfer function.

The **influence of mass inertia on adaptive camber airfoil performance** is studied using parameter set ②. While the adaptive camber airfoil is only actuated by aerodynamic forces for the case of the sinusoidal vertical gust encounter studied in Chapter 4, additional forces arise from the inertia of the flap system in the case of an oscillating airfoil. According to Spiegelberg [88], the adaptive camber airfoil's inertial forces can be described by the transfer function of a classic linear dynamic system. This transfer function takes the form $(-\eta^2 \tilde{M} + i\eta \tilde{D} + \tilde{K})$, where $\tilde{M}$, $\tilde{D}$ and $\tilde{K}$ are the structural mass, damping and stiffness matrices of the system, respectively. The mass matrix $\tilde{M}$ depends on the structural properties of the adaptive camber airfoil. For the complete formulation, the reader is referred to Spiegelberg [88], equation C.3, p. 157. Figure 5.7 shows influencing parameters on a simplified model of the adaptive camber airfoil, considering neither coupling of leading and trailing flap, stiffness nor damping. Each flap exhibits inertial moments M_inertia, which can be decomposed in an inertial moment due to translation M_trans and an inertial moment

(a) Pitch motion **(b)** Plunge motion
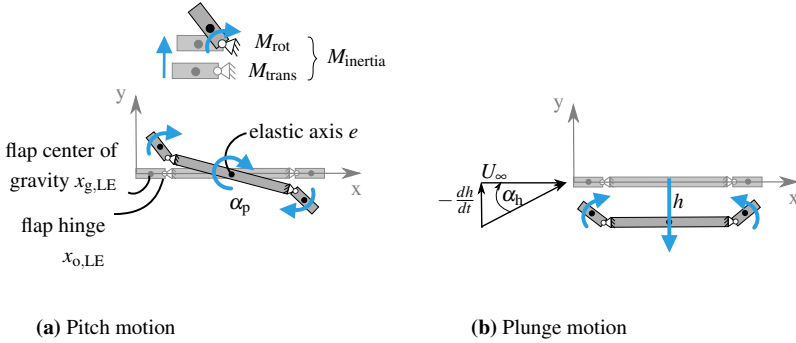
Figure 5.7.: Schematic visualization of the influence of mass inertia on the adaptive camber airfoil performance. Depending on the structural properties, inertial moments M_{inertia} can enhance or reduce the driving aerodynamic moments M_{aero}.

due to rotation M_{rot}. From the schematic visualization of Figure 5.7 it is evident that these moments depend highly on the adaptive camber airfoil's structural properties, i.e. its flap centers of gravity, the hinge positions, the coupling ratio between leading and trailing flap but also on the movement pattern. The adaptive camber airfoil's de-cambering is determined by the phase and amplitude of both the inertial moments M_{inertia} and the aerodynamic moment M_{aero} around leading-edge. The aerodynamic moment M_{aero} generally follows the aerodynamic angle of attack α with a small phase shift. This guarantees the working principle of the adaptive camber airfoil. An increasing α yields an increasing M_{aero} that de-cambers the airfoil and leads to de-creased load pick up. If inertial moments M_{inertia} are superimposed to M_{aero} such that the airfoil's camber increases with increasing α, the working principle of the adap-tive camber airfoil is inverted, resulting in enhanced fluctuating loads. On the other hand, if M_{inertia} is in phase with M_{aero}, the actuation of the adaptive camber airfoil is enhanced, which enhances gust load alleviation. While alleviating fluctuating loads is favorable when encountering a gust, alleviating all load fluctuations could become problematic in the case of blade bending oscillations. The fluctuating aerodynamic forces induce a positive aerodynamic damping which is needed in order to quickly reestablish normal operating conditions and limit fatigue. If bending oscillations are not damped out by aerodynamic forces, all energy has to be absorbed by the struc-ture, possibly increasing fatigue. This fact has to be taken taken into account when

evaluating the benefits of the adaptive camber airfoil in terms of fatigue on an actual wind turbine. Understanding the interaction between inertial and aerodynamic forces on an oscillating airfoil is thus necessary to evaluate the adaptive camber airfoil in the context of wind turbine applications. The aeroelastic response of the adaptive camber airfoil cannot be accessed directly from the formulation of Spiegelberg for the case of a forced plunging motion in constant free stream. Therefore, a purely experimental investigation on how inertial forces alter the adaptive camber airfoil performance is carried out.

Table 5.1.: Summary of the experimental parameters.

		Verification of 1$^{\text{st}}$ order transfer functions	
airfoil		rigid airfoil only	
motion		pure pitch	
f_{p}	[Hz]	2 : 1 : 12	2 : 1 : 12
U_∞	[m/s]	15	15
k	[ ]	0.05...0.3	0.05...0.3
α_{m}	[°]	2	-4, -2, 2, 5, 8
$\widehat{\alpha}_{\text{p}}$	[°]	2, 4, 6	4
		Set (1a) verification of linearity	Set (1b) limits of applicability

		Influence of mass inertia on adaptive camber airfoil performance
airfoil		rigid vs. adaptive
motion		pure plunge
f_{h}	[Hz]	2 : 1 : 12
U_∞	[m/s]	0, 15
k	[ ]	0.05...0.3
α_{m}	[°]	5
$\widehat{\alpha}_{\text{h}}$	[°]	1.5
		Set (2) influence of inertia during pure plunge

5.2.2. Data Acquisition and Reduction

First, the **data acquisition** is described, followed by a derivation of the **experimental transfer function of the pressure difference** and the **experimental transfer function of the motion response**. An estimation of the measurement uncertainties of all measurands is given in appendix A.2.

Data Acquisition

All measured values (pressure, trailing flap deflection and acceleration of the pitch-plunge rig) are acquired with a *NI 6210* AD converter, operating at an input range of 5 V and a sampling rate of $f_s = 1\,\text{kHz}$. Pressure data are acquired using *First Sensor* HCL pressure transducers with full scales of 5 mbar (pressure side) and 12.5 mbar (suction side). The electric full scale output signals of 20 mV are augmented to the maximal input of the AD converter with in-house fabricated adjustable amplifiers to obtain maximal resolution. The trailing flap deflection is measured using an *ams AS5162* rotary hall sensor. The sensor provides a linear analog output over a full turn of 360° and allows programming of start and stop positions in order to increase full scale resolution for smaller measurement ranges. Start and stop positions are set at the maximal and minimal flap deflections, to exploit the data acquisition device input range optimally.

During quasi-steady reference measurements, the airfoil's mean angle of attack α_m is augmented from $-10° < \alpha_m < 20°$ in steps of 1°. Data are acquired for $T = 20\,\text{s}$ and a simple arithmetic mean is taken to describe each measuring point.

During dynamic measurements, the airfoil is oscillated continuously with a dynamic angle of attack $\alpha_{\text{dyn}} = \widehat{\alpha}_{\text{dyn}} \sin(2\pi f t)$ around a mean angle of attack of α_m. The dynamic angle of attack is generated by a pure pitching motion with a pitching amplitude of $\widehat{\alpha}_{\text{dyn}} = \widehat{\alpha}_p$ or by a pure plunging motion with an amplitude of $\widehat{\alpha}_{\text{dyn}} = \widehat{\alpha}_h$. Data are acquired for $T = 10\,\text{s}$ and phase averaged with the oscillation frequency f. The instantaneous dynamic angle α_{dyn} is obtained from two *Freescale Semiconductor* MMA1270KEG acceleration sensors fixed to the linear actuators of the pitch-plunge rig and serves as the phase reference.

Experimental Transfer Function of the Pressure Difference $h^*_{C_{\Delta p}}$

The lift force is not directly accessible in the present experimental setup. The coefficient of the pressure difference on the airfoil's leading-edge $C_{\Delta p}$ serves as an estimator for the lift, as proposed by Gaunaa and Andersen [27]. Similar to the pressure coefficient C_p, the coefficient of the pressure difference between suction side (SS) and pressure side (PS) of the airfoil is defined as

$$C_{\Delta p} = C_{p,\text{SS}} - C_{p,\text{PS}} = \frac{p_{SS} - p_{PS}}{\frac{\rho}{2}U_\infty^2} \tag{5.3}$$

Analog to the transfer function of the load h_L that relates the dynamic lift response to a quasi-steady approximation, a transfer function of the pressure difference $h_{C_{\Delta p}}$ is obtained by relating the dynamic pressure difference $C_{\Delta p,\text{dyn}}$ to its quasi-steady counterpart $C_{\Delta p,\text{qs}}$.

$$h_{C_{\Delta p}} = \frac{\widehat{C}_{\Delta p,\text{dyn}}}{\widehat{C}_{\Delta p,\text{qs}}} \frac{e^{i(\omega t + \varphi_{C_{\Delta p}})}}{e^{i\omega t}} = \widehat{h}_{C_{\Delta p}} e^{i\varphi_{C_{\Delta p}}} \tag{5.4}$$

The theoretical transfer function of the pressure difference $h_{C_{\Delta p}}$ is obtained from the formulation of the unsteady pressure distribution Δp_{dyn} on an oscillating airfoil given by Mateescu and Abdo [68], see section 3.2.2, p.28. The experimental value of $h^*_{C_{\Delta p}}$ is obtained from pressure measurements on the suction and pressure side of the airfoil at the same chordwise position $x/s = 0.11$. The quasi-steady value $\widehat{C}^*_{\Delta p,\text{qs}}$ is obtained by

$$\widehat{C}^*_{\Delta p,\text{qs}} = \frac{\partial C^*_{\Delta p,\text{qs}}}{\partial \alpha} \cdot \widehat{\alpha}_{\text{dyn}} \tag{5.5}$$

where $\partial C^*_{\Delta p,\text{qs}}/\partial \alpha$ is the slope of the coefficient of the pressure difference in the region of attached flow, derived from quasi-steady reference measurements and $\widehat{\alpha}_{\text{dyn}}$ is amplitude of the dynamic angle of attack due to a pitching or a plunging of the airfoil. The amplitude $\widehat{C}^*_{\Delta p,\text{dyn}}$ and phase $\varphi^*_{C_{\Delta p}}$ are derived from phase averaged dynamic pressure measurements, such that:

$$C^*_{\Delta p,\text{dyn}} = \widehat{C}^*_{\Delta p,\text{dyn}} \sin(2\pi f t + \varphi^*_{C_{\Delta p}}) \tag{5.6}$$

Experimental Transfer Function of the Motion Response h_γ^*

According to its definition of section 3.2.3, p. 33, the transfer function of motion h_γ relates the fluctuating trailing flap angle γ' to the dynamic angle of attack α_{dyn}:

$$h_\gamma = \frac{\widehat{\gamma}}{\widehat{\alpha}_{\mathrm{dyn}}} \frac{e^{i(\omega t + \varphi_\gamma)}}{e^{i\omega t}} = \frac{\widehat{\gamma}}{\widehat{\alpha}_{\mathrm{dyn}}} e^{i\varphi_\gamma} \tag{5.7}$$

The experimental amplitude $\widehat{\gamma}^*$ is derived from phase averaged measurements

$$\gamma^* = \widehat{\gamma}^* \sin(2\pi f + \varphi_\gamma^*). \tag{5.8}$$

The phase φ_γ^* is related to the dynamic angle

$$\alpha_{\mathrm{dyn}}^* = \widehat{\alpha}_{\mathrm{dyn}}^* \sin(2\pi ft), \tag{5.9}$$

which is obtained from the acceleration sensor signals of the pitch-plunge rig.

5.2.3. Experimental Results

Experimental transfer functions for the pressure difference $h_{C_{\Delta p}}$ are obtained from phase averaged data as explained in section 5.2.2. The corresponding quasi-steady reference measurements are given in appendix C.2. The presentation of the results follows the outline given in section 5.2.1.

Verification of 1$^{\mathrm{st}}$ Order Transfer Functions

Verification of Linearity - Parameter Set (1a)

Figure 5.8 compares the experimental and theoretical transfer function of the pressure difference $h_{\Delta C_p}$ for a rigid airfoil oscillating in pure pitch around its leading-edge ($e = 0$) for various pitching amplitudes $\widehat{\alpha}_p$. The theoretical transfer function is independent of the pitch amplitude $\widehat{\alpha}_p$ and the mean angle of attack α_m. In the experiments, the airfoil is pitched with various $\widehat{\alpha}_p$ around $\alpha_m = 2°$ in a free stream of $U_\infty = 15\,\mathrm{m/s}$. The magnitude of the transfer function $|h_{\Delta C_p}|$ is displayed in Figure 5.8a, the phase $\varphi_{\Delta C_p}$ is displayed in Figure 5.8b. According to linear theory, the pitching amplitude $\widehat{\alpha}_p$ has no influence on the transfer function. This is confirmed by the experimental results and is in good agreement with the findings of Chapter 4 of the sinusoidal vertical gust encounter and the results of Halfman [31] of a harmonically pitching NACA 0012 airfoil.
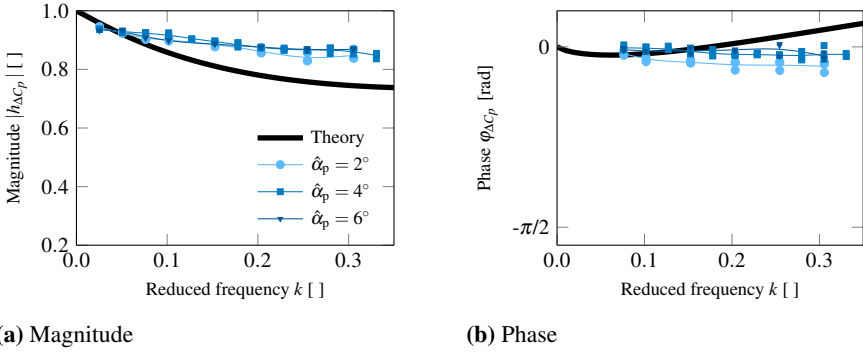
(a) Magnitude

(b) Phase

Figure 5.8.: Magnitude $|h_{\Delta C_p}|$ and phase $\varphi_{\Delta C_p}$ of the transfer function of the pressure difference ΔC_p on a continuously pitching rigid airfoil. The airfoil is pitched around its leading-edge at a mean angle of attack $\alpha_m = +2°$ with the indicated pitch amplitude $\widehat{\alpha}_p$ at an inflow velocity of $U_\infty = 15\,\text{m/s}$. Experimental values, indicated by marker symbols, are compared to a first-order solution given by Mateescu and Abdo [68].

Limits of Applicability - Parameter Set ①b

Figure 5.9 compares the experimental and theoretical transfer function of the pressure difference $h_{\Delta C_p}$ for a rigid airfoil pitched continuously around its leading-edge ($e = 0$) for various mean angles of attack α_m. The theoretical transfer function is independent of the mean angle of attack α_m and the pitch amplitude $\widehat{\alpha}_p$. In the experiments, the airfoil is pitched with $\widehat{\alpha}_p = 4°$ at $U_\infty = 15$ m/s around different α_m in the range of $-4° \leq \alpha_m \leq +8°$. The magnitude of the transfer function $|h_{\Delta C_p}|$ is displayed in Figure 5.9a, the phase $\varphi_{\Delta C_p}$ is displayed in Figure 5.9b. At $\alpha_m = -4°$, magnitude and phase of experimental and theoretical values agree reasonably well. Note that this is the angle of attack which produces zero mean pressure difference $C_{\Delta p} = 0$ under quasi-steady conditions, cf. Figure C.4a, p. 179. With increasing α_m, the difference between experimental and theoretical values increases. At the highest mean angle of attack of $\alpha_m = +8°$, significant differences are observed between experimental values and theoretical prediction. The magnitude $|h_{\Delta C_p}|$ of experimental and theoretical values shows an opposite frequency dependence and approaches different values for $k \to 0$. The phase $\varphi_{\Delta C_p}$ shows a significant offset between experimental and theoretical values. A very similar behavior is observed for the sinusoidal vertical gust encounter of Chapter 4, cf. Figure 4.17 and Figure 4.18, p. 85.
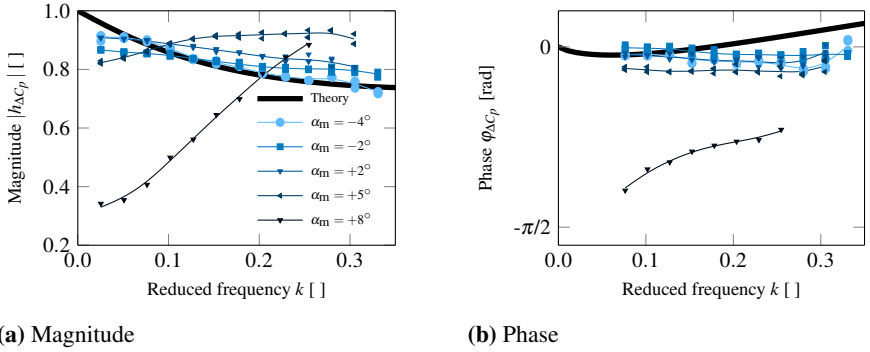
(a) Magnitude

(b) Phase

Figure 5.9.: Magnitude $|h_{\Delta C_p}|$ and phase $\varphi_{\Delta C_p}$ of the transfer function of the pressure difference ΔC_p on a continuously pitching rigid airfoil. The airfoil is pitched around its leading-edge at the indicated mean angle of attack α_m with a pitching amplitude $\widehat{\alpha}_p = 4°$ at an inflow velocity of $U_\infty = 15\,\text{m/s}$. Experimental values, indicated by marker symbols, are compared to a first-order solution given by Mateescu [68].

Influence of Mass Inertia on the Adaptive Camber Airfoil's Performance

Pure Plunge - Parameter Set (2a)

Figure 5.10 shows the motion response of the adaptive camber airfoil's trailing flap h_γ to a pure plunging motion. In Figure 5.10a, the flow velocity is set to $U_\infty = 0\,\text{m/s}$ and the motion response of the adaptive camber airfoil is only due to the inertial forces of the flap system. The magnitude $|h_\gamma|$ increases with increasing plunging frequency f_h and the phase φ_γ remains in the range of $0 < \varphi_\gamma < \pi$. This is the expected behavior for a linear spring mass damper system submitted to perturbations with increasing excitation frequencies below its system resonance. In Figure 5.10b, the flow velocity is set to $U_\infty = 15\,\text{m/s}$ and the motion response of the adaptive camber airfoil is a result of inertial and aerodynamic forces. As for $U_\infty = 0\,\text{m/s}$ (Figure 5.10a), the magnitude $|h_\gamma|$ increases with increasing reduced frequency, but at a higher rate. The phase of the motion response φ_γ increases for the inflow velocity $U_\infty = 15\,\text{m/s}$ from $\varphi_\gamma \approx -\pi/2$ at $k = 0$ to $\varphi_\gamma \approx -\pi/4$ at $k = 0.3$. The phase lag between the motion response and the excitatory plunge angle of attack α_h remains below $|\varphi_\gamma| < \pi/2$ and decreases with increasing k. The magnitude of the motion response increases with increasing k. This indicates that the inertial forces enhance the adaptive camber airfoil's
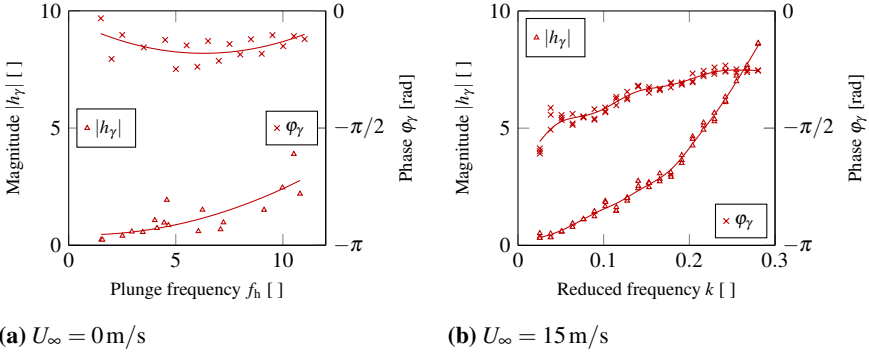
(a) $U_\infty = 0\,\mathrm{m/s}$

(b) $U_\infty = 15\,\mathrm{m/s}$

Figure 5.10.: Magnitude and phase of the motion response h_γ for $U_\infty = 0\,\mathrm{m/s}$ (a) and $U_\infty = 15\,\mathrm{m/s}$ (b). Discrete experimental data are indicated by marker symbols, a cubic spline interpolation emphasizes the frequency dependence. The investigated plunging frequencies f_h in (a) correspond to the reduced frequencies k in (b). The mean angle of attack is set to $\alpha_m = 5°$. The plunge motion corresponds to a plunge amplitude of $\alpha_h = 1.5°$ at $U_\infty = 15\,\mathrm{m/s}$.

gust load alleviation capabilities with increasing k, as most efficient gust load alleviation is expected for high $|h_\gamma|$ and small $|\varphi_\gamma|$. Figure 5.11 shows the corresponding aerodynamic response of the adaptive camber airfoil and the rigid reference airfoil. The aerodynamic response is quantified by the coefficient of the pressure difference between suction and pressure side on the leading-edge $C_{\Delta p}$, see equation 5.2.2, p. 110. Note that Figure 5.11a shows the amplitude $\widehat{C}_{\Delta p_{\mathrm{dyn}}}$ and not the magnitude of the transfer function $|h_{C_{\Delta p}}| = \widehat{C}_{\Delta p_{\mathrm{dyn}}}/\widehat{C}_{\Delta p_{\mathrm{qs}}}$, as a normalization with $\widehat{C}_{\Delta p_{\mathrm{qs}}}$ complicates a comparison between the rigid and the adaptive camber airfoil. The rigid airfoil's $\widehat{C}_{\Delta p_{\mathrm{dyn}}}$ increases with increasing reduced frequency k. The adaptive camber airfoil's $\widehat{C}_{\Delta p_{\mathrm{dyn}}}$ decreases with increasing k. This can be attributed to a more efficient manipulation of fluctuating loads with increasing k and is in good agreement with the motion response of the adaptive camber airfoil shown in Figure 5.10b. Figure 5.11b shows the phase $\varphi_{C_{\Delta p}}$ between $C_{\Delta p_{\mathrm{dyn}}}$ and the plunging angle of attack α_h. Both pressure responses lag the pitching angle of attack ($\varphi < 0$), the de-cambering of the adaptive camber airfoil introduces an additional phase lag. For $k \geq 0.2$, the adaptive camber airfoil damps the loads so efficiently that $\widehat{C}_{\Delta p_{\mathrm{dyn}}} \approx 0.1$ and no distinct phase can be assigned.
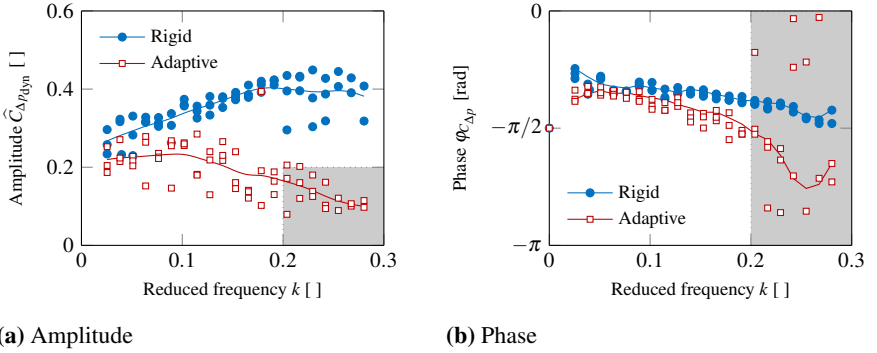
114

Figure 5.11.: Amplitude and phase of the coefficient of the pressure difference on the airfoil's leading-edge $C_{\Delta p}$ as a function of the reduced frequency. The airfoils are oscillated in a pure plunge motion at a mean angle of attack $\alpha_m = 5°$ with a plunging angle of attack $\alpha_h = 1.5°$ at an inflow velocity of $U_\infty = 15\,\mathrm{m/s}$. In the region highlighted in gray at $k \geq 0.2$, the combined influence of inertial and aerodynamic forces actuates the adaptive camber airfoil so efficiently that no distinct phase can be attributed to the adaptive camber airfoil's $C_{\Delta p}$.

For an airfoil oscillating in pure pitch motion, inertial forces and the resulting motion response and aerodynamic response depend highly on the elastic axis e around that the airfoil is oscillated. Results of an experimental investigation of the dynamic response of a pitching airfoil with adaptive camber mechanism are reported by Meißner [70].

Conclusions

The **verification of first-order transfer functions** is performed for the rigid airfoil only. A systematic investigation of the adaptive camber airfoil is omitted, as no theoretical transfer function for the forced pitching condition exists. In the case of a sinusoidal vertical gust encounter, where a theoretical transfer functions for the adaptive camber airfoil is given by Spiegelberg [88], the theoretical transfer functions of rigid and adaptive camber airfoil follow the same behavior and show the same discrepancy to the experimental results. It can thus be assumed that the following conclusions hold for the adaptive camber airfoil as well.

First-order transfer functions are derived using the approximation of a thin flat plate at zero angle of attack that does not alter the surrounding velocity field. If the surrounding velocity field remains unperturbed, the thin flat plate cannot produce a mean pressure difference or a mean lift.

- Experimental results agree reasonably well with first-order theory, if the perturbation is applied around an angle of attack that produces zero mean pressure difference.

It is shown in Figure 5.8 that the transfer function of an airfoil pitching around $\alpha_m = -4°$ agrees with theoretical predictions. From quasi-steady reference measurements in Figure C.4a, p. 179 it can be seen that $\alpha_m = -4°$ is exactly the angle where $\Delta C_{p,\text{qs}} = 0$.

- If the perturbation is applied around a lift producing angle $\alpha_m > \alpha_0$, the experimentally observed behavior differs from theoretical predictions.

In the case of an airfoil pitching around $\alpha_m \geq 5°$, significant differences between experimental and theoretical $h_{\Delta C_p}$ are observed. This is a rather high α_m and the fact that first-order theory fails to capture the experimentally observed behavior is understandable. For the case of the sinusoidal vertical gust encounter of Chapter 4, theoretical and experimental values showed the same significant differences at relatively small mean angles of attack of $\alpha_m = 2°$. According to Dowell [22] and Hodges and Pierce [35], first-order transfer functions are state-of-the-art design tools in flutter calculation for engineering applications. The experimental results reveal the limits of applicability of first-order transfer functions and emphasize that first-order transfer functions have to be applied with caution: The generation of a mean lift violates the assumptions upon which first-order transfer functions are built.

The **influence of the mass inertia** has major impact on the adaptive camber airfoil's performance.

- Pure plunging motion enhances the adaptive camber airfoil's motion response and gust load alleviation performance.

Alleviating load fluctuations is the purpose during normal operating conditions. On a wind turbine blade in bending oscillation, the fluctuating aerodynamic loads are

opposing the bending motion. Aerodynamic forces induce a positive aerodynamic damping that attenuates the blade oscillation. If bending oscillations are not damped out by aerodynamic forces, all energy has to be absorbed by the structure, possibly increasing fatigue. This fact has to be taken into account when evaluating the benefits of the adaptive camber in terms of fatigue on actual wind turbines.

5.3. Detached Flow Regime

At high mean angles of attack, the flow separates from the airfoil and viscous forces become predominant over pressure forces. The pressure difference Δp is no longer an adequate parameter to estimate the airfoil lift. Neither are first-order transfer functions an adequate tool to predict the unsteady airfoil response. At high mean angles of attack, dynamic flow perturbations lead to a phenomenon typically referred to as dynamic stall. Dynamic stall is accompanied by leading-edge vortices (LEV) and high transient forces, as discussed in section 3.3. Various parameters influence dynamic stall and the LEV evolution. The **objectives and the investigated parameter space** are explained in section 5.3.1. LEV circulation scales with the dynamic forces exhibited by the airfoil. The **data acquisition and reduction** procedures used to obtain LEV circulation from time resolved particle image velocimetry data are presented in section 5.3.2. Finally, the **experimental results** are presented in section 5.3.3.

5.3.1. Objectives and Investigated Parameter Space

As pointed out in section 3.3, the coherent LEV that emerge during dynamic stall produces highly localized forces at the airfoil's leading-edge. On the adaptive camber airfoil, these forces are sufficient to actuate the adaptive camber mechanism. The LEV themselves are highly sensitive to the conditions at the airfoil's leading-edge, i. e. the airfoil's effective angle of attack. The effective angle of attack changes as the airfoil de-cambers. Figure 5.12 graphically illustrates the considerations: The shear layer velocity profile is determined by the relative velocity between outer flow and airfoil surface $\Delta U|_0^\delta$. On the adaptive camber airfoil, the leading-edge rotates with a rotational velocity of $\frac{1}{N} \frac{d\gamma}{dt}$, with γ being the trailing flap angle and N the me-
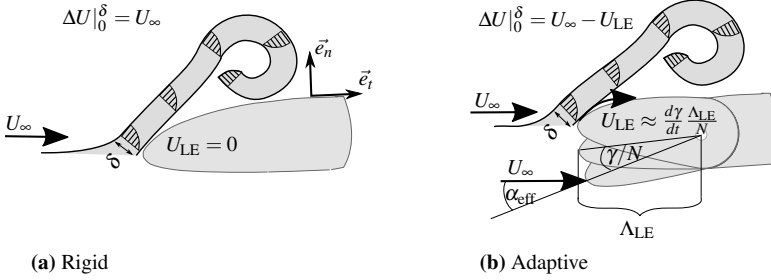
Figure 5.12.: The rotation of the adaptive camber airfoil's leading-edge alters the velocity difference $\Delta U|_0^\delta$ over the feeding shear layer. This influences the vortex growth rate.

chanical coupling ratio between leading-edge and trailing flap. This rotation alters the feeding shear layer strength due to the no-slip boundary condition on the airfoil surface by $\Delta U|_{0,\text{ad}}^\delta = \Delta U|_{0,\text{rig}}^\delta - U_{\text{LE}}$, where U_{LE} is the surface velocity of the rotating leading-edge that is proportional to $\frac{d\gamma}{dt}$ and $\frac{d\alpha_{\text{eff}}}{dt}$. The vortex growth rate $\dot{\Gamma}$ is determined by $\Delta U|_0^\delta$ and accordingly both $\dot{\Gamma}$ and $\Gamma_{\text{max}} = \int \dot{\Gamma} dt$ are altered by the adaptive camber airfoil's flap rotation. In an otherwise identical experimental setup, a difference in maximal circulation on the rigid and the adaptive camber airfoil $\Gamma_{\text{max,rigid}} - \Gamma_{\text{max,adaptive}}$ can be attributed to the de-cambering of the airfoil. It follows that

$$\Gamma_{\text{max,rigid}} - \Gamma_{\text{max,adaptive}} \propto \int U_{\text{LE}} dt \propto \Delta\gamma \propto \Delta\alpha_{\text{eff}} \tag{5.10}$$

where Δ defines the difference between maximal and minimal value during the complete pitch cycle. On rigid airfoils, the LEV growth rate $\dot{\Gamma}$ is mainly determined by the effective angle off attack and thus the motion history. Baik et al. [5] and Widmann and Tropea [105] kept the effective angle of attack history constant and varied the inflow velocity, chord length or percentage of plunging and pitching motion in order to isolate the effect of reduced frequency k and Strouhal number Sr on the normalized circulation $\Gamma/\pi U_\infty$. The unsteady flow encountered by a wind turbine blade can also be quantified in terms of k and Sr. On the adaptive camber airfoil, isolating the effects of reduced frequency k and Strouhal number Sr in a combined pitch and plunge motion yields several difficulties. Changing the percentage of pitch and plunge motion leads to different mass inertia effects on the flap system. A change in inflow
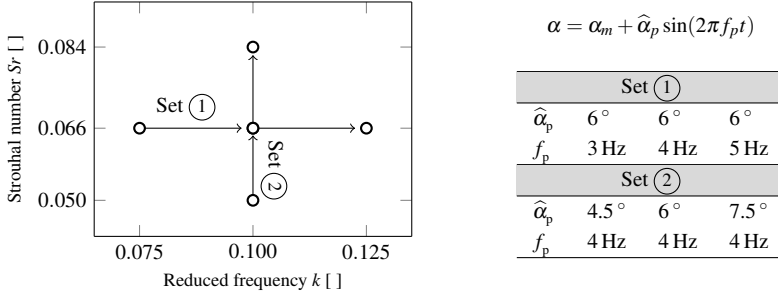
$$\alpha = \alpha_m + \widehat{\alpha}_p \sin(2\pi f_p t)$$

Set ①		
$\widehat{\alpha}_p$	6°	6°	6°
f_p	3 Hz	4 Hz	5 Hz
Set ②		
$\widehat{\alpha}_p$	4.5°	6°	7.5°
f_p	4 Hz	4 Hz	4 Hz

Figure 5.13.: Investigated parameters combinations, displayed in the Strouhal number - reduced frequency plane and the corresponding dimensional pitch frequencies f_p and pitch amplitudes $\widehat{\alpha}_p$. The inflow velocity is kept constant at $U_\infty = 15\,\text{m/s}$ to keep the adaptive camber airfoil's reduced system stiffness constant. The airfoil is oscillated continuously in pure pitch motion around its c/2 axis. The mean angle of attack is $\alpha_m = 14°$.

velocity U_∞ leads to a different reduced stiffness of the adaptive camber airfoil. Both parameters are suspected to significantly alter the adaptive camber airfoil's behavior. In this study, only pure continuous pitching motions around the airfoil's $e = c/2$ axis are performed. This elastic axis has the smallest inertia influence on the flap system, as reported by Meißner [70]. The inflow velocity is $U_\infty = 15\,\text{m/s}$ and the mean angle of attack is set to $\alpha_m = 14°$. The reduced frequency k is varied by changing only the pitching frequency and the Strouhal number Sr is varied by changing only the pitching amplitude. This effectively limits the range of k and Sr but keeps the influence of mass inertia and reduced stiffness as low as possible. Fully exploiting the dynamic properties of the pitch-plunge rig yields the parameter combinations given in Figure 5.13. Two different sets are carried out: In set ① k is varied, keeping the Sr constant at $Sr = 0.066$. In set ② the Sr is varied and k is set to $k = 0.1$.

5.3.2. Data Acquisition and Reduction

This section explains how dimensional, two-component, time resolved particle image velocimetry (2D2C TR PIV) data are acquired and processed to obtain two-dimensional velocity vector fields. From the velocity vector fields, coherent LEV are identified and their circulation is calculated by integration of the vorticity inside the LEV boundaries. An estimation of the measurement uncertainties of all acquired

measurands is given in appendix A.2.

Data Acquisition

2D2C TR PIV field data are acquired using the measurement system schematically shown in Figure 5.14. A *Litron LDY-303* high speed Nd:YLF dual cavity laser is
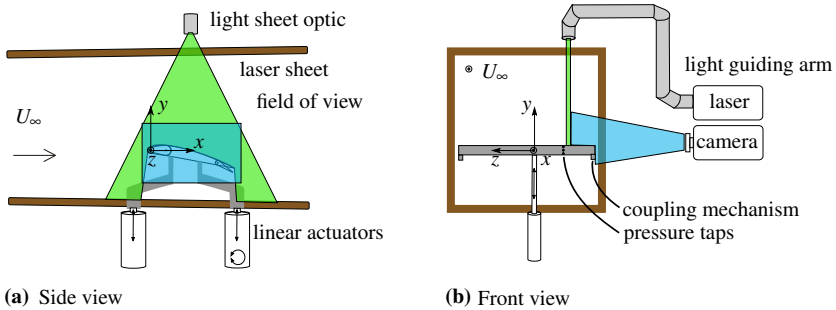

(a) Side view   **(b)** Front view

Figure 5.14.: Schematic view of the PIV setup. A laser sheet in the $x - y$ plane illuminates seeding particles in the flow around the airfoil. A camera is located outside the wind tunnel with its optical axis normal to the laser sheet. The field of view (FoV) comprises the whole airfoil chord length.

installed outside the wind tunnel. The laser has a wavelength $\lambda = 527$ nm and is operated in single frame mode at 10 kHz with its maximum output energy. A light guiding arm guides the laser beam to a light sheet optic installed above the wind tunnel. A laser sheet of approximately 2 mm thickness is produced at the airfoil's quarter span. The laser sheet illuminates DEHS (Di-Ethyl-Hexyl-Sebacat) seeding particles. The seeding particles are atomized with a mean diameter of 0.9 μm in the settling chamber and transported with the flow in the test section. The flow field is captured by a *Phantom v 12.1* high speed CMOS camera controlled with *Phantom V PCC 2.5* acquisition software. The camera is installed at approximately 0.6 m distance from the laser sheet outside the wind tunnel and is equipped with a *Carl Zeiss Makro Planar 2/50ZF* lens and a bandpass filter of 20 nm bandwidth and 532 nm mid-band frequency. Together with the adaptive camber airfoil's rhodamine coating, surface reflexions are minimized. The camera's optical axis is normal to the laser sheet, capturing the whole airfoil's chord length with a resolution of 800 x

600 pixels. The field of view spans 185x140 mm^2, which corresponds to a resolution of approximately 4.3 pixels/mm.

PIV Correlation

The raw images are masked to remove spurious gray scale values due to reflections on the airfoil's surface and suppress regions where no seeding particles can be correlated. During the pitch-plunge experiments, the airfoil moves continuously through the field of view (FoV). In the case of the adaptive camber airfoil, leading-edge and trailing flap introduce an additional degree of freedom and move independently from the airfoil kinematics of the pitch-plunge rig. Knowing the kinematics imposed by the pitch-plunge rig, airfoil shape and trailing flap angle for each instant in time, a mask is produced in *Matlab*. After masking the airfoil in all recordings, an adaptive cross-correlation is performed using *PIVview2C*. According to Raffel et al. [76] good correlations are obtained for particle displacements of about 25 % of the interrogation area (IA) size. Since local flow velocities may be significantly higher than the main stream velocity U_∞, a relatively large IA size of 256 x 256 pixels is reduced by a stepwise refinement scheme to an ending IA size of 16 x 16 pixels. This showed to be a good trade-off between spatial resolution, computing power and invalid vectors. An IA overlap of 50% leads to a grid spacing of 2 mm. From the raw vector maps, invalid vectors are identified with a normalized median test of 3 x 3 IA. Approximately 6 % of the vectors are outliers and are replaced via bi-linear interpolation. From the obtained vector fields at a sampling rate of $f_s = 10$ kHz, an average of three vector maps is taken, leading to a time resolution of $f_{res} = 3.33$ kHz. This eliminates small scale fluctuations but facilitates the identification of large scale coherent structures, which is the main goal of this study.

Vortex Identification

The circulation Γ of a region of area A, enclosed by a boundary B can be calculated by integrating the component of the vorticity vector $\vec{\omega} = \frac{1}{2}\text{rot}\vec{u}$ normal to the considered area A or by integrating the velocity vector $\vec{u}$ along the boundary B:

$$\Gamma = \int_A \vec{\omega} \cdot \vec{n}\,dA = \oint_B \vec{u} \cdot d\vec{x} \tag{5.11}$$

In the two-dimensional $x - y$ plane, the velocity vector $\vec{u} = (u, v)$ is fully described by the flow component in x-direction u and the flow component in y-direction v. The vorticity vector reduces to $\omega_z = \frac{1}{2}\left(-\frac{\partial u}{\partial y} + \frac{\partial v}{\partial x}\right)$. From PIV data, velocity vector fields $\vec{u}(x, y)$ are obtained in the $x - y$ plane. To calculate Γ of a coherent LEV, the boundary B or the area A of this coherent LEV have to be known. Integrating ω_z in the whole FoV would lead to erroneous results, as the shear layer, the airfoil wake or regions of detached flow also contain vorticity. Several ways to identify vortex boundaries exist. Kolar [53] reviewed methods to extract vortex boundaries from the local flow properties using velocity gradients $\nabla \vec{u} = \partial u_j / \partial x_i$. These methods are common in the post processing of numerical data. In experimentally obtained data, small scale velocity fluctuations due to measurement errors occur. Vortex identification schemes based on local methods are highly sensitive for these small scale velocity fluctuations and the application is challenging. Vollmers [101] reviewed and compared various algorithms to detect vortices from experimentally obtained velocity fields (PIV). He confirmed that noisy or fluctuating data are best processed with methods that deal with a directly measured velocity field rather than with its gradients. One method that takes the integral flow behavior of the velocity field into account is the vortex identification method developed by Graftieaux et al. [30]. Two scalar functions Γ_1 and Γ_2 are derived directly from the velocity vector fields. According to Graftieaux, these scalars do not consider the vortex strength but rather the flow topology. This makes the method suitable to deal with discontinuities and also robust enough to handle big amounts of data. The method was successfully applied by Widmann [104] for a similar experimental setup and will be used in this study to identify vortex core positions and vortex boundaries. The scalar function Γ_1 and Γ_2 are mathematically defined as:

$$\Gamma_1(\text{P}) = \frac{1}{N} \sum_{n=1}^{N} \frac{\left(\overrightarrow{\text{PM}}_n \times U_{\text{M}_n}\right) \cdot z}{\left|\overrightarrow{\text{PM}}_n\right| \cdot |U_{\text{M}n}|} = \frac{1}{N} \sum_{n=1}^{N} \sin\left(\Theta_m\right) \tag{5.12}$$

$$\Gamma_2(\text{P}) = \frac{1}{N} \sum_{n=1}^{N} \frac{\left(\overrightarrow{\text{PM}}_n \times \left(U_{\text{M}_n} - \tilde{U}_{\text{P}}\right)\right) \cdot z}{\left|\overrightarrow{\text{PM}}_n\right| \cdot \left|U_{\text{M}_n} - \tilde{U}_{\text{P}}\right|} \tag{5.13}$$

P is the point in the vector field for that the scalar function is derived. P is located in the middle of a rectangular domain of N points. M_n is a point inside the considered rectangle and $\overrightarrow{PM_n}$ is the vector between P and M_n. Θ_m is the angle enclosed by $\overrightarrow{PM_n}$ and the local flow velocity $\vec{u}(M_n)$. For a circular vortex, Γ_1 takes its maximal value of $|\Gamma_1| = 1$ at the vortex center. $|\Gamma_2|$ equals $2/\pi$ at a point of pure shear, which serves to detect the vortex boundary. The algorithm is implemented in *Matlab*, based on a software file provided by Endrikat [24] and adopted to match the requirements of the experimental setup. The algorithm is optimized for circular vortices. In the experimental data vortices have various shapes. To efficiently detect vortex cores and boundaries, the typical values of $|\Gamma_1|$ and $|\Gamma_2|$ are adapted and the tracking of vortex cores in time is implemented. More information about the implementation and adaption of the vortex identification method can be found in Kehl [48].

5.3.3. Experimental Results

The qualitative observations are similar for all investigated parameter combinations and first a comparative **qualitative LEV evolution during one pitch cycle** on the rigid and the adaptive camber airfoil is given. The qualitative observations are quantified by deriving the normalized circulation of the coherent LEV with the vortex identification method given in section 5.3.2, p.121. This **quantitative LEV evolution during one pitch cycle** is presented for one selected parameter combination of reduced frequency k and Strouhal number Sr, which corresponds to the center of the parameter set of section 5.3.1, p.117. The pitch cycles of the remaining parameter combinations are processed in a similar manner and the **influence of reduced frequency and Strouhal number on the normalized circulation** is presented at the end of this subsection.

Qualitative LEV Evolution During one Pitch Cycle

Figure 5.15a shows the dynamic pitch angle of attack α_p over the dimensionless time t^+, which is obtained by normalization with the pitching period $T = 1/f_p$. Note that α_p is the geometric angle of attack enclosed by the main stream direction $U_\infty \vec{e}_x$ and the chordwise direction $\vec{x'}$ of the rigid reference airfoil. The pitch cycle begins at the minimum angle of attack of $\alpha_{p,min} = 8°$ ($t^+ = 0$). The airfoil pitches upwards to its

maximum angle of attack of $\alpha_{p,max} = 20°$ ($t^+ = 0.5$) and afterwards pitches down-wards to the minimum angle of attack ($t^+ = 1$). Coherent vortices are observed in the region highlighted in white. No coherent vortices are observed in gray colored regions. Points of interest are labeled from (a) to (e). The corresponding flow situations on the rigid and the adaptive airfoil are schematically visualized in Figure 5.16 and explained below.
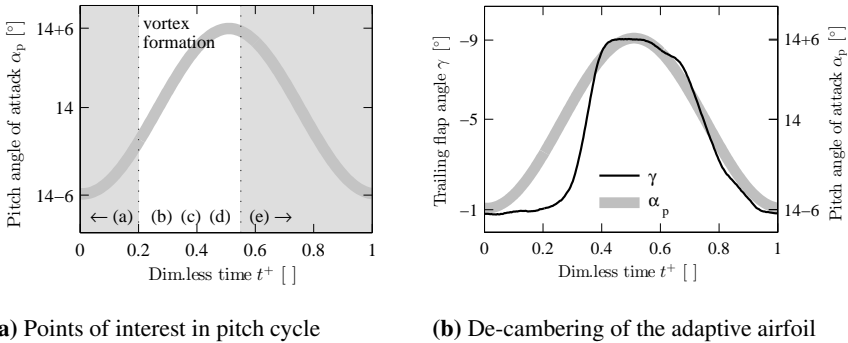

(a) Points of interest in pitch cycle

(b) De-cambering of the adaptive airfoil

Figure 5.15.: Evolution of the pitch angle of attack during one pitch cycle ($0 < t^+ = t/T < 1$). The airfoil pitches continuously around a mean angle of attack $\alpha_m = 14°$, with an amplitude $\hat{\alpha}_p = 6°$. The cycle starts at minimum angle of attack and follows a harmonic sinusoidal motion. (a): Important stages in the pitch cycle are labeled and described later. (b): De-cambering of the adaptive airfoil over one pitch-period, exemplary shown for $k = 0.1$ and $Sr = 0.066$, quantified by the trailing flap angle γ.

The flow structure on the **rigid airfoil** is similar to that observed by other authors (for example [15,16,69,71,85]) and resembles the typical vortex life cycle described in section 3.3.1. At the beginning of the upstroke at $t^+ = 0$, the angle of attack is small. The flow remains attached to the airfoil surface, which corresponds to (a). With increasing angle of attack, the shear layer starts to roll up into a coherent vortical structure at the front part of the airfoil, the so-called leading-edge vortex (LEV) (b). The LEV grows in size as it convects over the airfoil, with a velocity smaller than the main flow, staying close to the airfoil surface (c). At the aft part, the LEV interacts with a counter rotating trailing-edge vortex (d). The LEV is deflected from the airfoil surface and is drawn away by the outer flow. A new coherent LEV is formed at the leading-edge and a new vortex life cycle of formation, growth and convection
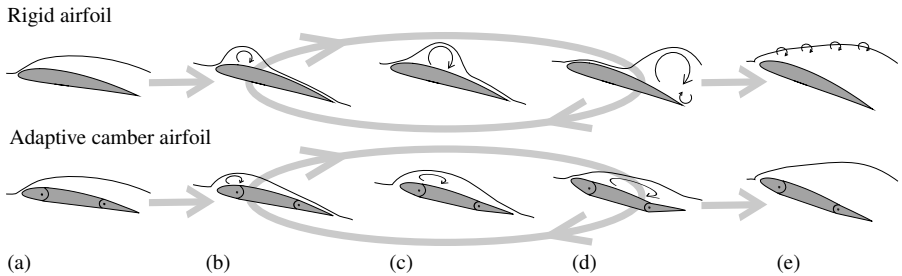
124

Rigid airfoil

Adaptive camber airfoil

(a)   (b)   (c)   (d)   (e)

Figure 5.16.: Schematic representation of the dynamic stall process on the rigid (top) and
the adaptive camber airfoil (bottom). During the pitch cycle, the rigid airfoil experiences
the flow phenomenon typically associated with dynamic stall: a cycle of formation of a
leading-edge vortex (b) growth and convection of the vortex over the airfoil (c), interaction
with the trailing-edge vortex and separation (d), followed by full stall, well behind the static
stall angle (e). The flow around the adaptive camber airfoil features smaller vortices (b-d),
while the airfoil de-cambers, followed by full stall (e).

begins. Stages (a), (b) and (c) are repeated two to three times during $0.15 < t^+ < 0.5$,
before the airfoil stalls completely at stage (e). The full stall persists during down-
stroke. Smaller vortices sprout in the shear layer between undisturbed mean flow and
the stalled region. This vortex layer moves closer to the airfoil as deep stall evolves
to light stall with decreasing angle of attack. The vortices in the vortex layer become
less distinct and the flow reattaches from the leading-edge as the airfoil passes its
minimum angle of attack. A new coherent LEV forms, and the cycle is repeated in
the next consecutive pitch cycle.

The **adaptive camber airfoil** de-cambers during the pitch cycle, as depicted in Fig-
ure 5.15b. At the beginning of the pitch cycle, the adaptive camber airfoil's shape is
close to the original Clark Y with a trailing flap angle of about $\gamma = -1°$. During the
first half of the upstroke, where the aerodynamic moment around the leading-edge
is not sufficient to effectively actuate the adaptive camber mechanism, the adaptive
camber airfoil's shape remains unchanged. Midway during upstroke, the adaptive
camber airfoil de-cambers to a trailing flap angle of $\gamma = -9°$. The adaptive camber
airfoil maintains its shape as the airfoil passes its maximum angle of attack and re-
turns to its original shape during downstroke, proportional to the airfoil pitch motion.
The de-cambering occurs at the phase in the pitch cycle during that vortex formation,

growth and convection take place on the rigid airfoil (stages (b)-(d)). On the adaptive camber airfoil, coherent LEVs with a rounded elliptical shape are formed that are generally smaller in size. This is in agreement with the findings of Rojratsirikul et al. and Visbal et al. [81,100] who investigated membrane airfoils mimicking insect wings. Those membrane airfoils have inverted kinematics, compared to the adaptive camber airfoil. The membrane wings' camber increases with increasing angle of attack, yielding an increased effective angle of attack and a stronger shear layer. This results in likewise stronger vortices and higher lift production compared to a rigid reference wing.

Quantitative LEV Evolution During one Pitch Cycle

The qualitative LEV evolution described above is similar for all parameter combinations. The qualitative observations are quantified by deriving the boundaries of the coherent LEV from the velocity vector fields with the vortex detection method of Graftieaux et al. [30] described in section 5.2.2. The circulation inside the coherent vortices is integrated and normalized to obtain $\Gamma^+(t^+)$ for every snapshot in time of the pitch cycle. From the time resolved Γ^+ evolution, mean, standard deviation and maximal values are derived to characterize each k-Sr combination. This procedure is exemplary shown for one parameter combination of $k = 0.1$ and $Sr = 0.066$ (i.e. the center point in the parameter space of Figure 5.13).

Figure 5.17 exemplary compares time resolved snapshots of the velocity field obtained from PIV data around the rigid (left) and the adaptive camber airfoil (right). Three instants in time $t^+ = 0.26, 0.30$ and 0.34 are chosen as they illustrate one cycle of vortex formation, growth and convection on the rigid airfoil. On both the rigid and the adaptive camber airfoil a coherent LEV is formed at $t^+ = 0.26$. This vortex is highlighted in blue for the rigid and in red for the adaptive camber airfoil. The same LEV is highlighted in the snapshots at $t^+ = 0.30$ and 0.34. On both the rigid and the adaptive camber airfoil, the LEV grows in time and its center propagates over the airfoil. The LEV on the rigid airfoil is generally larger than on the adaptive camber airfoil. Other coherent vortices, dating from a previous cycle of vortex formation, growth and propagation are detected in the snapshots at $t^+ = 0.26$ and 0.30.

The circulation of a coherent vortex is not necessarily proportional to its size but

126
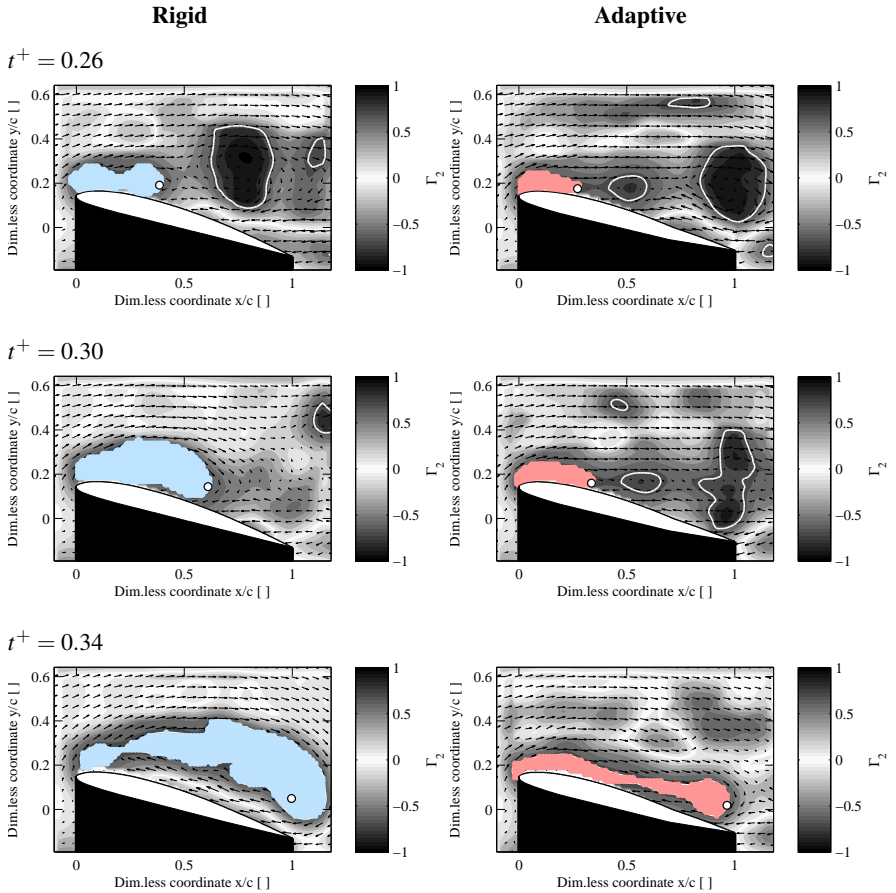
Figure 5.17.: Illustration of one vortex shedding cycle on the rigid airfoil (left) and the adaptive airfoil (right). Time resolved snapshots are taken at $t^+ = 0.26$, 0.30 and 0.34, corresponding to the stages of formation, growth and convection of the coherent LEV. The background is gray scale coded with Γ_2 values and overlaid with the local flow direction. Every third vector is plotted for clarity. Vortex center and boundary of the coherent LEVs are obtained by the vortex identification method of Graftieaux et al. [30] and highlighted in white. The coherent LEV formed at $t^+ = 0.26$ is highlighted in blue on the rigid and in red on the adaptive camber airfoil on all snapshots.

obtained by integrating the vorticity inside its boundaries, cf. section 5.3.2, p.121. Integrating the vorticity of all detected vortices of the vector field yields the total circulation Γ of all coherent LEVs for one snapshot in time. Normalization with the chord length c and the inflow velocity U_∞ results in the normalized circulation Γ^+

$$\Gamma^+ = \frac{\Gamma}{cU_\infty}. \tag{5.14}$$

Figure 5.18 shows Γ^+ as a function of t^+ for the rigid and the adaptive camber airfoil. Figure 5.18a shows the time resolved evolution over one complete pitch cycle. Figure 5.18b gives a close-up view of the vortex shedding region between $0.15 < t^+ < 0.5$. On the rigid airfoil, high variations of the normalized circulation Γ^+ are observed,
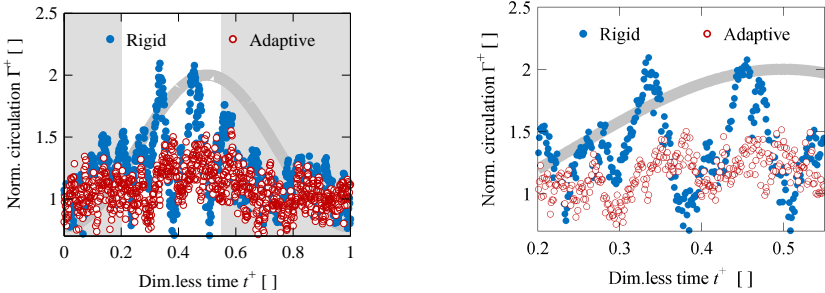
(a) Complete pitch cycle

(b) Vortex shedding region

Figure 5.18.: Normalized circulation Γ^+, obtained by integrating the vorticity of all identified coherent vortices for one snapshot and displayed over the dimensionless time t^+. The angle of attack evolution and the region of vortex shedding are highlighted in the background to provide orientation of the expected flow regime. For clarity, only every second value is displayed. (a) shows the complete pitch cycle. (b) gives a close up on the vortex shedding region between $0.15 < t^+ < 0.5$.

especially in the vortex shedding region. This is caused by the typical cycle of formation, growth and convection of large coherent structures, during which Γ^+ increases steadily. When the coherent structure reaches the airfoil's trailing-edge, it interacts with a counter rotating trailing-edge vortex and is shed. The coherent structure is convected downstream and leaves the field of view, Γ^+ decreases. A new cycle of formation, growth and convection begins that results in cyclic variations of Γ^+. On the

adaptive camber airfoil, the variation of Γ^+ is less pronounced. A total of four consecutive pitch cycles is evaluated. Macroscopically, an equivalent behavior is seen for each of the investigated pitch cycles: The rigid airfoil experiences vortex formation, growth and propagation. The adaptive camber airfoil de-cambers, accompanied by smaller and less coherent structures. The temporal occurrence of vortex formation, growth and propagation differs slightly from pitch cycle to pitch cycle. Mean and maximal values of Γ^+ as well as the standard deviation $\sigma(\Gamma^+)$ are given in Table 5.2 to quantify the repeatability of the events. Although dynamic stall is a highly turbulent phenomenon and the temporally resolved data exhibits a high variability, mean and maximum values as well as the standard deviation agree well from pitch cycle to pitch cycle. The qualitative observation that the de-cambering of the adaptive camber airfoil leads to weaker LEV has now been quantified. Figure 5.18 and Table 5.2 reveal the adaptive camber airfoil's potential for gust load alleviation under dynamic stall conditions. Mean and maximal values and the standard deviation of the Γ^+ are smaller on the adaptive camber airfoil, compared to the rigid reference airfoil. In section 4.3.3, p. 67, the load reduction LR is defined to be the relative difference in standard deviation of the fluctuating loads on adaptive and rigid airfoil. LR serves as a measure for the adaptive camber airfoil's effectiveness in terms of gust load alleviation: for $LR = 1$, all load fluctuations are alleviated by the adaptive camber airfoil. For $LR = 0$, the adaptive camber and the rigid airfoil exhibit equally fluctuating loads and for $LR < 0$, fluctuating loads are enhanced by the adaptive camber airfoil. In a

Table 5.2.: Mean and maximal values as well as the standard deviation of the normalized circulation Γ^+ during all investigated pitch cycles.

Pitch cycle	$\overline{\Gamma^+}$		Γ^+_{max}		$\sigma(\Gamma^+)$	
	rigid	adaptive	rigid	adaptive	rigid	adaptive
1	1.21	1.07	2.09	1.55	0.27	0.16
2	1.18	1.08	2.15	1.62	0.26	0.18
3	1.20	1.10	2.02	1.61	0.23	0.17
4	1.25	1.10	2.13	1.62	0.22	0.17

similar manner to *LR*, the circulation reduction *CR* is defined as

$$CR = \frac{\sigma(\Gamma^+_{rigid}) - \sigma(\Gamma^+_{adaptive})}{\sigma(\Gamma^+_{rigid})} \tag{5.15}$$

For the values of $\sigma(\Gamma^+_{rigid})$ and $\sigma(\Gamma^+_{adaptive})$ given in Table 5.2, the circulation reduction calculates to $CR = 0.32$ signifying that 32 % of the fluctuating circulation is alleviated by the adaptive camber airfoil. It can be anticipated that fluctuating loads are also damped, as Jones and Babinsky [44] found the circulation of coherent LEV to be directly proportional to the exhibited load. This is a good result in terms of gust load alleviation. Another favorable result in terms of fatigue is the decreased mean value of $\overline{\Gamma^+}$ on the adaptive camber airfoil. Below rated wind speed and in attached flow regime, a high mean lift is favorable regarding the energy harvest of the wind turbine. Above rated wind speed and at conditions where dynamic stall typically occurs, high mean loads do not further increase energy harvest but have an increased contribution to fatigue life.
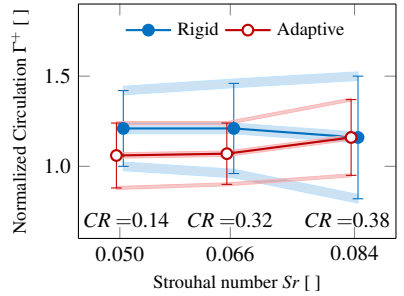
Influence of the Reduced Frequency and the Strouhal Number on the Normalized Circulation

An equivalent investigation is carried out for all Strouhal number *Sr* and reduced frequency *k* combinations of Figure 5.13, p.119. The results are displayed in Figure 5.19. Mean values $\overline{\Gamma^+}$ are represented by marker symbols and the standard deviation $\sigma(\Gamma^+)$ by error bars. The circulation reduction *CR* is indicated for each parameter combination. Figure 5.19a shows values for the variation of *k*, obtained from parameter set ①. Figure 5.19b shows values for the variation of *Sr*, obtained from parameter set ②. Generally, mean values $\overline{\Gamma^+}$ and standard deviation $\sigma(\Gamma^+)$ of the normalized circulation are smaller on the adaptive camber airfoil, compared to the corresponding values on the rigid airfoil. The circulation reduction *CR* takes values between $0.14 < CR < 0.38$, meaning that the adaptive camber airfoil reduces fluctuating circulation between 14 % and 38 %. The adaptive camber airfoil exhibits also smaller mean circulation $\overline{\Gamma^+}$ for all investigated *k-Sr* combinations.

The maximal circulation accumulated in a LEV vortex Γ^+_{max} is mainly determined by the feeding shear layer properties, if LEV detachment is initiated by bluff body mechanism as reported by Widmann and Tropea [104]. For a rigid airfoil, Γ^+_{max}
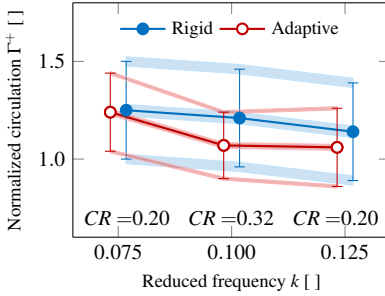
(a) Parameter set ①, $Sr = 0.066$

(b) Parameter set ②, $k = 0.1$

Figure 5.19.: Mean and standard deviation of the normalized circulation Γ^+ on the rigid and the adaptive camber airfoil. (a) shows the dependence on the reduced frequency k at constant Sr, (b) shows the dependence on the Strouhal number Sr at constant k. Mean values $\overline{\Gamma^+}$ are represented by marker symbols and standard deviation $\sigma(\Gamma^+)$ is represented by error bars. Uncertainty intervals due to the stochastic nature of dynamic stall are obtained according to the guidelines of GUM Type A [43] from consecutive measurements of the same parameter combination, as listed in table 5.2 and represented by colored regions. The displayed values are dispersed for better visibility, but are obtained at the indicated parameters.

depends then mainly on the reduced frequency k and the Strouhal number Sr of the airfoil oscillation. Baik et al. [5] found maximal values of $\Gamma^+_{\max}$ on a pitching and plunging flat plate to increase with increasing Strouhal number in the range of $0.1 < Sr < 0.48$ and to decrease with increasing k in the range of $0.31 < k < 0.63$. A similar behavior was observed by Widmann and Tropea [105] for $0.24 < k < 0.48$ in a comparable experimental setup. For the rigid airfoil, the evolution of $\Gamma^+_{\max}$ is proportional to $\overline{\Gamma^+} + \sigma(\Gamma^+)$ (i.e. the topmost line in Figure 5.19). The experimental values agree with the findings of Baik et al. [5] and Widmann and Tropea [105] in terms of k and Sr. On the adaptive camber airfoil, the evolution of Γ^+ is not only influenced by Sr and k but also by its de-cambering.

The trailing flap angle γ serves as a measure for the adaptive camber airfoil de-cambering and is displayed over the dimensionless time t^+ for all investigated parameter combinations in Figure 5.20. In Figure 5.20a the Strouhal number is held constant at $Sr = 0.066$ and the reduced frequency k is varied (parameter set ①). In Figure 5.20b k is held constant at $k = 0.1$ and the Sr is varied (parameter set ②).
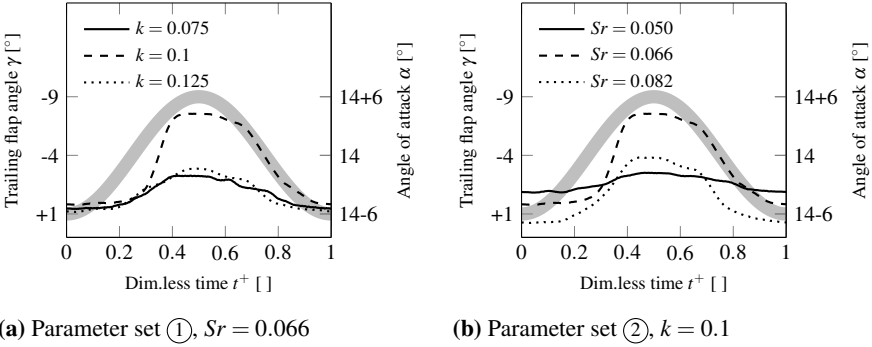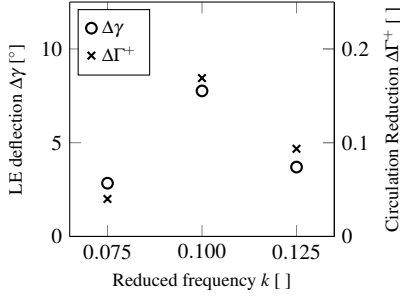
(a) Parameter set ①, $Sr = 0.066$

(b) Parameter set ②, $k = 0.1$

Figure 5.20.: Trailing flap angle γ as a measure for the de-cambering of the adaptive camber airfoil for the investigated parameters of set ① (left) and ② (right), displayed over the dimensionless time t^+. The original Clark Y profile corresponds to $\gamma = 0°$. Negative γ values correspond to an increased camber (flaps down), positive γ to a decreased camber (flaps up). The angle of attack α is plotted in the background and provides orientation of the position in the pitch cycle.

The evolution of γ is similar for all investigated parameter combinations. At the beginning of the upstroke, the adaptive camber airfoil's shape resembles the original Clark Y profile ($\gamma = 0°$). γ remains unchanged until midway through the upstroke at $t^+ \approx 0.25$. γ increases until the pitch motion is inverted at $t^+ = 0.5$. As the angle of attack α decreases for $t^+ \geq 0.5$, γ decreases proportionally to α. The trailing flap deflection during one pitch cycle $\Delta\gamma = \gamma_{max} - \gamma_{min}$ depends largely on the Sr-k combination. While in attached flow regime, the motion response increases with increasing k according to a power law and depends linearly on Sr, no distinct relationship is observed between $\Delta\gamma$ and k or $\Delta\gamma$ and Sr under detached flow conditions. At medium $k = 0.1$ and medium $Sr = 0.066$, the airfoil de-cambers most. The suspected influence of the de-cambering on the LEV evolution is discussed in section 5.3.1, p. 117. It is supposed that the rotation of the leading-edge alters the feeding shear layer due to the no-slip boundary condition on the airfoil surface and that the difference of circulation on rigid and adaptive camber airfoil $\Gamma^+_{max,rigid} - \Gamma^+_{max,adaptive}$ should scale with the adaptive camber airfoil's de-cambering, i.e. its effective angle of attack. Figure 5.21 shows $\Delta\gamma$ for parameter set ① and parameter set ②, together
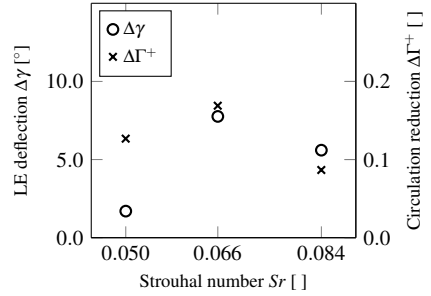
(a) Parameter set ①, $Sr = 0.066$ **(b)** Parameter set ②, $k = 0.1$

Figure 5.21.: Trailing flap deflection $\Delta\gamma$ of the adaptive camber airfoil and the relative reduction of the fluctuating circulation $\Delta\Gamma^+$ for all investigated parameter combinations.

with the normalized difference of maximal circulation $\Delta\Gamma^+$

$$\Delta\Gamma^+ = \frac{\Gamma^+_{\text{max,rigid}} - \Gamma^+_{\text{max,adaptive}}}{\Gamma^+_{\text{max,rigid}}} \qquad (5.16)$$

$\Delta\gamma$ and $\Delta\Gamma^+$ show a similar dependence on the reduced frequency k and the Strouhal number Sr. This confirms the assumption that maximal LEV circulation is reduced due to a weakening of the feeding shear layer by an upward rotation of the leading-edge.

Conclusions

The rigid airfoil passes through the cycle of LEV formation, growth, convection and detachment typically associated with dynamic stall. This is accompanied by high mean and fluctuating values of the normalized circulation. The adaptive camber airfoil de-cambers during the phase of vortex formation. Compared to the rigid reference airfoil,

- smaller and less stable LEV are observed on the adaptive camber airfoil.

The observations are quantified by the normalized circulation Γ^+:

- Reductions in the fluctuating normalized circulation $\sigma(\Gamma^+)$ of up to 38 % are observed.

133

Since the normalized circulation is directly proportional to the unsteady lift (see Jones and Babinsky [44]), this is a very favorable result in terms of gust load alleviation.

It is shown in section 4.4.1, p.69 that a distinct relation between the Strouhal number Sr, the reduced frequency k and the adaptive camber airfoil's trailing flap deflection $\widehat{\gamma}$ exists in attached flow regime. A different behavior is observed under detached flow conditions:

- No distinct relation between the reduced frequency k or Strouhal number Sr and the flap deflection γ is observed.

The accumulated circulation in the LEV formed during dynamic stall originates from the feeding shear layer.

- $\sigma(\Gamma^+)$, and hence the fluctuating loads, are more effectively damped for high flap deflections.

This is in good agreement with the findings during attached flow regime, cf. section 4.4.3, p.89, where the manipulation of fluctuating loads is shown to scale with the flap deflection $\widehat{\gamma}$. It was shown by Widmann and Tropea [104] that maximal LEV circulation is determined by the feeding shear layer strength. Comparing the normalized circulation on the rigid and the adaptive camber airfoil for otherwise equal conditions confirms this finding:

- $\Gamma^+_{\text{max,rigid}} - \Gamma^+_{\text{max,adaptive}}$ scales with the weakening of the shear layer due to the upwards rotation of the leading-edge.

Although intentionally designed to operate efficiently in attached flow conditions, the adaptive camber airfoil proves to alleviate fluctuating loads also in the detached flow regime. The reduction of fluctuating loads is accompanied by a reduction of the mean loading, which is especially favorable when considering fatigue.
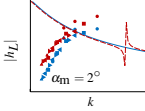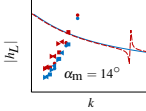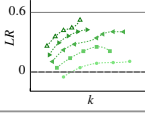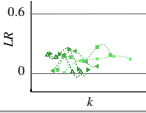
6. Summary, Conclusions and Outlook

6.1. Summary

In this thesis a rigid and an adaptive camber airfoil were investigated experimentally under unsteady conditions. The adaptive camber airfoil was developed at TU Darmstadt [38] in a preceding study and consists of a mechanically coupled leading and trailing flap. The concept entails strong fluid structure interaction, where flow conditions at the leading-edge provoke a change of camber through a combined deflection of leading-edge and trailing flap. Under quasi-steady conditions Lambie [57] showed that the adaptive camber airfoil exhibits a decreased lift curve slope. This could be beneficial in terms of gust load alleviation on wind turbines, as a gust expresses itself mainly through a change of angle of attack on the blade section. Gusts are by definition unsteady phenomena and unsteady aerodynamics are known to differ substantially from steady aerodynamics. To provide proof of concept of the adaptive camber airfoil regarding gust load alleviation under unsteady conditions, a systematic experimental study was carried out. Flow conditions typically encountered by wind turbine blades were approximated by generic inflow cases on a two-dimensional airfoil and tested in different wind tunnel experiments. The passage of the wind turbine blade through a horizontal velocity deficit was modeled by a sinusoidal vertical gust. Blade flapping and twisting were modeled by an oscillatory movement of the airfoil. A wind turbine blade encounters a wide spectrum of unsteady inflow conditions, described in dimensionless form by the reduced frequency k and the Strouhal number Sr, which can occur at various mean angles of attack. An extensive parameter study was performed to characterize influence of all parameters on the rigid and the adaptive camber airfoil's dynamic load response. The performance of the adaptive camber airfoil in terms of gust load alleviation was assessed by comparing the dynamic load responses of the rigid and the adaptive camber airfoil. The main findings of the performed experiments are schematically visualized in Figure 6.1.

	attached		detached	
Chapter 4: Sinusoidal vertical gust encounter - Sears Problem				
individual dyn. response	$|h_L|$; $\alpha_m = 2°$; k	inverse k-dependence	$|h_L|$; $\alpha_m = 14°$; k	similar quantitative behavior
load reduction	LR; 0.6; 0; k	up to 60% reduction of fluctuating loads	LR; 0.6; 0; k	no load enhanement, no correlation

	attached		detached	
Chapter 5: Oscillating airfoil - Theodorsen Problem				
individual dyn. response	$|h_{\Delta C_p}|$; $\alpha_m = 8°$; k	k-dependence agrees for zero lift angle	Γ^+; rigid; t	upward rotation of LE flap suppresses LEV generation
load reduction	$|h_{\Delta C_p}|$; 0.5; 0; rigid; adaptive; k	almost complete attenuation	$\Gamma^+ + \sigma(\Gamma^+)$; rigid; adaptive; Sr	circulation reduction $0.14 < CR < 0.38$
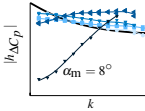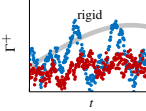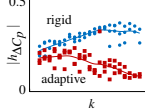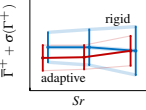
Figure 6.1.: Schematic overview of the obtained experimental results.

From the results of the performed experimental investigation, the initial question:

Does the adaptive camber airfoil alleviate gust loads under unsteady conditions?
can clearly be answered with 'Yes'. The adaptive camber airfoil was developed to
operate efficiently under attached flow conditions. Submitted to a sinusoidal vertical
gust, the adaptive camber airfoil alleviated up to 60 % of the gust loading at small
($\alpha_m = 2°$) and moderate ($\alpha_m = 8°$) mean angles of attack. Gust load reduction was

- unaffected by the gust amplitude $\widehat{\alpha}_g$,

- increased with decreasing system stiffness κ,
- increased with increasing reduced frequency k and
- was proportional to the trailing flap deflection γ.

At high angles of attack ($\alpha_m = 14\,^\circ$), the physical mechanisms of lift generation under unsteady conditions change. Gust load reduction of up to 30 % was achieved, but no distinct correlation between $\widehat{\alpha}_g$, κ, k, γ and the gust load reduction performance was observed. This gave rise to the question:

How does the adaptive camber airfoil alleviate gust loads?

To understand the behavior of the adaptive camber airfoil under **high mean angles of attack** the flow field was studied by means of time resolved particle image velocimetry (TR PIV). Dynamic stall conditions were provoked by pitching the airfoil dynamically around a high mean angle of attack ($\alpha_m = 14\,^\circ$). Coherent leading-edge vortices (LEV), believed to be responsible for high force excursions experienced by rigid airfoils during dynamic stall, were identified from the velocity field data. LEV were efficiently suppressed by the adaptive camber airfoil. This was attributed to the upwards rotation of the leading-edge, which changes the effective angle of attack and thereby alters the properties of the feeding shear layer. Maximal circulation on the rigid and the adaptive airfoil were compared for the same k and Sr combination. The difference in maximal circulation on the rigid and the adaptive camber airfoil scaled with the difference in effective angle of attack on both airfoils. The results support the statement of Widmann and Tropea [104] that shear layer properties, mainly influenced by the effective angle of attack, define the maximal circulation of LEVs.

At **small mean angles of attack**, the frequency dependent unsteady airfoil response is pressure driven and conveniently described by transfer functions. A comparison of first-order transfer functions with the experimentally derived individual airfoil response showed a significant deviation in the dependence on the reduced frequency. This was not only observed for the adaptive camber airfoil, but also for the rigid airfoil and led to the question:

Why is the individual airfoil response not captured by first-order theory?

A thorough literature research yielded that most first-order transfer functions lack a systematic experimental validation. This is somehow surprising given the wide ap-

plication of first-order transfer functions in the engineering community. In the case of the oscillating airfoil, which is described by the Theodorsen function, some experimental investigations have been carried out. The studies poorly support the theoretical Theodorsen function. Also the agreement between the individual studies is poor. To the authors best knowledge, no systematic experimental investigation of the sinusoidal gust encounter, i.e. the Sears problem, exists. This might be due to the fact that the experimental generation of two-dimensional sinusoidal vertical gusts is challenging. The only experimental study on the aerodynamic response to sinusoidal vertical gusts was performed in the context of civil engineering on an asymmetric bridge deck by Hatakana and Tanaka [33]. The lift response of the bridge deck showed a very similar behavior to the observations made during this study: The dynamic lift amplitude increased with reduced frequency k from a quasi-steady value smaller than one, while the Sears function predicts a decrease from the quasi-steady value of one. This implies on the one hand a faulty scaling, as experimental and theoretical transfer functions approach a different quasi-steady value and on the other hand a non satisfactory mathematical description, as the frequency dependence is not captured. First-order transfer functions assume an undisturbed constant velocity field with undistorted streamlines. The presence of a lift producing object violates these assumptions. Both, the asymmetric bridge deck and the airfoil investigated in this study (Clark Y airfoil at $\alpha_m = 2°$) produce a mean lift. The literature review on the Theodorsen problem yielded that most experimental results agree better with theory if the oscillation is applied around small mean angles of attack where no or very small mean lift is produced. This led to the assumption that the production of a mean lift might be responsible for the discrepancies between experimental results and first-order transfer functions. The assumption was tested on a sinusoidally pitching airfoil. The pressure difference at the airfoil's leading-edge was compared to a corresponding first-order transfer function of the pressure, given by Mateescu and Abdo[68]: For an oscillation around a mean angle of attack that generates zero pressure difference under quasi-steady conditions, experimental results agreed well with first-order transfer functions. With increasing mean angle of attack and increasing mean pressure difference, a deviation between experimental and theoretical values in terms of reduced frequency dependence and scaling was observed. At $\alpha_m = 5°$ and $\alpha_m = 8°$, an inversion of the frequency dependence was seen: The magnitude of

the experimental transfer function increased from a quasi-steady value smaller than one, while theory predicts a decrease from the quasi-steady value of one. This resembles the behavior of the load response observed for the sinusoidal vertical gust encounter.

6.2. Conclusions and Outlook

First-order transfer functions have to be applied with caution. In engineering applications it is rarely the objective to produce zero mean lift. The oscillating airfoil seemed to be less sensitive for a violation of the zero mean lift assumption: Significant differences between theory and experimental results were observed for $\alpha_m \geq 5°$, while the airfoil encountering a sinusoidal vertical gust was not captured by theory for mean angles as small as $\alpha_m = 2°$. Although the results indicate that the production of mean lift is responsible for the deviation between theory and experimental results, this assumption was not verified for the sinusoidal vertical gust encounter. The experimental verification of the Sears function for a symmetric airfoil at various α_m could provide useful guidelines for the limits of its applicability.

The evaluation in terms of gust load alleviation is uninfluenced by the disagreement between experimental and theoretical individual airfoil response. Both the rigid and the adaptive camber airfoil's behavior deviate in a similar manner from theoretical predictions. If a theory is found that describes the reduced frequency dependence of the unsteady load response of rigid airfoils adequately, the adaptive camber airfoil should be representable by the same means. In the present experimental study it was shown that the adaptive camber airfoil's performance in terms of gust load alleviation is comparable to active systems, while retaining all the advantages already pointed out by Lambie [57]: The passive nature of the adaptive camber concept makes it more robust to implement, as no sensors, actuators or control schemes are needed. The restraining spring system can be configured in such a way that the airfoil produces higher mean lift at low aerodynamic loading, which could increase energy harvesting at wind speeds below rated speed. At the same time, the mean lift is decreased for high aerodynamic loading, which could be beneficial in limiting maximal loading and fatigue. This encourages further investigation of the adaptive

camber system: The current study was performed at low Reynolds numbers under two-dimensional unsteady flow conditions, exciting isolated degrees of freedom underneath their resonance frequency. Before submitting the adaptive camber airfoil to real world operating conditions on wind turbines, some additional points should be considered:

Two-dimensional aerodynamic investigations
The current experimental investigations were carried out at relatively low Reynolds numbers ($Re \approx 200.000$), which is an order of magnitude smaller than the Reynolds number encountered by blade sections on the outer rotor position of multi-megawatt turbines. On this part of the rotor the Mach number threshold of $M = 0.3$ that commonly distinguishes incompressible from compressible flow description is scratched. In incompressible attached flow described by first-order transfer functions, the influence of the Reynolds number is usually neglected. It was shown in the current experimental investigation that the limits of applicability of first-order transfer functions might be narrower than it is commonly assumed. An experimental two-dimensional investigation at higher Reynolds numbers should be carried out.
As it was pointed out by Spiegelberg [88], the placement of the system's eigenfrequencies plays a crucial role in the performance of the adaptive camber airfoil. In this study only excitation frequencies below the system's eigenfrequency were investigated, due to limitations of the active grid and the pitch-plunge rig. Even with a thorough design it can never be completely excluded that the adaptive camber airfoil encounters excitation frequencies close to its resonance and an investigation at these operating conditions should be performed.

Two-dimensional aero-elastic investigations
Besides investigating the resonance of one isolated degree of freedom, the interaction between different degrees of freedom should be examined. When energy is shifted from one oscillatory degree of freedom to another, an aeroelastic phenomenon called flutter can occur. Flutter exists between two airfoil degrees of freedom (i.e. plunge and pitch) but also for example between the plunging motion of an airfoil and the rotational oscillation of its trailing flap. An experimental aeroelastic investigation of the adaptive camber airfoil's flapping degree of freedom should be carried out, es-

pecially when considering that state of the art flutter calculations build on the Sears function.

Rotating frame aerodynamic investigations

The current experimental investigation approximates flow conditions on a rotating blade by a two-dimensional airfoil section, submitted to two-dimensional perturbations. In the rotating reference frame, additional fictitious aerodynamic forces due to rotation occur: The centrifugal force is directed in radial direction and points from the nacelle to the blade tip. The Coriolis force accelerates the fluid from leading to trailing flap and in direction of the nacelle. The induced cross flow leads to a perceived diminution of the blade thickness. The influence of these additional forces on the adaptive camber airfoil's working principle as well as inertial forces due to the rotation on the flap system have to be investigated.

System integration

It was shown on the plunging adaptive camber airfoil that mass inertia effects enhance the adaptive camber airfoil's working principle up to a point of complete attenuation of fluctuating aerodynamic loads. On a wind turbine blade in bending oscillation, which is the corresponding three dimensional scenario, aerodynamic loads induce positive aerodynamic damping. If all aerodynamic damping forces are alleviated, all kinetic energy has to be absorbed by structural damping. To which extent this fact reduces the benefits of gust load alleviation in terms of fatigue and to which extend the working principle of the adaptive camber airfoil suppresses bending oscillations a priori could be studied in a numeric aeroelastic investigation.

The adaptive camber mechanism changes the aerodynamic properties of the airfoil, while the aerodynamic properties of a rigid airfoil remain constant over time. State of the art wind turbines possess complicated control systems that are optimized for rigid rotor blades. If the wind turbine blade alters its aerodynamic performance according to different inflow conditions, control schemes have to be adapted. Pitch control for example aims to increase the blades load pick up below rated speed and keep it constant above rated speed. Depending on the configuration of the restraining spring system, the adaptive camber airfoil has the same effect. The interaction between pitch control and a wind turbine blade with variable aerodynamic properties

could be an interesting application for developers of control schemes.

Although there remains much work to be done, this study presents an important milestone on the road from the idea of the adaptive camber airfoil to an installation on commercial wind turbines. The experimental results are promising and encourage further investigations of the adaptive camber airfoil as a robust and highly effective gust load alleviation device.

Bibliography

[1] J. Akkala. *Understanding and controlling vorticity transport in unsteady, separated flows*. PhD thesis, University of Iowa, 2015.

[2] P. B. Andersen, M. Gaunaa, C. Bak, and M. H. Hansen. A dynamic stall model for airfoils with deformable trailing edges. *Wind Energy*, 12(8):734–751, 2009.

[3] P. B. Andersen, L. Henriksen, M. Gaunaa, C. Bak, and T. Buhl. Deformable trailing edge flaps for modern megawatt wind turbine controllers using strain gauge sensors. *Wind Energy*, 13(2-3):193–206, 2010.

[4] H. Atassi. The Sears problem for a lifting airfoil revisited-new results. *Journal of Fluid Mechanics*, 141:109–122, 1984.

[5] Y. S. Baik, L. P. Bernal, K. Granlund, and M. V. Ol. Unsteady force generation and vortex dynamics of pitching and plunging aerofoils. *Journal of Fluid Mechanics*, 709:37–68, 2012.

[6] C. Bak, M. Gaunaa, P. B. Andersen, T. Buhl, P. Hansen, K. Clemmensen, and R. Moeller. Wind tunnel test on wind turbine airfoil with adaptive trailing edge geometry. In *45th AIAA Aerospace Sciences Meeting and Exhibit*, page 1016, 2007.

[7] S. Barbarino, O. Bilgen, R. M. Ajaj, M. I. Friswell, and D. J. Inman. A review of morphing aircraft. *Journal of Intelligent Material Systems and Structures*, 22(9):823–877, 2011.

[8] T. K. Barlas and G. van Kuik. Review of state of the art in smart rotor control research for wind turbines. *Progress in Aerospace Sciences*, 46(1):1–27, 2010.

[9] L. Bergami and M. Gaunaa. Analysis of aeroelastic loads and their contributions to fatigue damage. In *Journal of Physics: Conference Series*, volume 555, page 012007. IOP Publishing, 2014.

[10] D. D.-I. A. Betz. *Wind-Energie und ihre Ausnutzung durch Windmühlen*. Vandenhoeck & Ruprecht, 1926.

[11] F. Boettcher, C. Renner, H.-P. Waldl, and J. Peinke. On the statistics of wind gusts. *Boundary-Layer Meteorology*, 108(1):163–173, 2003.

[12] J. B. Bratt. The effect of mean incidence, amplitude of oscillation, profile and aspect ratio on pitching moment derivatives. *Reports and Memoranda*, 2064:2299–2348, 1945.

[13] J. Brötz. Konstruktion eines Flügelprofils mit adaptivem Wölbmechanismus. Bsc. Thesis, FG SLA, TU Darmstadt, 2014.

[14] T. Burton, D. Sharpe, N. Jenkins, and E. Bossanyi. *Wind Energy Handbook*. John Wiley & Sons, 2001.

[15] L. W. Carr, K. W. McAlister, and W. J. McCroskey. Analysis of the development of dynamic stall based on oscillating airfoil experiments. Technical report, NASA Ames Research Center, 1977.

[16] L. W. Carr, W. J. McCroskey, and K. W. McAlister. Dynamic stall experiments on the NACA 0012 airfoil. Technical report, NASA Ames Research Center, 1978.

[17] T. Cebeci, M. Platzer, H. Chen, K.-C. Chang, and J. P. Shao. Analysis of low-speed unsteady airfoil flows. *Long Beach, CA: Horizons Publishing Inc, 2005. 226*, 2005.

[18] G. Commerford and F. Carta. An exploratory investigation of the unsteady aerodynamic response of a two-dimensional airfoil at high reduced frequency. In *American Institute of Aeronautics and Astronautics, Dynamics Specialists Conference, Williamsburg, VA*, page 1973, 1973.

144

[19] J. R. Connell. Turbulence spectrum observed by a fast-rotating wind-turbine blade. Technical report, Battelle Pacific Northwest Labs., Richland, WA (USA), 1980.

[20] S. S. Davis and G. N. Malcolm. Transonic shock-wave/boundary-layer interactions on an oscillating airfoil. *AIAA Journal*, 18(11):1306–1312, 1980.

[21] T. Doligalski, C. Smith, and J. Walker. Vortex interactions with walls. *Annual Review of Fluid Mechanics*, 26(1):573–616, 1994.

[22] E. H. Dowell and K. C. Hall. Modeling of fluid-structure interaction. *Annual Review of Fluid Mechanics*, 33(1):445–490, 2001.

[23] J. A. Ekaterinaris and M. F. Platzer. Computational prediction of airfoil dynamic stall. *Progress in Aerospace Sciences*, 33(11):759–846, 1998.

[24] S. Endrikat. Find vortices in velocity fields, idvortex. http://www.mathworks.com/matlabcentral/fileexchange/52343-find-vortices-in-velocity-fields/content/IDvortex.m, 2015.

[25] I. E. Garrick. On some reciprocal relations in the theory of nonstationary flows. *NACA Tech Rept. 629*, 1938.

[26] M. Gaunaa. Unsteady two-dimensional potential-flow model for thin variable geometry airfoils. *Wind Energy*, 13(2-3):167–192, 2010.

[27] M. Gaunaa and P. B. Andersen. Load reduction using pressure difference on airfoil for control of trailing edge flaps. In *2009 European Wind Energy Conference and Exhibition*, 2009.

[28] M. Gharib, E. Rambod, and K. Shariff. A universal time scale for vortex ring formation. *Journal of Fluid Mechanics*, 360:121–140, 1998.

[29] M. E. Goldstein and H. Atassi. A complete second-order theory for the unsteady flow about an airfoil due to a periodic gust. *Journal of Fluid Mechanics*, 74(04):741–765, 1976.

[30] L. Graftieaux, M. Michard, and N. Grosjean. Combining PIV, POD and vortex identification algorithms for the study of unsteady turbulent swirling flows. *Measurement Science and Technology*, 12(9):1422, 2001.

[31] R. L. Halfman. Experimental aerodynamic derivatives of a sinusoidally oscillating airfoil in two-dimensional flow. *NACA Tech Rept. 1108*, 1952.

[32] M. H. Hansen, M. Gaunaa, and H. Aagaard Madsen. A Beddoes-Leishman type dynamic stall model in state-space and indicial formulations. *R-1354 (EN), Risø National Laboratory*, 2004.

[33] A. Hatanaka and H. Tanaka. New estimation method of aerodynamic admittance function. *Journal of Wind Engineering and Industrial Aerodynamics*, 90(12):2073–2086, 2002.

[34] E. Hau. *Windkraftanlagen: Grundlagen, Technik, Einsatz, Wirtschaftlichkeit*. Springer-Verlag, 2014.

[35] D. H. Hodges and G. A. Pierce. *Introduction to Structural Dynamics and Aeroelasticity*, volume 15. Cambridge University Press, 2011.

[36] J. Holierhoek, J. De Vaal, A. van Zuijlen, and H. Bijl. Comparing different dynamic stall models. *Wind Energy*, 16(1):139–158, 2013.

[37] J. Horlock. Fluctuating lift forces on aerofoils moving through transverse and chordwise gusts. *Journal of Basic Engineering*, 90(4):494–500, 1968.

[38] K. Hufnagel and B. Lambie. Erfindungen betreffend Rotorblätter, insbesondere für Windkraftanlagen, EP 2569535 A2, 2013.

[39] IEC. IEC 614 0001 Edition 3, Wind turbines part 3: Design requirements. Technical report, International Electrotechnical Commission, May 2003.

[40] L. Jäger. Modellierung und Kopplung Instationärer Profilanströmung mit einem Panelverfahren. Bsc. Thesis, FG SLA, TU Darmstadt.

[41] C. O. Johnston. Review, extension, and application of unsteady thin airfoil theory. *CIMSS Report*, pages 04–101, 2004.

[42] C. O. Johnston, W. H. Mason, and C. Han. Unsteady thin airfoil theory revisited for a general deforming airfoil. *Journal of Mechanical Science and Technology*, 24(12):2451–2460, 2010.

[43] Joint Committee for Guides in Metrology. Evaluation of measurement data - guide to the expression of uncertainty in measurement. Technical report, JCGM, 2008.

[44] A. Jones and H. Babinsky. Unsteady lift generation on rotating wings at low Reynolds numbers. *Journal of Aircraft*, 47(3):1013–1021, 2010.

[45] J. M. Jonkman, S. Butterfield, W. Musial, and G. Scott. Definition of a 5-MW reference wind turbine for offshore system development. Technical report, National Renewable Energy Laboratory, 2009.

[46] J. Katz and A. Plotkin. *Low-Speed Aerodynamics*, volume 13. Cambridge University Press, 2010.

[47] R. Katzmayr. Effect of periodic changes of angle of attack on behavior of airfoils. *Zeitschrift für Flugtechnik und Motorluftschifffahrt*, 1922.

[48] T. Kehl. Visualisierung instationärer Strömung um ein adaptives Flügelprofil für Windenergieanlagen. Master's thesis, FG SLA, TU Darmstadt, 2016.

[49] V. Kitsios, R. Kotapati, R. Mittal, A. Ooi, J. Soria, and D. You. Numerical simulation of lift enhancement on a NACA 0015 airfoil using znmf jets. In *Proceedings of the Summer Program*, page 457. Citeseer, 2006.

[50] M. Klyk. Konstruktion und Inbetriebnahme eines flexiblen Flügelprofils für Dynamic Stall Versuche. Bsc. Thesis, FG SLA, TU Darmstadt.

[51] P. Knebel, A. Kittel, and J. Peinke. Atmospheric wind field conditions generated by active grids. *Experiments in Fluids*, 51:471–481, 2011.

[52] R. Knoller. Zur Theorie des Segelfluges. *Zeitschrift für Flugtechnik und Motorluftschiffahrt*, 4:13–14, 1913.

[53] V. Kolar. Brief notes on vortex identification. *Recent Advances in Fluid Mechanics, Heat & Mass Transfer and Biology WSEAS*, 2007.

[54] M. Kramer. Increase in the maximum lift of an airplane wing due to a sudden increase in its effective angle of attack resulting from a gust. *Zeitschrift für Flugtechnik und Motorluftschiffahrt*, Vol. 23(7):185–189, 1932.

[55] R. Kubin and A. Fletcher. Fluorescence quantum yields of some rhodamine dyes. *Journal of Luminescence*, 27(4):455 – 462, 1983.

[56] H. G. Küssner. Zusammenfassender Bericht über den instationären Auftrieb von Flügeln. *Luftfahrtforschung*, 13(12):410–424, 1936.

[57] B. Lambie. *Aeroelastic Investigation of a Wind Turbine Airfoil with Self-Adaptive Camber*. PhD thesis, TU Darmstadt, 2011.

[58] G. Larose. Experimental determination of the aerodynamic admittance of a bridge deck segment. *Journal of Fluids and Structures*, 13(7):1029–1040, 1999.

[59] J. W. Larsen, S. R. Nielsen, and S. Krenk. Dynamic stall model for wind turbine airfoils. *Journal of Fluids and Structures*, 23(7):959–982, 2007.

[60] E. Lazar, B. DeBlauw, N. Glumac, C. Dutton, and G. Elliott. A practical approach to PIV uncertainty analysis. In *27th AIAA Aerodynamic Measurement Technology and Ground Testing Conference*, volume 28, 2010.

[61] J.-W. Lee, J.-H. Han, H.-K. Shin, and H.-J. Bang. Active load control of wind turbine blade section with trailing edge flap: Wind tunnel testing. *Journal of Intelligent Material Systems and Structures*, 25(18):2246–2255, 2014.

[62] J. G. Leishman. Validation of approximate indicial aerodynamic functions for two-dimensional subsonic flow. *Journal of Aircraft*, 25(10):914–922, 1988.

[63] J. G. Leishman. Challenges in modelling the unsteady aerodynamics of wind turbines. *Wind energy*, 5(2-3):85–132, 2002.

[64] J. G. Leishman. *Principles of Helicopter Aerodynamics*. Cambridge University Press, 2006.

[65] J. G. Leishman and T. Beddoes. A semi-empirical model for dynamic stall. *Journal of the American Helicopter society*, 34(3):3–17, 1989.

[66] D. Markus. Vermessung des Eiffel-Windkanals des Fachgebietes SLA. Interner Bericht, April 2016.

[67] B. Marrant and T. van Holten. Comparison of smart rotor blade concepts for large offshore wind turbines. *Offshore Wind Energy and Other Renewable Energies in Mediterranean and European Seas*, 2006.

[68] D. Mateescu and M. Abdo. Unsteady aerodynamic solutions for oscillating airfoils. *AIAA Paper*, 227:2003, 2003.

[69] L. McCroskey, W.J. Carr and K. McAlister. Dynamic stall experiments on oscillating airfoils. *AIAA Journal*, 14(1):57–63, 1976.

[70] T. Meißner. Experimentelle Ermittlung aerodynamischer Übertragungsfuntionen für ein flexibles Profil. Master's thesis, FG SLA, TU Darmstadt, 2016.

[71] K. Mulleners and M. Raffel. The onset of dynamic stall revisited. *Experiments in Fluids*, 52(3):779–793, 2012.

[72] H. Naumann and H. Yeh. Lift and pressure fluctuations of a cambered airfoil under periodic gusts and applications in turbomachinery. *Journal of Engineering for Power*, 95(1):1–10, 1973.

[73] A. E. Panah, J. M. Akkala, and J. H. Buchholz. Vorticity transport and the leading-edge vortex of a plunging airfoil. *Experiments in Fluids*, 56(8):1–15, 2015.

[74] R. Pereira, G. Schepers, and M. D. Pavel. Validation of the Beddoes-Leishman dynamic stall model for horizontal axis wind turbines using MEXICO data. *Wind Energy*, 16(2):207–219, 2013.

[75] E. Postel and E. Leppert. Theoretical pressure distributions for a thin airfoil oscillating in incompressible flow. *Journal of Aeronautical Sciences*, 15:486–492, 1948.

[76] M. Raffel, C. E. Willert, J. Kompenhans, et al. *Particle image velocimetry: a practical guide*. Springer, 2013.

[77] A. G. Rainey. Measurement of aerodynamic forces for various mean angles of attack on an airfoil oscillating in pitch and on two finite-span wings oscillating in bending with emphasis on damping in the stall. *NACA Tech Rept. 1305*, 1957.

[78] E. G. Reid. An experimental determination of the lift of an oscillating airfoil. *Journal of the Aeronautical Sciences*, 8(1):1–6, 1940.

[79] A. Rezaeiha, M. Arjomandi, M. Kotsonis, and M. O. L. Hansen. Identification of variations of angle of attack and lift coefficient for a large horizontal-axis wind turbine. In *15TH European Turbulence Conference*, 2015.

[80] D. Rival, T. Prangemeier, and C. Tropea. The influence of airfoil kinematics on the formation of leading-edge vortices in bio-inspired flight. *Experiments in Fluids*, 46(5):823–833, 2009.

[81] P. Rojratsirikul, Z. Wang, and I. Gursul. Unsteady fluid–structure interactions of membrane airfoils at low reynolds numbers. *Experiments in Fluids*, 46(5):859–872, 2009.

[82] L. Schwarz. Berechnung der Druckverteilung einer harmonisch sich verformenden Tragfläche in ebener Strömung. *Luftfahrtforschung*, 17:379–386, 1940.

[83] W. R. Sears. *A systematic presentation of the theory of thin airfoils in non-uniform motion*. PhD thesis, California Institute of Technology, 1938.

[84] W. R. Sears. Some aspects of non-stationary airfoil theory and its practical application. *Journal of the Aeronautical Sciences*, 8(3):104–108, 1941.

[85] C. Shih, L. Lourenco, L. van Dommelen, and A. Krothapalli. Unsteady flow past an airfoil pitching at a constant rate. *AIAA Journal*, 30(5):1153–1161, 1992.

[86] W. Shyy, H. Aono, S. K. Chimakurthi, P. Trizila, C.-K. Kang, C. E. Cesnik, and H. Liu. Recent progress in flapping wing aerodynamics and aeroelasticity. *Progress in Aerospace Sciences*, 46(7):284–327, 2010.

[87] A. Silverstein and U. T. Joyner. Experimental verification of the theory of oscillating airfoils. *NACA Tech Rept. 673*, 1939.

[88] H. Spiegelberg. *Adaptive camber airfoil for load alleviation in horizontal axis wind turbines: analytical and numerical study.* PhD thesis, TU Darmstadt, 2015.

[89] J. Spurk. *Strömungslehre: Einführung in die Theorie der Strömungen.* Springer-Verlag, 2013.

[90] M. Stanislas, K. Okamoto, and C. Kähler. Main results of the first international PIV challenge. *Measurement Science and Technology*, 14(10):R63, 2003.

[91] M. Stanislas, K. Okamoto, C. J. Kähler, and J. Westerweel. Main results of the second international PIV challenge. *Experiments in Fluids*, 39(2):170–191, 2005.

[92] M. Stanislas, K. Okamoto, C. J. Kähler, J. Westerweel, and F. Scarano. Main results of the third international PIV challenge. *Experiments in Fluids*, 45(1):27–71, 2008.

[93] H. Sutherland. On the fatigue analysis of wind turbines. Technical report, Sandia National Laboratories, 1999.

[94] T. Theodorsen. General theory of aerodynamic instability and the mechanism of flutter, NACA Report 496, US nat. *Advisory Committee for Aeronautics, Langley, VA*, 13, 1935.

[95] C. van Dam, D. E. Berg, and S. J. Johnson. Active load control techniques for wind turbines. Technical report, Sandia National Laboratories, 2008.

[96] J. van Wingerden, A. Hulskamp, T. Barlas, B. Marrant, G. van Kuik, D. Molenaar, and M. Verhaegen. On the proof of concept of a 'smart' wind turbine rotor blade for load alleviation. *Wind Energy*, 11(3):265, 2008.

[97] J.-W. van Wingerden, A. Hulskamp, T. Barlas, I. Houtzager, H. Bersee, G. van Kuik, and M. Verhaegen. Two-degree-of-freedom active vibration control of a prototyped 'smart' rotor. *Control Systems Technology, IEEE Transactions on*, 19(2):284–296, 2011.

[98] P. S. Veers, T. D. Ashwill, H. J. Sutherland, D. L. Laird, D. W. Lobitz, D. A. Griffin, J. F. Mandell, W. D. Musial, K. Jackson, M. Zuteck, et al. Trends in the design, manufacture and evaluation of wind turbine blades. *Wind Energy*, 6(3):245–259, 2003.

[99] D. N. Veritas. Design and manufacture of wind turbine blades, offshore and onshore wind turbines. *DNV Standard, DNV-DS-J102*, pages 2010–11, 2010.

[100] M. R. Visbal, R. E. Gordnier, and M. C. Galbraith. High-fidelity simulations of moving and flexible airfoils at low reynolds numbers. *Experiments in Fluids*, 46(5):903–922, 2009.

[101] H. Vollmers. Detection of vortices and quantitative evaluation of their main parameters from experimental velocity data. *Measurement Science and Technology*, 12(8):1199, 2001.

[102] T. H. Von Karman and W. Sears. Airfoil theory for non-uniform motion. *Journal of the Aeronautical Sciences*, 5(10):379–390, 1938.

[103] H. Wagner. Über die Entstehung des dynamischen Auftriebes von Tragflügeln. *ZAMM-Journal of Applied Mathematics and Mechanics/Zeitschrift für Angewandte Mathematik und Mechanik*, 5(1):17–35, 1925.

[104] A. Widmann and C. Tropea. Parameters influencing vortex growth and detachment on unsteady aerodynamic profiles. *Journal of Fluid Mechanics*, 773:432–459, 2015.

[105] A. G. M. Widmann. *Formation and Detachment of Leading Edge Vortices on Unsteady Airfoils*. PhD thesis, TU Darmstadt, 2015.

[106] Windmonitor IWES Fraunhofer. Developement of wind turbine dimensiones. www.windmonitor.iwes.fraunhofer.de, 2016.

[107] A. Wöhler. Über die Festigkeitsversuche mit Eisen und Stahl. *Ernst und Korn, Berlin*, 1870.

[108] C. J. Wojcik and J. H. Buchholz. Vorticity transport in the leading-edge vortex on a rotating blade. *Journal of Fluid Mechanics*, 743:249–261, 2014.

Nomenclature

Abbreviations

Symbol	Description
ABL	Atmospheric boundary-layer
COE	Cost of Energy
FoV	Field of View
IA	Interrogation area
LE	Leading-edge
LEV	Leading-edge vortex
PIV	Particle image velocimetry
TE	Trailing-edge

Dimensionless Numbers

Symbol	Description	Definition
C_L	Lift coefficient	$C_L = \dfrac{L}{\frac{\rho}{2}U_\infty^2}$
C_p	Pressure coefficient	$C_p = \dfrac{p_s - p_\infty}{\frac{\rho}{2}U_\infty^2}$
$C_{\Delta p}$	Pressure difference coeff.	$C_{\Delta p} = \dfrac{p_{SS} - p_{PS}}{\frac{\rho}{2}U_\infty^2}$
CR	Circulation reduction	$CR = \dfrac{\sigma(\Gamma^+_{\text{rigid}}) - \sigma(\Gamma^+_{\text{adaptive}})}{\sigma(\Gamma^+_{\text{rigid}})}$

k	Reduced frequency	$k = \dfrac{\pi f c}{U_\infty}$
LR	Load reduction	$LR = \dfrac{\sigma\left(L_{\text{rig}}\right) - \sigma\left(L_{\text{ad}}\right)}{\sigma\left(L_{\text{rig}}\right)}$
Re	Reynolds number	$Re = \dfrac{U_\infty D}{\nu}$
Sr	Strouhal number	$Sr = \dfrac{2\Delta h f}{U_\infty}$

Greek Symbols

Symbol	Description	Dimensions	Units
α	Angle of attack, AoA	$L^0 T^0 M^0$	°
Δ	Difference	$L^0 T^0 M^0$	
δ	Shear layer thickness	L	m
η	Camber	$L L^{-1}$	%c
Γ	Circulation	$L^2 T^{-1}$	m²/s
γ	Trailing flap angle	$L^0 T^0 M^0$	°
κ	Rotational stiffness	$M L^2 T^{-2}$	Nm/rad
Λ	Relative flap length	$L L^{-1}$	%c
λ	Wave length	L	m
ν	Kinematic viscosity	$L^2 T^{-1}$	m²/s
ω	Angular frequency	T^{-1}	rad/s
ρ	Mass density	$M L^{-3}$	kg/m³
φ	Phase angle	$L^0 T^0 M^0$	°
Γ_1	Scalar function to identify vortex centers	$L^0 T^0 M^0$	

| Γ_2 | Scalar function to identify vortex boundaries | $L^0T^0M^0$ | |

Roman Symbols

Symbol	Description	Dimensions	Units
P	Power	ML^2T^{-3}	watt
b	Half chord length, $b = c/2$	L	m
C	Theodorsen function	$L^0T^0M^0$	
c	Chord length	L	m
D	Diameter	L	m
e	Elastic axis	LL^{-1}	%c
f	Frequency	T^{-1}	Hz
h	Transfer function	$L^0T^0M^0$	
i	Imaginary number		
L	Lift	MLT^{-2}	N
M	Moment	ML^2T^{-2}	Nm
N	Coupling ratio	$L\,L^{-1}$	
p	Pressure	$ML^{-1}T^{-2}$	Pa
q	Dynamic pressure	$ML^{-1}T^{-2}$	Pa
S	Sears function	$L^0T^0M^0$	
s	Airfoil span	L	m
T	Time period	T	s
t	Time	T	s

U	Steady horizontal velocity	$L^1 T^{-1}$	m/s
u	Measurement uncertainty		
v	Perturbing vertical velocity	$L^1 T^{-1}$	m/s

Superscripts

Symbol	Description
$'$	Fluctuating
$*$	Experimental
$+$	Dimensionless
$\cdot$	Time derivative
$\sim$	Phase average
$\char"02C6$	Amplitude

Subscripts

Symbol	Description
γ	TE angle
L	Lift
p	Pressure
0	Pre-, Initial
κ	Rotational stiffness
∞	Undisturbed
adaptive, ad	Adaptive camber airfoil
aero	Aerodynamic
dyn	Dynamic

158

e	Excitation
eff	Effective
g	Gust
h	Heaving motion (Plunge)
LE	Leading-edge
m	Mean
max	Maximal
min	Minimal
P	Power
p	Pitch
PS	Pressure side
qs	Quasi-steady
r	Reaction
rigid, rig	Rigid airfoil
s	Static
SS	Suction side
TE	Trailing-edge

A. Measurement Uncertainties

Each measured variable has an uncertainty due to non-perfect measurement equipment. These uncertainties are obtained according to the guidelines of GUM type B [43], using the specifications of the measurement devices. For steady experiments, this is the most important and the only accessible source of uncertainty. During dynamic measurements, the turbulent nature of the flow introduces an additional stochastic uncertainty. This uncertainty is conveniently obtained from phase averaged data according to the guidelines of GUM Type A [43]. The combined uncertainty during dynamic measurements, comprising uncertainties due to the non-perfect measurement equipment and the turbulent inflow is obtained by the Euclidean norm of type A and type B uncertainties.

Uncertainties due to Instrumentation - GUM Type B

A directly measured variable x is influenced by each component of the measurement chain (i.e. sensor, amplifier, AD converter). The standard uncertainty of a directly measured variable is estimated by taking the relative uncertainty of each component of the measurement chain p_i into account:

$$\frac{u(x)}{|x|} = \sqrt{\sum p_i^2} \tag{A.1}$$

Some variables are not directly measured, but calculated from several directly measured variables x_i. The standard uncertainty of such a dependent variable $f(x_i)$ is estimated by applying the law of propagation of uncertainties, using the formula

$$\frac{u(f(x_i))}{|f(x_i)|} = \sqrt{\sum \left(\frac{\partial f}{\partial x_i}\right)^2 u^2(x_i)}. \tag{A.2}$$

Scaling the standard uncertainty $\frac{u(x)}{|x|}$ with the expected order of magnitude of the respective variable $|x|$ yields the uncertainty of the measured variable u_x. The same

161

holds for a dependent variable:

$$u_{f(x)} = \frac{u(f(x))}{|f(x)|} \cdot |f(x)| \qquad (A.3)$$

Stochastic Uncertainties - GUM Type A

For unsteady measurements, additional uncertainties due to the stochastic nature of the turbulent inflow have to be taken into account. From the phase averaged data, the standard uncertainty u_A of a variable x is calculated according to the guidelines of GUM Type A, [43]

$$u_A(x) = \frac{\sigma(x)}{\sqrt{N}}. \qquad (A.4)$$

Where N is the number of performed individual load cycles and $\sigma(x)$ is the averaged standard deviation of the fluctuating mean.

Combined Uncertainty

The combined standard uncertainty $\frac{u_C}{|x|}$ is the Euclidean norm of type A and type B uncertainties:

$$\frac{u_C}{|x|} = \sqrt{\frac{u_A{}^2}{|x|} + \frac{u_B{}^2}{|x|}}. \qquad (A.5)$$

Scaling with a typical value for the measured variable x yields the combined uncertainty u_x during unsteady measurements.

A.1. Sinusoidal Vertical Gust Experiments

Type B Uncertainties

The **lift force** L is measured with a wind tunnel balance, consisting of a multiaxial force sensor *K3D120* with a full scale of 500N and an accuracy class of 0.5. Signals

are amplified by a *GSV-1A8* amplifier incorporating an *NI 6210* board for AD conversion with a combined accuracy class of 0.1. Expressing the relative component uncertainties by their respective accuracy classes yields an uncertainty of the measured lift L due to the accuracy of the force balance components of

standard uncertainty $\frac{u(L)}{|L|}$	maximal value of $|L|$	measurement uncertainty u_L
$4 \cdot 10^{-3}$	30 N	± 0.12 N

The **mean angle of attack** α_m is measured using a *Kuebler 8.5850* absolute encoder with a maximal error of $0.2°$ over a full rotation of $360°$ and converted by a *NI 6211* 16 bit AD board. A calibration, comprising a linear regression over the total measurement range of $\pm 30°$ leads to an uncertainty for the mean angle of attack α_m of

standard uncertainty $\frac{u(\alpha_m)}{|\alpha_m|}$	typic value of $|\alpha_m|$	measurement uncertainty u_{α_m}
$1.6 \cdot 10^{-3}$	$2°$	$\pm 3.2 \cdot 10^{-3}\,°$

A similar procedure is applied for the **trailing flap angle** γ, which is measured using an *ams AS5162* rotary hall sensor with a full scale analog output of 5 V. The application range is programmed to match the maximal flap deflections of $\pm 15°$, which allows to optimally exploit the input range of 5 V of the *NI 6210* AD board. A calibration, consisting of a linear regression, leads to an uncertainty for the trailing flap angle γ of

standard uncertainty $\frac{u(\gamma)}{|\gamma|}$	maximal value of $|\gamma|$	measurement uncertainty u_γ
$2.3 \cdot 10^{-3}$	$15°$	$\pm 0.035°$

The airfoil is manufactured from polyamide by direct laser sintering with an *EOS formiga p100*. This rapid prototyping machine produces components with a tolerance of $1 \cdot 10^{-4}$ m. The airfoil **chord** c is measured with a sliding caliper and the airfoil **span** s is measured with a sliding tape. The corresponding uncertainties are

standard uncertainty $\frac{u(c)}{|c|}$	typic value of $|c|$	measurement uncertainty u_s
$6.2 \cdot 10^{-4}$	0.18 m	$1.1 \cdot 10^{-4}$ m
standard uncertainty $\frac{u(s)}{|s|}$	typic value of $|s|$	measurement uncertainty u_s
$6.25 \cdot 10^{-3}$	0.8 m	$5 \cdot 10^{-3}$ m

The **dynamic pressure** q_∞ in front of the active grid is obtained from the pressure difference over the wind tunnel nozzle, measured with two *Setra C-239* high accuracy low differential pressure transducers. Both transducers have a full scale accuracy of 0.073 % and their output signals are converted by a *NI 6211* AD board. Considering only uncertainties associated with the pressure measurement, the uncertainty for the dynamic pressure q_∞ is obtained as

standard uncertainty $\frac{u(q_\infty)}{|q_\infty|}$	typic value of $|q_\infty|$	measurement uncertainty u_{q_∞}
$2.3 \cdot 10^{-3}$	1800 Pa	± 4.12 Pa

The mass density of the air $\rho = p/\mathrm{R}(\varphi)T$ is calculated using the temperature T, ambient pressure p and the gas constant R, which is a function of the humidity φ of the air. T is obtained with an *EPCOS NTC* thermistor which has an accuracy of $\Delta T = \pm 0.3°$ in the expected temperature range. A temperature compensated *Sensortechnics 144S* pressure transducer with an accuracy class of 0.1 captures p. An *HIH-4000* humidity sensor of an absolute accuracy of 3.5 % is used to measure φ. All signals are sampled with a *NI 6281* 18 bit AD converter. From the uncertainties of the dynamic pressure q_∞ and the density of the air $\rho(T, p, \varphi)$ the uncertainty of the **inflow velocity** U_∞ is obtained as

standard uncertainty $\frac{u(U_\infty)}{|U_\infty|}$	typic value of $|U_\infty|$	measurement uncertainty u_{U_∞}
$3 \cdot 10^{-3}$	20 m/s	± 0.06 m/s

The uncertainty of the **lift coefficient** $C_L = L/\left(\frac{1}{2}\rho U^2 cs\right)$ is then estimated by using the uncertainties of the lift u_L, air density u_ρ, inflow velocity u_{U_∞} and geometric uncertainties of the airfoil u_c and u_s, which yields

standard uncertainty $\frac{u(C_L)}{|C_L|}$	max. value of $|C_L|$	measurement uncertainty u_{C_L}
$3 \cdot 10^{-3}$	1.2	$\pm 3.6 \cdot 10^{-3}$

The flow direction is measured with a cross-wire probe. For each wire, the uncertainty in the velocity measurement is calculated individually. According to the man-

ufacturer of the anemometer, a *Dantec Streamline*, the anemometer's accuracy is high and can be omitted in uncertainty considerations. The most important error occurs during velocity calibration, when the curve fits are linearized. Additionally, the stochastic error due to resolution of the AD converter is taken into account. The geometric error due to probe positioning and the error due to temperature variation have an equal effect on each wire. When calculating the **gust angle** $\widehat{\alpha}_g$, they cancel out and are therefore omitted. This leads to an uncertainty in the gust angle of

standard uncertainty $\dfrac{u(\widehat{\alpha}_g)}{\left|\widehat{\alpha}_g\right|}$	max. value of $\left|\widehat{\alpha}_g\right|$	measurement uncertainty $u_{\widehat{\alpha}_g}$
$3.1 \cdot 10^{-2}$	$6.2\,°$	$\pm 0.2\,°$

Combined Uncertainties

Type A uncertainties due to the stochastic nature of the flow are derived from phase averaged data. The respective values, as well as the combined uncertainties of all variables, are summarized in Table A.1.

Table A.1.: Standard uncertainties of variables measured in the Oldenburg experimental setup. The combined standard uncertainty is obtained from standard uncertainties of type A and type B.

	Standard uncertainty			Combined uncertainty
	Type B $\dfrac{u_B}{|x|}$	Type A $\dfrac{u_A}{|x|}$	Combined $\dfrac{u_C}{|x|}$	u_x
Gust amplitude $\widehat{\alpha}_g$	$3.1 \cdot 10^{-2}$	$2 \cdot 10^{-2}$	$3.7 \cdot 10^{-2}$	$\pm 0.23\,°$
Inflow velocity U_∞	$3 \cdot 10^{-3}$	$4 \cdot 10^{-3}$	$5 \cdot 10^{-3}$	$\pm 0.1\,\mathrm{m/s}$
Lift L	$4 \cdot 10^{-3}$	$3 \cdot 10^{-3}$	$5 \cdot 10^{-3}$	$\pm 0.15\,\mathrm{N}$
Lift coefficient C_L	$3 \cdot 10^{-3}$	$1.5 \cdot 10^{-3}$	$3.3 \cdot 10^{-3}$	$\pm 4 \cdot 10^{-3}$
Trailing flap angle γ	$2.3 \cdot 10^{-3}$	$5 \cdot 10^{-4}$	$2.4 \cdot 10^{-3}$	$\pm 0.035\,°$

The dynamic pressure q_∞ is obtained from the pressure difference in the nozzle in front of the active grid, and sampled with a frequency well below the excitation frequency of the active grid. Accordingly, no phase averaged data for q_∞ is available.

A.2. Sinusoidally Oscillating Airfoil Experiments

Attached Flow Experiments

The **inflow velocity** U_∞ in the wind tunnel is adjusted using a *Schiltknecht MiniAir60 Micro* vane anemometer with a FS of 40 m/s and an accuracy of $\pm 1\,\%$FS. The 4 V output signal is aquired with a NI *6009 AD* converter at an input range of ± 5 V. This leads to an uncertainty of the inflow velocity U_∞ of

Standard uncertainty $\frac{u(U_\infty)}{|U_\infty|}$	Max. value of $|U_\infty|$	Meas. uncertainty u_{U_∞}
$2.2 \cdot 10^{-2}$	20 m/s	± 0.45 m/s

The **trailing flap angle** γ is measured using an *ams AS5162* rotary hall sensor with a full scale analog output of 5 V. The application range is programmed to match the maximal flap deflections of $\pm 15°$ which allows to optimally exploit the input range of 5 V of the *NI 6210* AD board. A calibration, consisting of a linear regression, leads to an uncertainty for the trailing flap angle γ of

Standard uncertainty $\frac{u(\gamma)}{|\gamma|}$	Max. value of $|\gamma|$	Meas. uncertainty u_γ
$2.3 \cdot 10^{-3}$	$15°$	$\pm 3.5 \cdot 10^{-2}\,°$

The **static pressure on the airfoil's surface** p_s and the **dynamic pressure of the pitot-tube** q_∞, are measured with *HCL* miniature pressure transducers with a combined non-linearity and hysteresis of $\pm 0.25\,\%$FS. Transducers on the airfoil's suction side have a full scale (FS) of 12.5 mbar. On the airfoil's pressure side and for the pitot-static tube, the full scale of the transducers is 5 mbar. The pressure transducers output signal of 20 mV full scale is amplified to the 5 V full scale input of the *NI 6210* AD device with an in-house fabricated adjustable amplifier to obtain maximal resolution. The amplified output signal is calibrated using a *CPC6000 mensor* precision pressure controller with a reading accuracy of 0.01 %, consisting of a linear regression over 15 datapoints with a maximal deviation of 0.1 %.

	Standard uncertainty $\frac{u(x)}{|x|}$	Maximal value of $|x|$	Measurement uncertainty u_x
$p_{s,\text{SS}}$	$5.1 \cdot 10^{-3}$	7.2 mbar	$\pm 3.6 \cdot 10^{-2}$ mbar
$p_{s,\text{PS}}$ and q_∞	$5.1 \cdot 10^{-3}$	2.4 mbar	$\pm 1.2 \cdot 10^{-2}$ mbar

The **coefficient of the pressure difference** $C_{\Delta p}$ between suction and pressure side can is obtained by $C_{\Delta p} = C_{p,\text{SS}} - C_{p,\text{DS}} = \frac{p_{s,\text{SS}} - p_{s,\text{DS}}}{q_\infty}$. Applying the law of propagation of uncertainties, the uncertainty of $C_{\Delta p}$ is calculated to be

Standard uncertainty $\frac{u(C_{\Delta p})}{|\Delta C_p|}$	Max. value of $|C_{\Delta p}|$	Meas. uncertainty $u_{C_{\Delta p}}$
$8.3 \cdot 10^{-3}$	5	$\pm 4.0 \cdot 10^{-2}$

The airfoil's **geometric uncertainties** arise from manufacturing uncertainties and measurement uncertainties. The airfoil is manufactured from polyamide by direct laser sintering with an *EOS formiga p100*. This rapid prototyping machine produces components with a tolerance of 10^{-4} m. The airfoil's **chord** c is measured with a sliding caliper with an absolute accuracy of 10^{-4} m and the airfoil's **span** s is measured with a sliding tape with an absolute accuracy of 10^{-3} m. Combining the uncertainties due to manufacturing and due to measuring leads to a combined geometric uncertainty of

	Standard uncertainty $\frac{u(x)}{|x|}$	Typic value of $|x|$	Meas. uncertainty u_x
Chord	$1.2 \cdot 10^{-2}$	0.12 m	$\pm 1.4 \cdot 10^{-4}$ m
Span	$2.2 \cdot 10^{-3}$	0.45 m	$\pm 5.0 \cdot 10^{-3}$ m

The **dynamic angle of attack** $\alpha(t)$ of the airfoil is applied via the pitch-plunge rig. The airfoil is fixed to two *LinMotPS01-48x240F-C* linear actuators that are operated via *LintMot LinTalk* software. According to the manufacturer, the uncertainty in start and stop positioning is 0.05 mm. This results in an uncertainty of the start and stop angle of attack of $3 \cdot 10^{-5}$ °. No information about the uncertainty of the position during the prescribed motion is given. Therefore, two *Freescale Semiconductor MMA1270KEG* acceleration sensors with a measurement range of ± 2.5 g and an accuracy of 1.3 %FS are attached to the actuators pistons. $\alpha(t)$ is obtained from

the starting position of the linear actuators and the integraded accelerator signals and can be calulated with an uncertainty of

Standard uncertainty $\frac{u(\alpha(t))}{\vert\alpha(t)\vert}$	Max. value of $\vert\alpha(t)\vert$	Meas. uncertainty $u_{\alpha(t)}$
$1.3 \cdot 10^{-2}$	$6°$	$\pm 8 \cdot 10^{-2}°$

Detached Flow Experiments

The basis of high quality **velocity field** measurements by means of PIV is the quality of the acquired raw images. Surface reflections lead to spurious intensity distributions and have to be minimized. Sufficient, but not too many seeding particles of the right size that scatter the laser light have to be introduced in the flow. According to Raffel [76], the same six or more particles should be mapped in each interrogation area (IA) of both acquired frames. In-plane displacement should be in the order of 0.25 IA, out-of-plane displacement should stay below 25 % of the light sheet thickness. The particle diameter should span 2-2.5 pixels. This maximizes the signal-to-noise ratio while minimizing pixel locking errors during cross correlation. If qualitatively good raw images are acquired, the uncertainty of PIV based velocity measurements still depends on a variety of parameters; the ability of the seeding particles to follow the flow, the imaging system, its calibration and the recording procedure and analysis of the acquired raw data. The uncertainties due to these error sources are estimated individually, the Euclidean norm of all uncertainties forms the combined uncertainty of a PIV based velocity measurement.

As for any measured variable, the uncertainty of the obtained velocity field depends on the combined **uncertainty of the measurement equipment** u_E. This uncertainty is calculated according to the guidelines of GUM type B [43]. The relative uncertainty of each component of the measurement chain is accounted for by the law of propagation of uncertainties. In PIV measurements, the velocity is obtained by relating the spatial distance of a particle Δx in two consecutively acquired frames to the time interval Δt between the two frames. According to Lazar et al. [60] uncertainties of Δx arise from uncertainties in the camera and the calibration that relates physical length to pixel units. Uncertainties of Δt arise from uncertainties in the delay generator and the laser pulse timing. The resulting standard uncertainty of a PIV velocity

measurement is given by Lazar et al. [60] as

$$
\frac{u_{\mathrm{E}}\left(\vec{u}\right)}{|\vec{u}|} = \sqrt{
\begin{aligned}
&\left[\left(\frac{1}{L}\right)^2 u_l^2 + \left(\frac{-l}{L^2}\right)^2 u_{L1}^2 + \left(\frac{-l}{L^2}\right)^2 u_{L2}^2 + \left(\frac{l}{\lambda L}\right)^2 u_\lambda^2\right] \\
&+ \left(\frac{-l}{\Delta t L}\right)^2 \left[u_{t1}^2 + u_{t2}^2\right]
\end{aligned}
}
$$

$$= 0.001$$

(A.6)

where l is the image length in pixels, L is the image length in meter, L_1 is the geometric uncertainty of the calibration target, expressed in the image plane length , L_2 is the image distortion due to lens aberrations, expressed in image plane length, t_1 is the Laser pulse timing, t_2 is the accuracy of the delay generator, λ is the distance of the measuring plane to the camera lens. Typical values for the experimental setup are given in table A.2.

Table A.2.: Summary of equipment uncertainty parameters

Parameter	Description	Value	Uncertainty
l	Calibration target length in m	$0.12\,\mathrm{m}$	$1.0\cdot 10^{-6}\,\mathrm{m}$
L_1	Geometry of calibration target	519 pixels	1 pixel
L_2	Image distortion due to lens aberration	519 pixels	4.5 pixels
λ	Distance between lens and image plane	$0.6\,\mathrm{m}$	$5.0\cdot 10^{-6}\,\mathrm{m}$
t_1	Laser pulse timing	$1.0\cdot 10^{-4}\,\mathrm{s}$	$1.0\cdot 10^{-9}\,\mathrm{s}$
t_2	Accuracy of delay generator	$1.0\cdot 10^{-4}\,\mathrm{s}$	$1.5\cdot 10^{-9}\,\mathrm{s}$

PIV is based on the assumption that seeding particles follow the local flow field instantaneously without any relative velocity between seeding particle and surrounding flow. In reality, there is always a slip between seeding particles and surrounding flow which results in an **uncertainty due to the particle inertia** u_{P}. The ability of the particle to follow the fluid motion can be estimated according to Raffel [76] by comparing the response times of a particle τ_{s} to the typical flow time τ_{f}. The response time of DEHS seeding particle in the current setup is estimated by Widmann [105]. With a mean diameter of $d_{DEHS} = 1\,\mu\mathrm{m}$, a density of $\rho_{\mathrm{DEHS}} = 910\,\mathrm{kg/m^3}$ and the dynamic viscosity of the air $\mu = 1.846\cdot 10^{-5}\,\mathrm{kgm/s}$, the response time is calculated

as $\tau_s = d_{\text{DEHS}}^2 \cdot \rho_{\text{DEHS}}/18\mu = 2.7\,\mu\text{s}$. The typical flow time is estimated by the convective time of th Kolmogorov length scale $\eta_K = c \cdot Re^{-3/4}$, where the airfoil's chord c is the global length scale and Re the Reynolds number. For a maximal flow velocity $U_\infty = 20\,\text{m/s}$, the typical flow time calculates to $\tau_f = 15\,\mu\text{s}$. With $\tau_f > \tau_s$, the particles are assumed to follow the flow without slip and the uncertainty due to particle inertia is set to $u_P = 0$.

The stochastic nature of the flow is responsible for the **sampling uncertainty** u_S. Depending on the instant in time at which data are acquired, a different value will be collected. If the values are normally distributed, as it can be assumed in turbulent flow, standard uncertainty is calculated according to the guidelines of GUM Type A, [43]

$$u_S(\vec{u}) = \frac{\sigma(\vec{u})}{\sqrt{N}}, \tag{A.7}$$

where N is the number of collected data points and $\sigma(\vec{u})$ is the averaged standard deviation of the fluctuating mean. The uncertainty due to sampling depends largely on the flow situation. From the acquired temporally resolved velocity fields of the current setup, the uncertainty due to sampling is estimated as $u_S \leq 0.5\%$ in undisturbed flow and as $u_S \leq 3\%$ in regions of separated flow.

The **uncertainties due to image analysis** u_I are as numerous as the applied analysis algorithms. The image analysis of PIV data incorporates pre-processing algorithms, interpolation techniques, post-processing and filtering. Pre-processing aims to increase the information content of the acquired raw data. For example, if a seeding particle is mapped on the border of two IAs, an error intrinsic to the correlation algorithm will occur in the detected displacement. A normalization of the gray scale data with local intensity variation can help to avoid these errors. Cross correlation is a statistic method. The highest peak symbolizes the most probable particle displacement. To obtain statistically significant peaks, a certain number of particles has to be mapped in each IA. Particles can be lost from one frame to the other. Different methods can be applied to increase the information content: In-plane loss of particles can be accounted for by window shifting. Window deforming can account for high velocity gradients. The light intensity of scattered particles is Gaussian distributed. Rastering the mean values on the pixels of an IA leads to an error, which can be accounted for by sub-pixel interpolation. After correlation, the obtained ve-

locity field can be validated and filtered with various techniques to identify falsely obtained correlation peaks. These procedures comprise only a small part of the total available methods, but illustrate that the obtained combined uncertainty due to image analysis u_I depends largely on which and how the above mentioned techniques are applied. u_I is accordingly difficult to estimate. Lazar et al. [60] compared different pre-processing, processing and post-processing techniques on the same raw data. They found deviations in speed data of about 1 % in uniform flow and deviations of as high as 5-10 % in regions of high velocity gradients for different processing parameters. Separated flow on a dynamically pitching airfoil is supposed to have these high gradients. Hence, it is crucial for the comparability of different PIV runs that the data are treated with the same pre-, processing and post-processing parameters. During PIV Challenges [90–92], developers and users apply their correlation techniques to numerically obtained (and hence known) velocity fields or compare their results obtained with different algorithms to the same experimental raw data. Depending on the difficulty of the flow problem, the agreement between correlation results and numeric data varies. For time-resolved 2D turbulent velocity fields, good performing correlation algorithms match the generic velocity field with a deviation of approximately 1 %. In the current setup, the uncertainty due to image processing is estimated to $u_I = 5\,\%$.

The **combined standard uncertainty of a velocity measurement** obtained by PIV u_C is the Euclidean norm of the standard uncertainties due to measurement equipment u_E, due to sampling u_S and due to image processing u_I:

$$\frac{u_C}{|\vec{u}|} = \sqrt{\frac{u_E}{|\vec{u}|}^2 + \frac{u_S}{|\vec{u}|}^2 + \frac{u_I}{|\vec{u}|}^2}. \tag{A.8}$$

which leads to a combined uncertainty calculates of the velocity field of

Flow regime	Standard uncertainty $\frac{u(\vec{u})}{|\vec{u}|}$	Typic value of $|\vec{u}|$	Measurement uncertainty $u_{\vec{u}}$
Attached	$2.1 \cdot 10^{-2}$	20 m/s	± 0.42 m/s
Detached	$3.6 \cdot 10^{-2}$	20 m/s	± 0.72 m/s

B. Mean Values of the Dynamic Airfoil Response

Figure B.1 compares mean values of the dynamic airfoil data to the corresponding quasi-steady values, taken from parameter set (1), Chapter 4. On the left, the lift of the adaptive camber and the rigid airfoil are presented. On the right, the adaptive camber airfoil's trailing flap angle is displayed over the mean angle of attack.
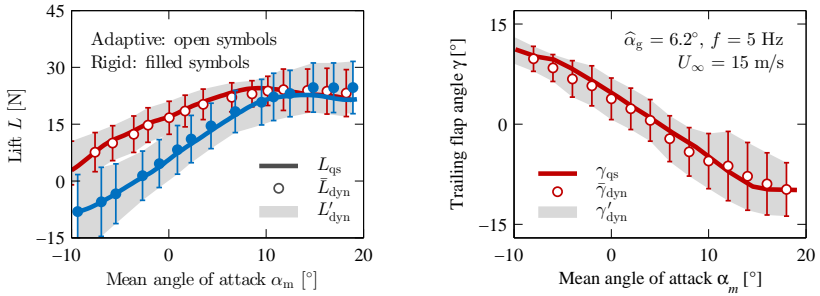
(a) Lift L on the rigid and the adaptive camber airfoil in configuration (a)

(b) Trailing flap angle γ on the adaptive camber airfoil in configuration (a)

Figure B.1.: Mean values of the dynamic measurements (marker symbols) compared to steady values (lines) for the lift L (a) and the trailing flap angle γ (b), displayed over the angle of attack α_{m}. The steady value is shown as a solid line. Dynamic data are represented by marker symbols for the mean value and error bars for the standard deviation around this mean value. Steady and dynamic measurements are performed at an inflow velocity of $U_\infty = 15\,\mathrm{m/s}$. During dynamic measurements, the gust amplitude and excitation frequency are set to $\widehat{\alpha}_{\mathrm{g}} = 6.2\,^\circ$ and $f = 5\,\mathrm{Hz}$.

The mean values of the dynamic data and the quasi-steady data show good agreement. The difference between the mean of the dynamic lift $\bar{L}_{\mathrm{dyn}}$ and steady lift L_{qs} is very small. Only at very high mean angles of attack a slight difference between dynamic mean and quasi-steady lift values is observed for both airfoils. Note that the

result is shown as a dimensional quantity. This allows an additional statement concerning the inflow velocity: The agreement of the mean dynamic and steady values indicates an identical averaged dynamic pressure during dynamic and steady experiments. This is not evident, as the operation of the active grid alters the blockage in front of the test section. For the assessment of the adaptive camber mechanism, it is crucial to keep the dynamic pressure constant, since the reduced system stiffness depends on it.

Varying other dynamic parameters of the experimental data sets ②and ③ leads to the same result: At moderate angles of attack, all investigated dynamic data possess the same mean values as their quasi-steady correspondent. Dynamic mean values can thus be approximated by their quasi-steady counterpart.

C. Quasi-Steady Reference Measurements

Quasi-steady results are needed as a reference for dynamic experiments and for a comparison with the steady thin airfoil model of Spiegelberg [88], which constitutes the basis of his dynamic model. The intention is not to provide a comprehensive study of the adaptive camber airfoil under steady inflow, which was performed by Lambie [57].

C.1. Sinusoidal Vertical Gust Encounter

During quasi-steady measurements, the active grid is mounted in front of the test section but is not operating. The mean angle of attack is varied from $-10° < \alpha_m < 20°$ in $2°$ increments by pitching the airfoil around its c/4 axis. At each mean angle of attack, force balance data and the adaptive camber airfoil's trailing flap angle are acquired. As the mean angle of attack is increased, the adaptive camber airfoil de-cambers. This process is illustrated in Figure C.1, which shows the adaptive camber airfoil's trailing flap angle γ over the mean angle of attack α_m. Results for the pre-cambered configuration (a) are shown on the left, for the stiffer configuration (b) on the right. A trailing flap angle $\gamma = 0°$ corresponds to the original Clark Y shape and is indicated with a gray line. Positive trailing flap angles correspond to an increased camber ('flaps down'), negative trailing flap angles to a decreased camber ('flaps up'). Three different inflow velocities $U_\infty = 10$, 15 and 20 m/s are tested. The quasi-steady results confirm the considerations of section 2.2 and the findings from Lambie [57] and Spiegelberg [88]: For configuration (a), the pre-cambering moment leads to a high camber for negative angle of attack. Because of the small system stiffness, the adaptive camber airfoil de-cambers at a high rate. At small dynamic pressures, it de-cambers until the original Clark Y shape ($\gamma = 0°$), at high dynamic pressures, it de-cambers completely ($\gamma = -15°$). Configuration (b) is not pre-cambered. The original Clark Y shape is attained approximately at $\alpha_m = -2°$, where no aerody-
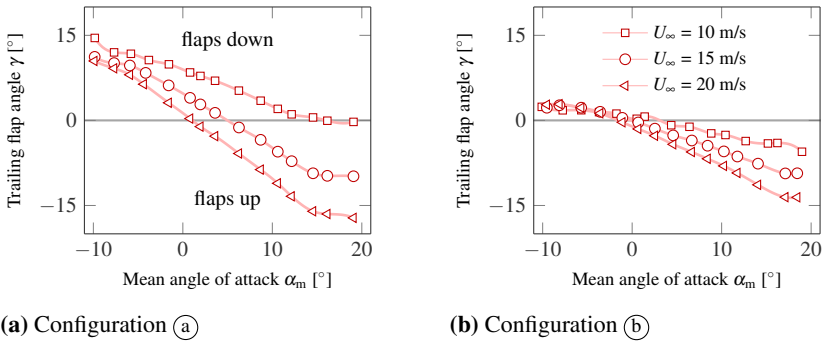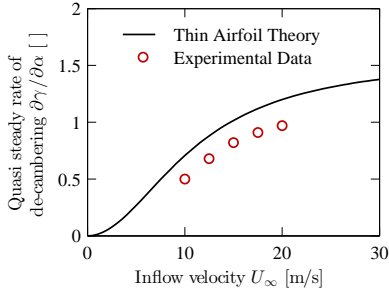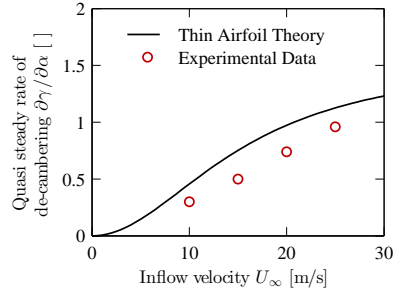
(a) Configuration ⓐ   **(b)** Configuration ⓑ

Figure C.1.: De-cambering of the adaptive camber airfoil under steady inflow conditions, represented by the trailing flap angle γ. Flaps down ($\gamma > 0$) corresponds to an enhanced camber, original Clark Y shape is at $\gamma = 0$ and flaps up ($\gamma < 0$) corresponds to a negative camber.

namic moment around leading-edge or trailing flap exists. The stiffer configuration of the restraining spring system leads to a smaller rate of de-cambering. Both airfoils de-camber linearly with increasing α_m in the angle of attack region associated with attached flow ($-8° < \alpha_m < 12°$). At very low and very high angles of attack ($\alpha_m < -8°$, $\alpha_m > 12°$), where flow separation is supposed to be present, the rate of de-cambering is smaller than in the region of attached flow.

In the region of attached flow, the rate of de-cambering $\partial\gamma/\partial\alpha$ is derived from the experimental data and compared to the quasi-steady thin airfoil model of Spiegelberg. Recall that for an airfoil with fixed spring stiffness κ_γ, leading-edge and trailing flap length and elastic axis, $\partial\gamma/\partial\alpha$ depends only on the reduced system stiffness $\kappa^+ = 2\kappa_\gamma/c^2\rho U_\infty^2$ and thereby the inflow velocity. Figure C.2 compares the experimentally derived rate of de-cambering to the results obtained with thin airfoil theory. Values for the adaptive camber airfoil in configuration ⓐ are shown on the left, for the adaptive camber airfoil in configuration ⓑ on the right. The experimental results are over predicted by thin airfoil theory, but the trend agrees well. As it is shown by Lambie [57], the adaptive camber mechanism affects the airfoil's lift coefficient C_L. The de-cambering of the adaptive camber airfoil results in a decreased C_L curve slope when displayed over the angle of attack. The pre-cambering moment adds an additional camber and shifts the C_L curve vertically. Figure C.3 graphically illustrates
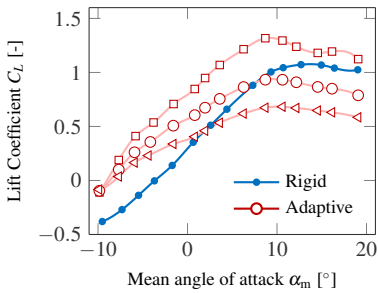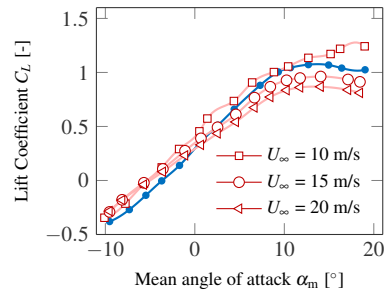
(a) Configuration (a)

(b) Configuration (b)

Figure C.2.: The quasi-steady rate of de-cambering $\partial\gamma/\partial\alpha$ for the adaptive camber airfoil in configuration (a) and configuration (b) as a function of the inflow velocity U_∞. $\partial\gamma/\partial\alpha$ increases with U_∞, i.e. reduced system stiffness κ^+.

this effect. C_L values for the adaptive camber airfoil in configuration (a) (left) and configuration (b) (right) are displayed over the angle of attack and are compared to C_L values of the rigid airfoil. For the rigid airfoil, identical C_L curves are obtained at different velocities. For lucidity, only one curve is shown at $U_\infty = 15$ m/s. In the case of the adaptive camber airfoil, an increase in dynamic pressure results in a higher rate of de-cambering, i.e. a smaller reduced system stiffness κ^+. Accordingly, different inflow velocities, represented by different marker symbols, provoke different C_L-curves. The pre-cambering of configuration (a) results in a higher C_L compared to the rigid Clark Y profile for small α_m and small U_∞. C_L-curves of the adaptive camber airfoil and the rigid airfoil intersect, when the adaptive camber airfoil takes the original Clark Y shape ($\gamma = 0°$, cf. Figure C.1). At high values of α_m and high values of U_∞, the adaptive camber airfoil has a smaller camber ($\gamma < 0°$) and produces less lift than the rigid airfoil. The high rate of de-cambering of the adaptive camber airfoil in configuration (a) leads to a significant decrease in the C_L-curve slope $\partial C_L/\partial\alpha$. Configuration (b) de-cambers less and its lift coefficient curve is closer to the rigid airfoil's C_L-curve.

**(a)** Configuration (a)

(b) Configuration (b)

Figure C.3.: Steady lift coefficient C_L for the adaptive camber and the rigid reference airfoil. The pre-cambered configuration (a) produces a higher lift coefficient. For higher dynamic pressures (i.e. lower reduced system stiffness) the airfoil de-cambers faster and the lift curve slope is decreased, compared to the stiffer configuration (b).

C.2. Sinusoidally Oscillating Airfoil

Figure C.4 shows the quasi-steady response of the rigid and the adaptive camber airfoil that serves as a reference for the dynamic investigations of the pitching and plunging airfoil of Chapter 5. Figure C.4a gives the evolution of the coefficient of the pressure difference $C_{\Delta p}$ over the mean angle of attack α_{m}, Figure C.4b shows the de-cambering of the adaptive camber airfoil, quantified by its trailing flap angle γ.
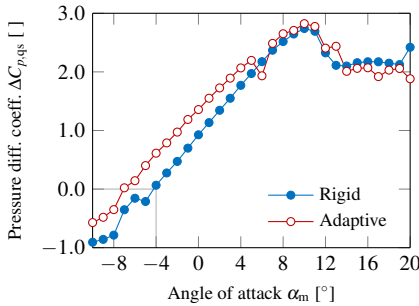
(a) Pressure difference coefficient ΔC_p as an estimator for the airfoil's lift
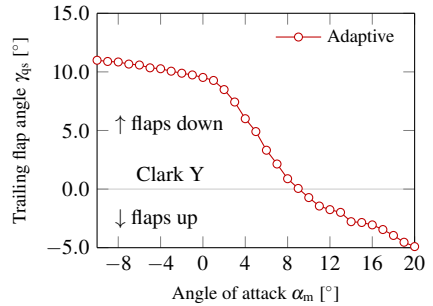
(b) Trailing flap angle γ as a measure for the de-cambering

Figure C.4.: Quasi-steady reference measurements on the rigid and the adaptive camber airfoil at $U_\infty = 15\,\mathrm{m/s}$. The rigid Clark Y airfoil has a flap deflection of $\gamma = 0\,^\circ$